

## ABSTRACT

MATZUKA, BRETT JAMES. Nonlinear Filtering Methodologies for Parameter Estimation and Uncertainty Quantification in Noisy, Complex, Biological Systems. (Under the direction of Hien Tran.)

A model is a set of equations constructed to represent the interactions of various variables within a biological or physical process. These mathematical models are used to obtain a more thorough understanding of a system or to gain information not easily obtained through other means. Measurements of system components are frequently collected and are used to validate the model through the solution of the inverse problem. The inverse problem is defined as calculating the optimal parameter values to obtain the best possible fit of the model to the data. However, as the systems of interest become more complex, the solution to the inverse problem becomes increasingly difficult.

A common method to solve the inverse problem is to use a nonlinear least squares (NLS) approach which aims to minimize the residual, the difference between the data and the model. However, this methodology presents a certain set of assumptions which may not hold for complicated biological models. An alternate method addressed in this thesis is the use of Kalman filtering. The Kalman filter is a recursive algorithm that optimally combines the uncertainties in the model and data to yield an improved final estimate. Carrying out the inverse problem utilizing this methodology has a number of advantages and has shown favorable results.

One area where these methodologies have proven fruitful is in cardiovascular modeling. The cardiovascular system is a branching network of vessels which transports blood and nutrients throughout the body while removing wastes. At the center of this process is the heart, which is the mechanism that facilitates transport through pumping. The heart and vasculature are controlled through the autonomic nervous system. As the cardiovascular system is so important to homeostasis, obtaining measurements on immediate variables of interest is difficult. Mathematical modeling is one way to gather more understanding. Using a simplified model of the cardiovascular system and the autonomic nervous system, the Kalman filter is used to illustrate their interplay. The advantages are shown over a NLS approach due to the ability to take into account modeling errors.

For many problems, measurements are collected for a multitude of individuals, representing a population. A standard approach is to fit each individual using NLS and then do statistical analysis on the individual parameters. However, this has been known to introduce bias to the final estimates. An improved method is introduced that accounts for inter- and intra-individual variability called nonlinear mixed effects. Using the Kalman filter within this framework allows the estimation of the population parameters, along with model misspecification, and time varying parameters. Using a population pharmacokinetic study, nonlinear mixed effects was carried out utilizing the Kalman filter referred to as stochastic nonlinear mixed effects. The results of this highlight the utility of the stochastic nonlinear mixed effect method through refinement of noisy model components.

© Copyright 2014 by Brett James Matzuka

All Rights Reserved

Nonlinear Filtering Methodologies for Parameter Estimation and Uncertainty Quantification in Noisy,  
Complex, Biological Systems

by  
Brett James Matzuka

A dissertation submitted to the Graduate Faculty of  
North Carolina State University  
in partial fulfillment of the  
requirements for the Degree of  
Doctor of Philosophy

Biomathematics

Raleigh, North Carolina

2014

APPROVED BY:

---

Mette Olufsen

---

Alun Lloyd

---

Ralph Smith

---

Hien Tran  
Chair of Advisory Committee

## **DEDICATION**

I would like to dedicate this to my loving and supportive family who always believed in me despite my unconventional life choices. To my mother, Paula Matzuka, who always encouraged my eccentric personality. To my father, Jim Matzuka, who taught and believed in me in all my endeavors. To my sister, Lauren Matzuka, who has only grown closer to me as time pushes forward, and proved that anything is possible through her constant pursuit of her passions.

I would like to dedicate this to my closest of friends who have always been there for me through thick and thin.



## BIOGRAPHY

Brett was born in Morris, Illinois, to Jim and Paula Matzuka. Spending his early childhood in small town Illinois, his parents decided that there would be no better place to spend his early adulthood than Kailua-Kona, Hawaii. After moving to Hawaii, Brett attended Hawaii Preparatory Academy (HPA) where his love and passion for tennis, science, and music grew tremendously. After graduating in 2003 from HPA with honors, Brett rolled a six sided die to select his undergraduate institution. Brett then attended University of Redlands in southern California with hopes of studying music, physics, and math. Upon completing one semester, Brett realized his pursuits would be better accomplished at a more appropriate institution and did not return to Redlands. As transferring was not feasible within the short time frame, Brett had found out he was admitted to the University of Queensland in Brisbane, Australia and took this opportunity to join his girlfriend in Australia and obtain college credits. Falling in love with the institution, culture, and sport of ultimate frisbee, Brett fully matriculated to the University of Queensland where he pursued studies in applied mathematics, quantitative ecology, aerospace engineering, computational finance, earth science, and a multitude of other applied sciences. Meeting a mathematical biologist PhD candidate at the university ultimate frisbee league, Brett began conducting research in mathematical biology. After finishing his Bachelor of Science degree in Mathematics in 2006, Brett continued onward with a Bachelor of Science Honours degree in Applied Mathematics at the University of Queensland.

Brett's pursuits in ultimate frisbee also continued onward winning a college ultimate national championship, Australian mixed ultimate championship, and after being selected to the Australian national team, a beach ultimate world championship all in 2007. At the end of 2007, Brett's time in Brisbane culminated with the award of first class honours in his Bachelor of Science Honours in Applied Mathematics. Having met an American girl during his time studying, Brett followed her back to the US to North Carolina where he began graduate school to pursue a doctorate in biomathematics at North Carolina State University in 2008. While their relationship went through a number of changes, Brett took a job at Pharsight as a Functional Analyst to apply his mathematical education to pharmaceutical software development. Though he bought a ring for his American girl, their love was not meant to be, and so his job, research, and frisbee career took top precedent. During the remainder of his time at NC State, Brett qualified for the college ultimate national championships with the NC State ultimate team. He also qualified for the ultimate club national championships each year with club team Ring of Fire. Brett was selected to Team USA for the Beach ultimate world championships in 2011 where they went on to win gold medal. Brett was extremely blessed to be flown to multiple countries, including Italy, Russia, and Ukraine, during this time to coach and teach ultimate frisbee. In 2013, Brett was selected to the US team for the World Games, the top honor is the sport. During all of this, Brett's interest in model refinement, uncertainty quantification, nonlinear dynamics, control theory, and optimization led a dissertation on

nonlinear filtering methodologies. This research all came together with a thesis defense in March 2014, where his long journey to a doctorate finally ended.

While the road ahead is unclear, Brett hopes to continue research in mathematical biology using advanced quantitative methods to better understand biological and physical systems. Brett is excited for the many opportunities that are ahead including the UK, Sweden, France, MIT, and many others, and truly hopes he will continue to be as fortunate and blessed as he has up to this point.

## ACKNOWLEDGEMENTS

I would like to thank my advisor, Hien Tran, for all his guidance, assistance, and help through my journey of obtaining my doctorate. I would like to thank my committee, Dr. Ralph Smith, Dr. Mette Olufsen, and Dr. Alun Lloyd, for their diligence, advice, and feedback throughout the process. My advisor and committee challenged me, pushed me, and helped me to view problems from an array of different view points, and made me into the scientist I am today.

I would like to sincerely thank my colleagues Jason Chittenden, Jon Monteleone, Mikio Aoi, Evan Bowles, Bob Leary, and Adam Attarian. I would also like to thank Pharsight for employment and an opportunity to experience mathematical applications in industry.

I would also like to greatly thank Elcelyx Therapeutics, Terri Kim, and Terri Pennell for the use of their data in my nonlinear mixed effects analysis, it would not have been possible without their permission and understanding.

I would like to thank Dr. Vera Novak, Dr. Jeser Mehlsen, and Nakeya Williams for their work with me in cardiovascular modeling.

Lastly, I can't thank my friends and family enough for their support. While the list is too long to begin, my teammates on Ring of Fire, the brotherhood of NC State ultimate, Team USA ultimate, Team Australia ultimate, Firestorm Ultimate, UQ ultimate lovers, my HPA ohana, the Cromwell college contingent, my Pharsight coworkers, those who shared their lives with me in Australia, Russia, Ukraine, Illinois, Hawaii, North Carolina, and throughout the US, this was only possible because of you.

## TABLE OF CONTENTS

<b>LIST OF TABLES</b> . . . . .	<b>viii</b>
<b>LIST OF FIGURES</b> . . . . .	<b>ix</b>
<b>Chapter 1 Introduction, Motivation, and Outline</b> . . . . .	<b>1</b>
<b>References</b> . . . . .	<b>3</b>
<b>Chapter 2 Nonlinear Filtering Methodologies for Parameter Estimation</b> . . . . .	<b>4</b>
2.1 Introduction . . . . .	4
2.2 Background and Derivation . . . . .	6
2.2.1 Bayes Filter . . . . .	6
2.2.2 The Kalman Filter . . . . .	7
2.3 Deterministic Kalman Filters . . . . .	10
2.3.1 The Extended Kalman Filter . . . . .	10
2.3.2 The Unscented Kalman Filter . . . . .	13
2.3.3 The Cubature Kalman Filter . . . . .	16
2.4 Sampling Based Kalman Filters . . . . .	21
2.4.1 Ensemble Kalman Filter . . . . .	21
2.4.2 Ensemble Transform Kalman Filter . . . . .	24
2.5 Problem Statement . . . . .	26
2.6 Applications . . . . .	27
2.6.1 Lorenz Equations . . . . .	27
2.6.2 HIV model . . . . .	39
2.6.3 Autoregulation model . . . . .	42
2.7 Conclusion . . . . .	49
<b>References</b> . . . . .	<b>52</b>
<b>Chapter 3 Physiology Background</b> . . . . .	<b>55</b>
3.1 The Cardiovascular System . . . . .	55
3.2 Cardiovascular Regulation . . . . .	60
<b>References</b> . . . . .	<b>63</b>
<b>Chapter 4 Time Varying Resistance in a Baroreflex Regulation Model During Head-Up Tilt</b> <b>64</b>	<b>64</b>
4.1 Introduction . . . . .	64
4.2 Mathematical Model . . . . .	65
4.2.1 Lumped cardiovascular model . . . . .	65
4.2.2 HUT model dynamics . . . . .	68
4.3 Sensitivity Analysis, Identifiability, and Subset Selection . . . . .	69
4.3.1 Sensitivity Analysis . . . . .	69
4.3.2 Subset Selection . . . . .	71

4.4	Methods . . . . .	72
4.4.1	$R_{aup}$ and $E_{min}$ estimation . . . . .	73
4.4.2	Nonlinear Optimization and Parameter Estimation . . . . .	73
4.4.3	Uncertainty Quantification and DRAM . . . . .	74
4.4.4	Nonlinear filter - Ensemble Transform Kalman Filter . . . . .	77
4.5	Results . . . . .	77
4.6	Discussion and Conclusion . . . . .	80
<b>References . . . . .</b>		<b>85</b>
<b>Chapter 5 Pharmacokinetics and Pharmacodynamics . . . . .</b>		<b>91</b>
5.1	Pharmacokinetics . . . . .	91
5.2	Pharmacodynamics . . . . .	94
<b>References . . . . .</b>		<b>96</b>
<b>Chapter 6 Stochastic Nonlinear Mixed Effects - A Metformin Case Study . . . . .</b>		<b>97</b>
6.1	Introduction . . . . .	97
6.2	Nonlinear Mixed Effects . . . . .	98
6.3	Kalman Filter . . . . .	102
6.3.1	Extended Kalman Filter Implementation . . . . .	102
6.3.2	Unscented Kalman Filter Implementation . . . . .	104
6.4	Study and Data . . . . .	107
6.5	Results . . . . .	107
6.5.1	Initial Model: 2-Compartment Oral . . . . .	107
6.5.2	Absorption Rate Tracking Model: EKF and UKF . . . . .	110
6.5.3	2-compartment Oral with Weibull absorption rate . . . . .	114
6.6	Discussion and Conclusion . . . . .	116
<b>References . . . . .</b>		<b>119</b>
<b>Chapter 7 Conclusion . . . . .</b>		<b>123</b>

## LIST OF TABLES

Table 2.1	Results for deterministic filters with full state observations over parameter regime shift; joint and dual, averaged over 100 runs. . . . .	29
Table 2.2	Results for ensemble filters with full state observations over parameter regime shift averaged over 100 runs. . . . .	32
Table 2.3	Results for Updated Ensemble Filters with full state observations averaged over 100 runs . . . . .	34
Table 2.4	Results for deterministic filters given observations for $x_1$ . . . . .	36
Table 2.5	Results for ensemble filters given observations for $x_1$ only . . . . .	37
Table 2.6	Results for the deterministic filters for the HIV model in $\log_{10}$ space, averaged over 100 runs . . . . .	41
Table 2.7	Results for the Ensemble Filters for the HIV model in $\log_{10}$ space, averaged over 100 runs . . . . .	42
Table 2.8	Parameters of the hemodynamic model of CA. Superscript * indicates that the value of the parameter was determined by the suggested value in [28]. Subscript $n$ indicates that the parameter represents a basal value. . . . .	46
Table 2.9	Results of ETKF vs. LM for simulated blood flow data with parameters in $\log_{10}$ space	48
Table 2.10	Results of ETKF vs. LM for real blood flow data with parameters in $\log_{10}$ space . .	49
Table 4.1	Subscript descriptions used in compartment model from [58]. . . . .	68
Table 4.2	Results of ETKF vs. NLS for blood pressure . . . . .	78
Table 6.1	Results for 2-compartment Oral model with log-additive errors for original model, EKF, UKF, and Wiebull absorption. . . . .	115
Table 6.2	Results for 2-compartment Oral model with log-additive errors for full EKF and constrained EKF. . . . .	117

## LIST OF FIGURES

Figure 2.1	Top: Plot of filter estimates for $x_1$ utilizing both joint and dual filters over all observations. Bottom: Plot of filter estimates for $x_1$ utilizing both joint and dual filters over short time scale. This gives a better perspective of the methods tracking ability.	30
Figure 2.2	Plot of Parameter estimates for the dual UKF and dual CKF along with 3 standard deviations (dotted) over the all observations, as well as true parameter values; green: $\rho$ blue: $\sigma$ . red: $\beta$ . . . . .	30
Figure 2.3	Plot of parameter estimates for the joint EKF, joint UKF and joint CKF over all observations, as well as true parameter values (purple lines). UKF and CKF obtained nearly identical results and therefore the UKF (red) is not visible. . . . .	31
Figure 2.4	Top: Plot of ensemble methods' state filter estimate of $x_1$ for the Lorenz equations prior to parameter shift. Bottom: Plot of ensemble methods' state filter estimate of $x_1$ for the Lorenz equations post parameter shift. . . . .	33
Figure 2.5	Plot of parameter estimates for both ensemble filters over all observations. . . . .	33
Figure 2.6	Top: Plot of updated ensemble state filter estimates of $x_1$ for the Lorenz equations over all observations. Bottom: Plot of updated ensemble state filter estimates of $x_3$ of the Lorenz Equations over all observations. . . . .	35
Figure 2.7	Plot of parameter estimates for both updated ensemble filters over all observations along with true parameter values (purple lines). . . . .	35
Figure 2.8	Top: Plot of joint and dual state filter estimates for $x_1$ over short time scale given observations only for $x_1$ . Bottom: Plot of joint and dual state filter estimates for $x_2$ over same short time scale given observations only for $x_1$ . . . . .	36
Figure 2.9	Plot of joint and dual filters' parameter estimates given observations only for $x_1$ . . . . .	37
Figure 2.10	Top: Plot of ensemble methods' state filter estimates for $x_1$ over short time scale given observations only for $x_1$ . Bottom: Plot of ensemble methods' state filter estimates for $x_2$ over same short time scale given observations only for $x_1$ . . . . .	38
Figure 2.11	Plot of parameter estimates using ensemble filters given observations only for $x_1$ along with true parameter values (purple lines). . . . .	38
Figure 2.12	Plot of filter estimates for the number of uninfected T cells, $T^*$ , over all the measurements. . . . .	41
Figure 2.13	Plot of filter estimates for the number of infected T cells . . . . .	43
Figure 2.14	Plot of parameter estimates for $\lambda$ , $k$ and $\delta$ for all the filters; blue dashed line is the true value, solid magenta line is the dual ukf, dashed magenta is the joint ukf, solid green line is the dual ckf, dashed green is the joint ckf, solid cyan line is the joint ekf, solid yellow is the EnKF, and solid black is the ETKF . . . . .	43

Figure 2.15	Hemodynamic schematic of the simple model of Ursino and Lodi [28]. Arterial (red) and venous (blue) compartments are enclosed within the intracranial space (brown, $C_{ic}$ : intracranial compliance). Regulated variables ( $C_a$ : arterial compliance, $R_a$ : arterial resistance) implicitly account for dynamics of hemodynamic variables ( $p_a$ : extracranial arterial blood pressure, $q$ : MCA territory arterial blood flow, $p_c$ : capillary blood pressure, $p_{ic}$ : intracranial pressure, $p_v$ : intracranial venous blood pressure, $q_f$ : cerebrospinal fluid (CSF) formation rate, $q_o$ : CSF outflow rate) and constant hemodynamic variables ( $R_{pv}$ : pial venus flow resistance, $R_v$ : cortical cerebral venous flow resistance, $R_f$ : CSF formation resistance, $R_o$ : CSF outflow resistance, $p_{vs}$ : venous sinus blood pressure). Reprinted with acknowledgement to Mikio Aoi [2]. . . . .	45
Figure 2.16	Left: simulated data, $\hat{v}$ (red), true blood flow velocity (blue), filter estimate for simulated blood flow velocity (green), NLS estimate for simulated blood flow velocity (cyan). Bottom plot displays the simulated blood flow velocity and fits due to both methodologies over a shorter time scale. Right: Plot of hidden state $C_a$ with added noise (red), true solution (blue), filter estimate (green), and NLS estimate (cyan). . . . .	47
Figure 2.17	parameter estimates for 4 of the 5 parameters for the U-L autoregulation model; (from top to bottom) 1: $kR$ 2: $\tau$ 3: $C_{an}$ 4: $G$ . . . . .	48
Figure 2.18	Plot of blood flow velocity data (red), filter estimate for the blood flow velocity (blue) and NLS model estimate for blood flow velocity (green). The NLS approach is using optimized values . . . . .	50
Figure 3.1	Blood flow from the left ventricle through the systemic arteries and veins to the right atrium. It is then ejected from the right ventricle and pumped through the pulmonary circulation back to the left atrium. Systemic arteries and pulmonary veins are $O_2$ -rich, $CO_2$ -poor blood, while systemic veins and pulmonary arteries are $O_2$ poor and $CO_2$ rich. Reprinted from [6]. . . . .	56
Figure 3.2	Left: Typical pressure during systemic circulation. Right: Typical pressure in pulmonary circulation. In both, the oscillations represent variations in time, not distance. Reprinted with permission from [1]. . . . .	57
Figure 3.3	Diagram of a typical cardiac cycle. The figure shows the relationship between heart sounds and the intraventricular pressure and volume. The top graph represents the pressures in the left ventricle and left atrium. The bottom graph shows the ventricular volume. Reprinted with permission from [6]. . . . .	58
Figure 3.4	Pressure-volume loop and four phases of the cardiac cycle. Line segments represent AC: Diastole, CD: Contraction, DF: systole, FA: relaxation. Reprinted with permission from [1]. . . . .	59
Figure 3.5	Branching structure of the typical vascular bed. Reprinted with permission from [1].	60
Figure 3.6	Diagram of the pathways by which the sympathetic and parasympathetic system's interact with the heart and vasculature. As seen, the sympathetic system synapses through the ganglia in the spine (green paths) while the parasympathetic has a more direct connection (yellow paths). The sympathetic system can affect both the heart and vasculature, while the parasympathetic only directly affects the heart. Reprinted with acknowledgement to Alison Margolskee. . . . .	62



Figure 4.1	Compartment model used for predicting HUT dynamics in the systemic circulation. The model includes five compartments representing the left heart (lh), arteries (a), and veins (v) in the upper (u) and lower (l) body. Flows are marked by $q$ , pressures by $p$ , volumes by $V$ , resistors by $R$ , compliances by $C$ . The opening and closing of the aortic (av) and mitral (mv) valves and prevention of retrograde flow through systemic veins are modeled via pressure-varying resistors. . . . .	66
Figure 4.2	Ranked total sensitivities, $\ \partial p_{au}/\partial \tilde{\theta}\ _2$ , for CV model. Ranked from most to least sensitive. 1: $E_{max}$ 2: $E_{min}$ 3: $C_{au}$ 4: $R_{aup}$ 5: $R_{vl}$ 6: $C_{al}$ 7: $C_{vu}$ 8: $C_{vl}$ 9: $T_R$ 10: $R_{al}$ 11: $R_{alp}$ 12: $V_{un,lh}$ . . . . .	71
Figure 4.3	Plot of Nonlinear Least Squares and Ensemble Transform Kalman Filter fit to Pressure data, $p_{au}$ , and Residual distributions. . . . .	79
Figure 4.4	Plots of ETKF results of unobserved states as described; upper left: $p_{al}$ , lower left: $p_{vl}$ , upper right: $V_{lv}$ , lower right: $p_{vu}$ . . . . .	80
Figure 4.5	Absolute value of residuals with $\sigma$ and $2\sigma$ from the filter fit for $p_{au}$ . Assuming the residuals are normally distributed, 68% of the data should fall under the $1\sigma$ line while 95% should fall under the $2\sigma$ line. . . . .	81
Figure 4.6	NLS estimate for $R_{aup}$ along with confidence bounds derived through DRAM compared to ETKF estimate for $R_{aup}$ with confidence intervals in log scale. . . . .	81
Figure 4.7	NLS estimate for $E_{min}$ along with confidence bounds derived through DRAM compared to ETKF estimate for $E_{min}$ with confidence intervals in log scale. . . . .	82
Figure 5.1	Schematic representation illustrating the interplay between absorption, distribution, binding, and elimination (excretion and metabolism) kinetics as well as dynamics of a drug. . . . .	92
Figure 5.2	Illustration of the absorption, distribution, and transport of a drug through the various barriers and membranes to its target. . . . .	94
Figure 6.1	Diagram representing the two compartment model. Absorption compartment, $A_a$ , represents the gut. Drug is taken into the absorption compartment and is transported into the central compartment at rate $k_a$ . The drug can diffuse into the peripheral compartment $A_{peripheral}$ at a rate $k_{12}$ and can diffuse back at rate $k_{21}$ . The drug will be eliminated from the body at rate $k_e$ . . . . .	108
Figure 6.2	Top: Population PK model fit for 16 subjects concentration profiles in log-space for concentration. Base model fit utilizes a 2-compartment oral absorption model with log-additive error. Bottom: Individual predictions vs. individual concentrations along with unity line (blue). Unity line represents the ideal situation where the model perfectly predicts the observations. . . . .	109
Figure 6.3	Left: Population PK model fit utilizing EKF for 16 subjects concentration profiles in log-space. Below is the individual predictions vs individual concentrations with unity line. Right: Population PK model fit utilizing UKF for 16 subjects concentration profiles in log-space. Below is the individual predictions vs individual concentrations with unity line (blue). Unity line represents the ideal situation where the model perfectly predicts the observations. . . . .	111

Figure 6.4	Left: Plasma concentration profile for Subject 1 including data, initial 2-compartment model (ODE), EKF absorption rate tracking model (EKF), UKF absorption rate tracking model (UKF), and Wiebull absorption 2-compartment model (Wiebull); prediction intervals are presented for the UKF calculated as $\hat{y}_{j j-1} \pm \sqrt{R_{(j j-1)}}$ Right: EKF and UKF filter predictions for Subject 1 along with prediction intervals for each filter. . . . .	112
Figure 6.5	Absorption rate profiles, $k_a$ , for Wiebull, EKF, and UKF models. This figure displays the temporal dynamics of the absorption rate of QD dose metformin for each individual. . . . .	112
Figure 6.6	Left: Plots of the fraction yet to be absorbed of metformin utilizing the EKF, UKF, and Wiebull ODE model. Right: Mass balance of drug over time for the EKF, UKF, and constrained EKF solutions. . . . .	113
Figure 6.7	Absorption rate profiles, $k_a$ , for Wiebull and constrained EKF models. . . . .	114
Figure 6.8	Top: Population PK model fit for 16 subjects concentration profiles in log-space for concentration. Model fit utilizes a 2-compartment oral absorption model with Wiebull absorption rate with log-additive error. Bottom: Individual predictions vs. individual concentrations with unity line(blue). Unity line represents the ideal situation where the model perfectly predicts the observations. . . . .	117

# Chapter 1

## Introduction, Motivation, and Outline

A model is a set of equations constructed to represent the interactions of various variables within a biological or physical process. Often, the model only incorporates the pertinent information for the system of interest, and will exclude variables or processes which are deemed insignificant or have little impact. Even if a model fully encapsulates the real world process, it may rely on initial conditions, boundary conditions, or parameters which are difficult to prescribe to high accuracy and precision [2].

The type of model constructed will also have an effect on the outcome and utility. Empirical models are created purely based upon observations rather than mathematically describable relationships of the system. Mechanistic models are constructed as representative abstractions of the underlying processes and are often compared to data for prediction purposes [8]. Mechanistic models are governed by physical relations and laws, and therefore often have less parameters than empirical models. Within this framework, models can then be classified as deterministic, thus having exact determinability, or stochastic, incorporating a level of statistical uncertainty within the predictions.

Resolving a model, we obtain a solution or single realization of the process outcome, out of a possible infinite number of realizations, without any understanding of the uncertainty associated with the model solution. The solution techniques introduce another level of uncertainty as numerical techniques have finite accuracy and precision. Other difficulties arise due to the size, complexity, and nonlinearity of the models, along with number of parameters [1].

In addition to the model, measurements from the system are collected at temporal and spatial locations. The measurements, themselves, introduce another element of uncertainty as sampling history, sampling equipment precision, and environmental conditions all introduce errors [9]. The computation of the model solution conditioned on these observed measurements defines the data assimilation or inverse problem which will be the focus for the remainder of this study. The inverse problem is defined as calculating the optimal parameter values to obtain the best possible fit of the model to a specified data.

The overall purpose of model building is to test hypotheses with regards to the system and parameters (within and between groups), and predict or simulate future outcomes [3]. Given the sources of

variability associated with the model solution due to the measurements and their collection, the model parameters, and the model assumptions may not fully represent the governing process [9], therefore the probability density function (pdf) of the model is considered. The pdf of the model can be used to extract information on the most likely estimate of the model state and its uncertainty [2].

For this thesis, the models of interest can be formulated as systems of ordinary differential equations (ODE), or solutions thereof [7]. Applying noise to the state space of the model alters the model framework from an ODE to a stochastic differential equation (SDE). This allows the model to account for the uncertainty associated with missing processes not considered, numerical techniques, and model parameters. Shifting to the SDE approach, then, allows the model to be represented by a probability density. While a class of linear SDEs possess analytical solutions [6], as well as optimal numerical solutions (Kalman filters) [5], many models are nonlinear and the solution for SDEs of this type require numerical methods.

The focus of this thesis will be on utilizing nonlinear filtering methodologies to quantify system dynamics along with its utilization within the inverse framework. Few studies are explicitly concerned with using filtering techniques for parameter estimation [4], the main purpose of this study is to illustrate its novelty and utility not only for uncertainty quantification of model dynamics, but its application to parameter estimation in general.

This thesis will continue as follows. Chapter 2 will cover a multitude of nonlinear filtering methods and their applications to a wide range of parameter estimation problems primarily within biological systems. A comprehensive comparison is carried out which highlights each filter's strengths and weaknesses on varying classes of problems.

Chapter 3 presents general background on human physiology of the cardiovascular system in general, as well as autonomic regulation. This biological background serves as motivation for the modeling done in Chapter 4.

Chapter 4 utilizes the biological background of Chapter 3 to construct a model to describe the baroreceptor and the body's regulation of blood pressure and heart rate during head-up tilt. The general model is derived and filtering is used to understand the control systems. The results are compared to alternate methods of modeling the control along with their respective uncertainties.

Chapter 5 presents a general background on pharmacokinetics and dynamics. This will provide the foundation for Chapter 6.

Chapter 6 provides a methodology for solving inverse problems for repeated measures or population studies and its application is shown in a population pharmacokinetic study of metformin.

Lastly, Chapter 7 provides a resolution as to what has been presented and concludes with possible future work which could be of interest.

## REFERENCES

- [1] Ellwein, L.M. *Cardiovascular and Respiratory Regulation, Modeling and Parameter Estimation*. PhD thesis, North Carolina State University, 2008.
- [2] Evensen, G. Data Assimilation: The Ensemble Kalman Filter. New York: Springer, 2009.
- [3] Gabrielsson, J. and Weiner, D. Pharmacokinetic and Pharmacodynamic Data Analysis: Concepts and Applications. Stockholm, Sweden: Swedish Pharmaceutical Press, 2006.
- [4] Haykin, S. Kalman Filtering and Neural Networks. New York: John Wiley and Sons, Inc., 2001.
- [5] Kalman, R.E. "A New Approach to Linear Filtering and Prediction Problems." ASME J. Basic Engineering. Vol. 82, 1960, Pgs. 34-45.
- [6] Klebaner, F.C. Introduction to Stochastic Calculus with Applications. London, UK: Imperial College Press, 2005.
- [7] Overgaard, R.V., Jonsson, N., Tornøe, C.W., and Madsen, H. "Nonlinear Mixed-Effects Models with Stochastic Differential Equations: Implementation of an Estimation Algorithm." Journal of Pharmacokinetics and Pharmacodynamics. Vol. 32, No. 1, 2005, Pgs. 85-107.
- [8] Riviere, J. Comparative Pharmacokinetics Principles, Techniques, and Applications. West Sussex, UK: John Wiley, and Sons, 2011.
- [9] Tornøe, C.W., Overgaard, R.V., Agerso, H., Nielsen, H.A., Madsen, H., and Jonsson, E.N. "Stochastic Differential Equations in NONMEM: Implementation, Application and Comparison with Ordinary Differential Equations." Pharmaceutical Research. Vol. 22, No. 8, 2005, Pgs.1247-1258.
- [10] Truskey, G.A., Yuan, F., and Katz, D.F. Transport Phenomena in Biological Systems. Upper Saddle River, NJ: Pearson Education, Inc., 2004.

## Chapter 2

# Nonlinear Filtering Methodologies for Parameter Estimation

### 2.1 Introduction

For many problems in science, the estimation of the state of a system given a set of system observations is ubiquitous. Given that mathematical models approximate the true dynamics of the underlying system and that any measurement of the system dynamics is noisy, we wish to find an optimal method to combine these to get more accurate estimates of the state of the system, and any model parameters. An optimal method to do this is to use the Bayes filter; however, the Bayes filter can rarely be solved analytically, and numerical approximation is often intractable, except for a small set of restrictive cases [3].

One solution to the Bayes filter is the celebrated Kalman filter [27]. Assuming that the model is linear and that the errors in both the model and the observations are Gaussian, the Bayes filter simplifies to the Kalman filter, which calculates the optimal state of the system by taking a weighted average of the probability distribution from the model and the probability distribution from the measurement. It is deterministic in nature and characterizes the entire optimal estimate through the propagation of the mean and covariance of the estimate at each step. However, if these restrictive assumptions do not hold and the model dynamics are nonlinear or the noise distributions are non-Gaussian, the Kalman filter fails. Several variants of the Kalman filter have been developed to overcome these shortcomings.

One such method is to approximate the nonlinear model dynamics by a linearization about the current state. This linear model is then propagated forward under the Kalman filter equations along with the observations and is used to approximate the optimal mean and covariance for the state of the system. This method still requires the assumption of Gaussian noise to hold for both the model and measurements, which may not be true as a normal distribution is not guaranteed to be maintained through a nonlinear transformation. This approach is known as the Extended Kalman Filter (EKF) [8,

12, 9, 19].

Another approach to handle the nonlinear model dynamics is via a statistical linearization [7]. Instead of linearizing the model dynamics, we perform a linearization of the distribution itself by carefully choosing a set of sigma points that characterize the distribution and capture the important features. By propagating these points through the unscented transform, we get an accurate representation of the posterior distribution. This is done for both the model and observations, and the resulting distributions are used in the classical Kalman filter equations. This approach still assumes Gaussian distributions and is known as the Unscented Kalman Filter (UKF) [7, 14, 11, 26, 38].

The last of the deterministic approaches to be discussed is the Cubature Kalman filter [3]. It is derived by applying the Gaussian distribution to the Bayes filter for any nonlinear function and exploiting the properties of the highly efficient cubature numerical integration technique for the multi-dimensional integral given in the Bayes filter. Much like the Unscented Kalman Filter, this method requires the calculation of cubature points to characterize the integrals, which are used to calculate the distributions more accurately, and finally used in the classical Kalman filter equations.

Another set of approaches has been derived by using sampling techniques, as opposed to deterministic methodologies, to characterize the distributions. These sampling based methods sample a large number of points from the assumed distribution and propagate them forward. The characterization of the distribution is now done using straightforward calculations of the mean and variance of these samples. The accuracy of these sample based approximate methods depends on the sampling as opposed to the previous approaches which relied upon the accuracy of the linearizations or the numerical integration. There are two types of these methods we will discuss, the Ensemble Kalman filter (EnKF) and the Ensemble Transform Kalman Filter (ETKF), though many other methods exist. For example, we refer the interested reader to [1, 6, 9, 10, 13] for more information on these methods and others.

For this study, since the systems dealt with will change sequentially in time, we shall focus our efforts on state-space models using discrete time. Therefore, difference equations shall mainly be presented to describe the dynamics of a system over time. This discrete formulation shall be used as measurements are collected at discrete times in application and the modeling framework can easily be extended to continuous time.

In this chapter, a comprehensive comparison study of the methods presented above will be performed on several problems. We shall draw conclusions about which methods give the best result for certain problems taking into account the assumptions, cpu time required for solutions, and the ability to solve the types of problems presented. The chapter is organized as follows. Background and derivation of the Bayes filter and Kalman filter will be presented in Section 2.2. Section 2.3 presents the deterministic methods previously discussed, and Section 2.4 the sampling based methods. The problem statement of interest will be presented in Section 2.5. The application of these methods to test problems will be presented in Section 2.6. Finally, Section 2.7 contains our concluding remarks.

## 2.2 Background and Derivation

### 2.2.1 Bayes Filter

The Bayes filter is an optimal method to combine a model along with measurements to get the best estimate of the state of the system, and the model parameters.

We start by defining the state-space representation as follows:

$$x_{i+1} = f(i, x_i, u_i, \theta) + w_i \quad (2.1)$$

$$y_{i+1} = h(i+1, x_{i+1}, u_{i+1}, \theta) + v_{i+1}, \quad (2.2)$$

where  $x_{i+1} \in \mathcal{R}^{n_x}$  and  $y_{i+1} \in \mathcal{R}^{n_y}$  are the model state and measurement, respectively,  $w_i$  and  $v_{i+1}$  are assumed to be independent and identically distributed (i.i.d.) noise processes with zero means and covariances  $Q_i$  and  $R_{i+1}$ ,  $u_i \in \mathcal{R}^{n_u}$  is an exogenous control, and  $\theta$  denote the model parameters. The functions  $f$  and  $h$  are assumed to be nonlinear in the state and observations.

The objective is to use the measurements,  $y_{1:i}$ , up to time  $i$ , to give an understanding of the state  $x_i$ . This requires calculating the distribution,  $p(x_i|y_{1:i})$ , assuming that the initial distribution  $p(x_0|y_0) = p(x_0)$ , which is just the distribution of the state without any observations at the current time, known as the prior. Given the initial distribution,  $p(x_i|y_{1:i})$  can be calculated in two steps: a prediction and an update.

Assuming time starts at  $i-1$ , with  $p(x_{i-1}|y_{1:i-1})$ , the prediction step involves using the model to calculate the prior probability density function (pdf) of the state at time  $i$  by using the Chapman-Kolmogorov equation [5]

$$p(x_i|y_{1:i-1}) = \int p(x_i|x_{i-1})p(x_{i-1}|y_{1:i-1})dx_{i-1}, \quad (2.3)$$

which utilizes the fact that  $p(x_i, x_{i-1}|y_{1:i-1}) = p(x_i|x_{i-1})$  since the model is a first order Markov process. The pdf  $p(x_i|x_{i-1})$  is given by the state-space model (2.1) with statistics governed by  $w_i$ .

Now given a measurement  $y_i$  becomes available at time  $i$ , Bayes' rule is applied to update the prior estimate and get our posterior

$$p(x_i|y_{1:i}) = \frac{p(y_i|x_i)p(x_i, y_{1:i-1})}{p(y_i, y_{1:i-1})}, \quad (2.4)$$

where  $p(y_i, y_{1:i-1}) = \int p(y_i, x_i)p(x_i|y_{1:i-1})dx_i$ .

The posterior is dependent upon the likelihood function which is defined by the measurement equation (2.2), with statistics given by  $v_{i+1}$ . Hence, the posterior updates the prior given a measurement to get the density at the current state [5] and the Bayes filter is simply a recursion relationship between (2.3) and (2.4).

The difficulty arises as each time we obtain a new measurement, the full posterior distribution would have to be recomputed. This is particularly troublesome in dynamic estimation where measurements are



obtained one at a time; when the number of time steps increases, the dimensionality of the full posterior distribution also increases leading to computationally intractable calculations [27].

### 2.2.2 The Kalman Filter

Assuming linear dynamics and Gaussian noise processes, the Bayes filter simplifies to the Kalman filter. Utilizing the work of Majda and Harlim [19], the Kalman filter is derived as follows. Operating with Gaussian distributions, the entire optimal estimate can be characterized through the propagation of the mean and covariance. Letting  $x_{i+1|i}$  be the state at time  $i + 1$  given the state at time  $i$ ,  $\hat{x}_{i+1|i}$  denotes the mean of the prior distribution, and  $P_{x_{i+1|i}}$  the covariance of the prior distribution, the state space can be formulated as:

$$x_{i+1|i} = Fx_{i|i} + w_i \quad (2.5)$$

$$y_{i+1} = Hx_{i+1} + v_{i+1}, \quad (2.6)$$

where  $w_i$  and  $v_{i+1}$  are normally distributed with mean 0 and covariances,  $Q$  and  $R$ , respectively, and  $F$  and  $H$  are matrix operators. For simplification, we shall use the following notation to describe distributions,  $w_i \sim N(0, Q)$  and  $v_{i+1} \sim N(0, R)$  where  $\sim$  denotes distributed and  $N(0, R)$  denotes normal with mean 0 and covariance  $R$ . This gives  $p(x_{i+1}) \sim N(\hat{x}_{i+1|i}, P_{x_{i+1|i}})$  with

$$P_{x_{i+1|i}} = \langle (x_{i+1} - \hat{x}_{i+1|i})(x_{i+1} - \hat{x}_{i+1|i})^T \rangle, \quad (2.7)$$

where  $\langle A \rangle$  denotes the mean of  $A$ .

Substituting (2.5) into (2.7), the following equation for the covariance prediction can be obtained,

$$P_{x_{i+1|i}} = \langle (Fx_{i|i} + w_{i+1} - F\hat{x}_{i|i})(Fx_{i|i} + w_{i+1} - F\hat{x}_{i|i})^T \rangle \quad (2.8)$$

$$= F \langle (x_{i|i} - \hat{x}_{i|i})(x_{i|i} - \hat{x}_{i|i})^T \rangle F^T + Q = FP_{x_{i|i}}F^T + Q. \quad (2.9)$$

Assuming Gaussian distributions, the distributions become

$$p(x_{i+1}) \propto e^{-\frac{1}{2}(x - \hat{x}_{i+1|i})^T (P_{x_{i+1|i}})^{-1} (x - \hat{x}_{i+1|i})} \quad (2.10)$$

$$p(y_{i+1}|x_{i+1}) \propto e^{-\frac{1}{2}(y_{i+1} - Hx)^T R^{-1} (y_{i+1} - Hx)}. \quad (2.11)$$

By applying Bayes formula,  $p(x_{i+1}|y_{i+1}) \propto p(x_{i+1})p(y_{i+1}|x_{i+1})$ , where  $\propto$  denotes proportionality, the posterior can be written as

$$p(x_{i+1}|y_{i+1}) \propto e^{-\frac{1}{2}J[x]}, \quad (2.12)$$

where  $J[x] = (x - \hat{x}_{i+1|i})^T (P_{x_{i+1|i}})^{-1} (x - \hat{x}_{i+1|i}) + (y_{i+1} - Hx)^T R^{-1} (y_{i+1} - Hx)$ .

The best estimate is obtained by maximizing the conditional density,  $p(x_{i+1}|y_{i+1})$ , which is the same

as minimizing  $J[x]$ . The necessary condition for  $J[x]$  to be minimized is

$$\frac{dJ}{dx} = P_{x_{i+1|i}}^{-1} (x - \hat{x}_{i+1|i}) + (x - \hat{x}_{i+1|i})^T P_{x_{i+1|i}}^{-1} - H^T R^{-1} (y_{i+1} - Hx) + (y_{i+1} - Hx)^T R^{-1} (-H) \quad (2.13)$$

$$= 2(P_{x_{i+1|i}})^{-1} (x - \hat{x}_{i+1|i}) - 2H^T R^{-1} (y_{i+1} - Hx) = 0, \quad (2.14)$$

which implies

$$(P_{x_{i+1|i}})^{-1} (x - \hat{x}_{i+1|i}) = H^T R^{-1} (y_{i+1} - Hx).$$

Isolating the dependent variable  $x$  yields

$$(P_{x_{i+1|i}}^{-1} + H^T R^{-1} H)x = P_{x_{i+1|i}}^{-1} \hat{x}_{i+1|i} + H^T R^{-1} y_{i+1}.$$

Adding and subtracting  $H^T R^{-1} H \hat{x}_{i+1|i}$ , the inverse of the leading term  $(P_{x_{i+1|i}}^{-1} + H^T R^{-1} H)$  is multiplied through to obtain

$$\begin{aligned} \hat{x}_{i+1|i+1} = & (P_{x_{i+1|i}}^{-1} + H^T R^{-1} H)^{-1} P_{x_{i+1|i}}^{-1} \hat{x}_{i+1|i} + (P_{x_{i+1|i}}^{-1} + H^T R^{-1} H)^{-1} H^T R^{-1} y_{i+1} + \\ & [(P_{x_{i+1|i}}^{-1} + H^T R^{-1} H)^{-1} H^T R^{-1} H \hat{x}_{i+1|i} - (P_{x_{i+1|i}}^{-1} + H^T R^{-1} H)^{-1} H^T R^{-1} H \hat{x}_{i+1|i}], \end{aligned}$$

where  $\hat{x}_{i+1|i+1}$  is the mean of the posterior distribution.

Rearranging the terms gives

$$\begin{aligned} \hat{x}_{i+1|i+1} = & (P_{x_{i+1|i}}^{-1} + H^T R^{-1} H)^{-1} P_{x_{i+1|i}}^{-1} \hat{x}_{i+1|i} + (P_{x_{i+1|i}}^{-1} + H^T R^{-1} H)^{-1} H^T R^{-1} H \hat{x}_{i+1|i} + \\ & (P_{x_{i+1|i}}^{-1} + H^T R^{-1} H)^{-1} H^T R^{-1} (y_{i+1} - H \hat{x}_{i+1|i}). \end{aligned}$$

Adding the  $\hat{x}_{i+1|i}$  terms together and simplifying leads to

$$\hat{x}_{i+1|i+1} = \hat{x}_{i+1|i} + K_{i+1} (y_{i+1} - H \hat{x}_{i+1|i}), \quad (2.15)$$

where  $K_{i+1}$  is defined as

$$K_{i+1} = (P_{x_{i+1|i}}^{-1} + H^T R^{-1} H)^{-1} H^T R^{-1}, \quad (2.16)$$

also known as the Kalman gain. Equation (2.15) is the mean update for the state. A more common expression for the Kalman gain can be obtained by multiplying  $K_{i+1}$  by  $(HP_{x_{i+1|i}} H^T + R)(HP_{x_{i+1|i}} H^T + R)^{-1}$ ;

$$K_{i+1} = (P_{x_{i+1|i}}^{-1} + H^T R^{-1} H)^{-1} H^T R^{-1} (HP_{x_{i+1|i}} H^T + R)(HP_{x_{i+1|i}} H^T + R)^{-1}. \quad (2.17)$$

Multiplying  $R$  by  $(P_{x_{i+1|i}} H^T)^{-1} P_{x_{i+1|i}} H^T$  in  $(HP_{x_{i+1|i}} H^T + R)(HP_{x_{i+1|i}} H^T + R)^{-1}$  gives

$$(HP_{x_{i+1|i}} H^T + R)(HP_{x_{i+1|i}} H^T + R)^{-1} = (HP_{x_{i+1|i}} H^T + R(P_{x_{i+1|i}} H^T)^{-1} P_{x_{i+1|i}} H^T)(HP_{x_{i+1|i}} H^T + R)^{-1}. \quad (2.18)$$

Substituting (2.18) into (2.17) and expanding yields

$$K_{i+1} = (P_{x_{i+1}|i}^{-1} + H^T R^{-1} H)^{-1} [H^T R^{-1} H P_{x_{i+1}|i} H^T + H^T (P_{x_{i+1}|i}^{-1})^{-1} P_{x_{i+1}|i} H^T] (H P_{x_{i+1}|i} H^T + R)^{-1}. \quad (2.19)$$

Substituting  $(P_{x_{i+1}|i} H^T)^{-1} = (H^T)^{-1} P_{x_{i+1}|i}^{-1}$  into (2.19) yields

$$K_{i+1} = (P_{x_{i+1}|i}^{-1} + H^T R^{-1} H)^{-1} [H^T R^{-1} H (P_{x_{i+1}|i} H^T) + H^T (H^T)^{-1} P_{x_{i+1}|i}^{-1} (P_{x_{i+1}|i} H^T)] (H P_{x_{i+1}|i} H^T + R)^{-1}.$$

Rearranging terms results in

$$K_{i+1} = (P_{x_{i+1}|i}^{-1} + H^T R^{-1} H)^{-1} [(H^T R^{-1} H + P_{x_{i+1}|i}^{-1}) (P_{x_{i+1}|i} H^T)] (H P_{x_{i+1}|i} H^T + R)^{-1}.$$

Simplifying, we finally arrive at

$$K_{i+1} = P_{x_{i+1}|i} H^T (H P_{x_{i+1}|i} H^T + R)^{-1}, \quad (2.20)$$

which is the more common expression for the Kalman Gain.

By substituting (2.15) into the covariance formula,

$$\langle (x_{i+1} - \hat{x}_{i+1|i+1})(x_{i+1} - \hat{x}_{i+1|i+1})^T \rangle, \quad (2.21)$$

we obtain

$$(x_{i+1} - \hat{x}_{i+1|i+1}) = x_{i+1} - \hat{x}_{i+1|i} - K_{i+1}(y_{i+1} - Hx_{i+1} - H(\hat{x}_{i+1|i} - x_{i+1})).$$

Let  $e_{i+1|i+1} = x_{i+1} - \hat{x}_{i+1|i+1}$  be the error between the true state and the estimated state. Using the output equation (2.6) leads to

$$e_{i+1|i+1} = (I - K_{i+1}H)e_{i+1|i} - K_{i+1}(Hx_{i+1} + v_{i+1} - Hx_{i+1}) \quad (2.22)$$

$$e_{i+1|i+1} = (I - K_{i+1}H)e_{i+1|i} - K_{i+1}v_{i+1}. \quad (2.23)$$

Using (2.23), the covariance update is given by

$$\langle e_{i+1|i+1} e_{i+1|i+1}^T \rangle = (I - K_{i+1}H) \langle e_{i+1|i} e_{i+1|i}^T \rangle (I - K_{i+1}H)^T + K_{i+1} R K_{i+1}^T \quad (2.24)$$

$$\langle e_{i+1|i+1} e_{i+1|i+1}^T \rangle = (I - K_{i+1}H) \langle e_{i+1|i} e_{i+1|i}^T \rangle - (I - K_{i+1}H) \langle e_{i+1|i} e_{i+1|i}^T \rangle (K_{i+1}H)^T + K_{i+1} R K_{i+1}^T. \quad (2.25)$$

Substituting (2.16) into  $(I - K_{i+1}H)$  and simplifying results in

$$(I - K_{i+1}H) = (P_{x_{i+1}|i}^{-1} + H^T R^{-1} H)^{-1} (P_{x_{i+1}|i}^{-1} + H^T R^{-1} H) - (P_{x_{i+1}|i}^{-1} + H^T R^{-1} H)^{-1} H^T R^{-1} H \quad (2.26)$$

$$= (P_{x_{i+1}|i}^{-1} + H^T R^{-1} H)^{-1} P_{x_{i+1}|i}^{-1}. \quad (2.27)$$

Applying the definition of the covariance,  $\langle e_{i+1|i} e_{i+1|i}^T \rangle = P_{x_{i+1|i}}$ , along with substituting (2.27) and expanding (2.25) yields

$$\begin{aligned}
\langle e_{i+1|i+1} e_{i+1|i+1}^T \rangle &= (I - K_{i+1}H)P_{x_{i+1|i}} - ((P_{x_{i+1|i}}^{-1} + H^T R^{-1} H)^{-1} P_{x_{i+1|i}}^{-1}) P_{x_{i+1|i}} H^T K_{i+1}^T + K_{i+1} R K_{i+1}^T \\
&= (I - K_{i+1}H)P_{x_{i+1|i}} - (P_{x_{i+1|i}}^{-1} + H^T R^{-1} H)^{-1} H^T K_{i+1}^T \\
&\quad + ((P_{x_{i+1|i}}^{-1} + H^T R^{-1} H)^{-1} H^T R^{-1}) R K_{i+1}^T \\
&= (I - K_{i+1}H)P_{x_{i+1|i}} - (P_{x_{i+1|i}}^{-1} + H^T R^{-1} H)^{-1} H^T K_{i+1}^T \\
&\quad + (P_{x_{i+1|i}}^{-1} + H^T R^{-1} H)^{-1} H^T K_{i+1}^T.
\end{aligned}$$

Simplifying, the covariance update becomes

$$P_{x_{i+1|i+1}} = (I - K_{i+1}H)P_{x_{i+1|i}}. \quad (2.28)$$

In summary, the above derivation for the Kalman filter essentially contains two steps.

*Prediction*

$$\hat{x}_{i+1|i} = F x_{i|i} \quad (2.29)$$

$$P_{x_{i+1|i}} = F P_{x_{i|i}} F^T + Q \quad (2.30)$$

*Update*

$$\hat{x}_{i+1|i+1} = \hat{x}_{i+1|i} + K_{i+1}(y_{i+1} - H\hat{x}_{i+1|i}) \quad (2.31)$$

$$K_{i+1} = P_{x_{i+1|i}} H^T (H P_{x_{i+1|i}} H^T + R)^{-1} \quad (2.32)$$

$$P_{x_{i+1|i+1}} = (I - K_{i+1}H)P_{x_{i+1|i}}. \quad (2.33)$$

As stated, however, this only holds if the model dynamics and observation equation are both linear and the noise processes are Gaussian. For cases when these do not hold, modifications to the Kalman filter have been developed.

## 2.3 Deterministic Kalman Filters

### 2.3.1 The Extended Kalman Filter

Because of the Kalman filter's optimality and simplicity, the extended Kalman filter (EKF) maintains the basic framework and idea of the original Kalman filter, but uses a first order linearization of the model dynamics to approximate the error statistics. Following Evensen [9], the extended Kalman filter

is derived as follows. Assuming a general nonlinear system as below:

$$x_{i+1}^t = f(i, x_i^t, u_i, \theta) + w_i \quad (2.34)$$

$$y_{i+1}^t = h(i+1, x_{i+1}^t, u_i, \theta) + v_{i+1}, \quad (2.35)$$

and assuming this system is modeled by the approximate equation

$$\hat{x}_{i+1}^- = f(i, \hat{x}_i, u_i, \theta), \quad (2.36)$$

subtracting (2.36) from (2.34) obtains

$$x_{i+1}^t - \hat{x}_{i+1}^- = f(i, x_i^t, u_i, \theta) - f(i, \hat{x}_i, u_i, \theta) + w_i. \quad (2.37)$$

A Taylor expansion can be performed to approximate the system

$$f(x) = f(x_0) + \frac{df}{dx}(x_0)(x - x_0) + \frac{1}{2}(x - x_0)^T F_{xx}(x_0)(x - x_0)^T + O(\|x - x_0\|^3),$$

where  $F_{xx}$  is used to denote the second derivative, or Hessian matrix for multiple dimensions. Applying this expansion to the original system leads to

$$x_{i+1}^t - \hat{x}_{i+1}^- = f(i, \hat{x}_i, u_i, \theta) + \frac{df}{dx}(\hat{x}_i)(x_i^t - \hat{x}_i) + \frac{1}{2}(x_i^t - \hat{x}_i)F_{xx}(\hat{x}_i)(x_i^t - \hat{x}_i)^T + O(\|x - x_0\|^3) - f(i, \hat{x}_i, u_i, \theta) + w_i.$$

Squaring both sides and taking the expected value leads to the following equation

$$\begin{aligned} P_{x_{i+1}|i} &= F_x(\hat{x}_i)E[(x_i^t - \hat{x}_i)(x_i^t - \hat{x}_i)]^T F_x(\hat{x}_i)^T + \frac{1}{2}F_x(\hat{x}_i)E[(x_i^t - \hat{x}_i)(x_i^t - \hat{x}_i)^T]F_{xx}^T(\hat{x}_i)E[(x_i^t - \hat{x}_i)] \\ &\quad + \frac{1}{4}E[(x_i^t - \hat{x}_i)(x_i^t - \hat{x}_i)^T]F_{xx}F_{xx}^T E[(x_i^t - \hat{x}_i)(x_i^t - \hat{x}_i)^T] + \dots + Q, \end{aligned}$$

which simplifies by discarding the moments of third or higher order

$$P_{x_{i+1}|i} \approx F_x(\hat{x}_i)P_{x_{ij}|i}F_x(\hat{x}_i)^T + Q, \quad (2.38)$$

where  $F_x(\hat{x}_i) = \frac{\partial f(i, x)}{\partial x}|_{x=\hat{x}_i}$  is the Jacobian,  $Q$  is the model error covariance, and  $P_{x_{i+1}|i}$  is the predicted error covariance.

Applying the same procedure to the nonlinear observation equation  $h$ , we utilize a linearization of the observation equation to be used in the update as follows

$$H_{i+1} = \frac{\partial h(i, x)}{\partial x}|_{x=\hat{x}_{i+1}^-}.$$

Using the above derivations in the classical Kalman filter equations, we obtain the extended Kalman

filter. While the initial state estimation portion of the algorithm is unchanged, these Jacobians are utilized in the initial covariance estimation and in the estimation update for both the covariance and the state, through the gain. Though utilizing the same procedure as the Kalman filter, the extended Kalman filter is sub-optimal for nonlinear problems, and reduces to the Kalman filter for linear problems.

The algorithm for the extended Kalman filter is summarized as follows:

*Initialize:* for  $i = 0$

$$\hat{x}_0 = E[x_0]$$

$$P_0 = E[(x_0 - E[x_0])(x_0 - E[x_0])^T]$$

*algorithm:* for  $i = 1, 2, 3, \dots$

State Estimation

$$\hat{x}_i^- = f(i, \hat{x}_{i-1})$$

Covariance Estimation

$$P_i^- = F_{i,i-1} P_{i-1} F_{i,i-1}^T + Q_{i-1}$$

where  $F$  is the linearization of the model w.r.t. the state

$$F_{i,i-1} = \left. \frac{\partial f(i, x)}{\partial x} \right|_{x=\hat{x}_{i-1}}$$

Kalman Gain Matrix

$$K = P_i^- H_i^T [H_i P_i^- H_i^T + R_i]^{-1}$$

where  $H$  is the linearization of the observation w.r.t. the state

$$H_i = \left. \frac{\partial h(i, x)}{\partial x} \right|_{x=\hat{x}_i^-}$$

State Estimation Update

$$\hat{x}_i = \hat{x}_i^- + K[y_i - h(i, \hat{x}_i^-)]$$

Covariance Estimation Update

$$P_i = [I - KH_i] P_i^-$$

Reviewing the algorithm, this extension of the Kalman filter is applicable for nonlinear systems, though still requires Gaussian distributions for both the model and observations. However, the disadvantage of the extended Kalman filter is that it is approximating the nonlinear model by a linearized counterpart, through a first order Taylor expansion. The success of the extended Kalman filter relies heavily on the assumption that the linearization of the nonlinear state-space model deviates from linearity no more than first order [14]. In cases where the nonlinearities deviate from linearity greater than first order, or the initial estimates cause higher order terms to be significant, the filter will achieve less accurate results, and can even diverge and fail to achieve meaningful results [38]. This is likely due to

the approximation of the error statistics by the linearized model, since a Gaussian distribution cannot be guaranteed once propagated through a nonlinear operator.

To increase the accuracy of nonlinear models, another Kalman filter has been constructed that better preserves the distribution statistics as it passes through the nonlinearities. Unlike the EKF, this new filter maintains at least second order accuracy for all distributions, and at least third order accuracy for Gaussian distributions [14].

### 2.3.2 The Unscented Kalman Filter

The unscented Kalman filter addresses the shortcomings of the EKF through the 'unscented transformation.' Following the work by Haykin [14], the unscented Kalman filter is derived assuming the errors are Gaussian random variables (GRV). Instead of using a linear approximation to the nonlinear model, a set of sample points is constructed which will completely capture the true mean and covariance of the GRV, and once propagated through the nonlinear model, will capture the posterior mean and covariance to 3rd order for any nonlinearity [38]. The advantages of the unscented Kalman filter are not just the increase of accuracy, but also the decrease in complexity by not requiring the calculation of a derivative, or Jacobian. To better understand, we shall explain the unscented transformation.

The unscented transformation (UT) is a method used to calculate the statistics of a random variable which undergoes a nonlinear transformation [11]. Assuming that  $x$  is a random variable with dimension  $L$ , which has mean  $\hat{x}$  and covariance,  $P_x$ , this random variable gets propagated through a nonlinear function,  $y = g(x)$ . To calculate the statistics of  $y$ , a matrix  $\chi$  is formed of  $2L + 1$  sigma vectors  $\chi_i$ . This matrix  $\chi$  is constructed as follows,

$$\chi = [\hat{x}, \hat{x}\mathbf{1}_{1 \times L} + (\sqrt{(L + \lambda)P_x})_L, \hat{x}\mathbf{1}_{1 \times L} - (\sqrt{(L + \lambda)P_x})_L], \quad (2.39)$$

where  $\hat{x}$  is a column vector,  $\hat{x}\mathbf{1}_{1 \times L}$  is a matrix of the column vector  $\hat{x}$ , and  $(\sqrt{(L + \lambda)P_x})_L$  is an  $L \times L$  matrix. The corresponding weights ( $W_i$ ) for the sigma vectors are as follows

$$W_0^{(m)} = \frac{\lambda}{(L + \lambda)} \quad (2.40)$$

$$W_0^{(c)} = \frac{\lambda}{(L + \lambda)} + (1 - \alpha^2 + \beta) \quad (2.41)$$

$$W_i^{(m)} = W_i^{(c)} = \frac{1}{2(L + \lambda)} \quad i = 1, \dots, 2L, \quad (2.42)$$

where  $\lambda = \alpha^2(L + \kappa) - L$  is a scaling parameter. The tuning parameter,  $\alpha$ , is used to determine the spread of the sigma points around  $\hat{x}$ , and takes values between  $1 \geq \alpha \geq 10^{-4}$  depending on the problem. The

tuning parameter,  $\kappa$ , is a secondary scaling parameter which is optimally set to  $3 - L$  [14]. Lastly,  $\beta$  is used to incorporate prior knowledge of the distribution of  $x$  (for Gaussian distributions,  $\beta = 2$  is optimal) [38]. From our matrix of sigma points (2.39),  $(\sqrt{(L + \lambda)P_x})_i$  is the  $i$ th row of the matrix square root [38]. The sigma vectors are then propagated through the nonlinear function accordingly,

$$y_i = g(\chi_i), \quad i = 0, \dots, 2L, \quad (2.43)$$

with the mean and covariance of  $y$  being approximated using a weighted sample mean and covariance of the posterior sigma points,

$$\hat{y} \approx \sum_{i=0}^{2L} W_i^{(m)} y_i \quad (2.44)$$

$$P_y \approx \sum_{i=0}^{2L} W_i^{(c)} (y_i - \hat{y})(y_i - \hat{y})^T. \quad (2.45)$$

As stated earlier, the UT results in approximations that are accurate to the third order for Gaussian inputs for all nonlinearities, and accurate to at least second order for all other inputs [9]. Extending the UT for use in the Unscented Kalman filter (UKF) is straightforward, and is shown below (assuming additive



Gaussian noise),

*Initialize:* for  $t = 0$

$$\hat{x}_0 = E[x_0]$$

$$P_0 = E[(x_0 - E[x_0])(x_0 - E[x_0])^T]$$

*algorithm:* for  $t = 1, 2, 3, \dots$

Calculate Sigma Points

$$\chi_{t-1} = [\hat{x}, \hat{x} + (\sqrt{(L + \lambda)P_{t-1}})_L, \hat{x} - (\sqrt{(L + \lambda)P_{t-1}})_L]$$

time-update equations

$$\chi_{t,t-1}^* = F(\chi_{t-1}, u_t, w_t)$$

where  $u_t$  is an exogenous input and  $w_t$  are parameters

$$\hat{x}_t^- = \sum_{i=0}^{2L} W_i^{(m)} \chi_{i,t|t-1}^*$$

$$P_t^- = \sum_{i=0}^{2L} W_i^{(c)} (\chi_{i,t|t-1}^* - \hat{x}_t^-)(\chi_{i,t|t-1}^* - \hat{x}_t^-)^T + Q$$

time-update equations for observation: augment sigma points

$$\chi_{t|t-1} = [\chi_{0,t|t-1}^*, \chi_{0,t|t-1}^* + (\sqrt{(L + \lambda)P_t^-})_L, \hat{x} - (\sqrt{(L + \lambda)P_t^-})_L]$$

$$Y_{t|t-1} = g(\chi_{t,t-1})$$

$$\hat{y}_t^- = \sum_{i=0}^{2L} W_i^{(m)} Y_{i,t|t-1}$$

measurement-update equations

$$P_{\hat{y}_t \hat{y}_t} = \sum_{i=0}^{2L} W_i^{(c)} (Y_{i,t|t-1} - \hat{y}_t^-)(Y_{i,t|t-1} - \hat{y}_t^-)^T + R$$

$$P_{x_t y_t} = \sum_{i=0}^{2L} W_i^{(c)} (\chi_{i,t|t-1} - \hat{x}_t^-)(Y_{i,t|t-1} - \hat{y}_t^-)^T$$

$$K_t = P_{x_t y_t} P_{\hat{y}_t \hat{y}_t}^{-1}$$

$$\hat{x}_t = \hat{x}_t^- + K_t(y_t - \hat{y}_t^-)$$

$$P_t = P_t^- - K_t P_{\hat{y}_t \hat{y}_t} K_t^T$$

where  $Q$  is the process noise covariance and  $R$  is the measurement noise covariance.

The unscented Kalman filter as presented assumes additive Gaussian noise. There are multiple variations of this algorithm for numerical purposes, one of which is the square root unscented Kalman filter.

Also, a more general form of the UKF is also available, which does not assume additive noise, but propagates the measurement and process covariance through the nonlinear function. These extensions can be found in most of our referenced materials [14, 11, 26, 38, 30].

### 2.3.3 The Cubature Kalman Filter

Similar to the previous deterministic filters, the cubature Kalman filter (CKF) relies upon an approximation of the nonlinear function and is derived following the work of Arasaratnam [3]. However, unlike the previous methods, the CKF closely follows the Bayes filter theory and takes advantage of the assumption of a normal distribution using numerical integration techniques to calculate the time and measurement updates. This underlying assumption of a Gaussian distribution for the predictive density and the measurement density is central as it leads to a Gaussian posterior distribution [3].

The prediction step, or time update, is focused on calculating the mean  $\hat{x}_{i+1|i}$  and covariance  $P_{i+1|i}$  of the predictive density

$$\hat{x}_{i+1|i} = E[x_{i+1}|u_{1:i}, y_{1:i}]. \quad (2.46)$$

Substituting the model (2.63) into (2.46), obtains

$$\hat{x}_{i+1|i} = E[f(i, x_i, u_i, \theta) + w_i|u_{1:i}, y_{1:i}] = E[f(i, x_i, u_i, \theta)|u_{1:i}, y_{1:i}].$$

This result follows because  $w_i$  is assumed to be a zero-mean noise process that is uncorrelated with previous measurements. The expectation becomes

$$\begin{aligned} \hat{x}_{i+1|i} &= \int_{\mathbb{R}^{n_x}} f(i, x_i, u_i, \theta) p(x_i|u_{1:i}, y_{1:i}) dx_i \\ &= \int_{\mathbb{R}^{n_x}} f(i, x_i, u_i, \theta) \mathbb{N}(x_i; \hat{x}_{i|i}, P_{i|i}) dx_i, \end{aligned}$$

where  $\mathbb{N}(\cdot, \cdot, \cdot)$  is standard notation for a Gaussian density. Following the same procedure, the predictive covariance is

$$P_{i+1|i} = E[(x_{i+1} - \hat{x}_{i+1|i})(x_{i+1} - \hat{x}_{i+1|i})^T | u_{1:i}, y_{1:i}].$$

Again, substituting (2.63) in for  $x_{i+1}$ , using  $f(x_i)$  for shorthand to represent  $f(i, x_i, u_i, \theta)$  leads to

$$\begin{aligned} P_{i+1|i} &= E[(f(x_i) + w_i - \hat{x}_{i+1|i})(f(x_i) + w_i - \hat{x}_{i+1|i})^T | u_{1:i}, y_{1:i}] \\ &= E[f(x_i)f(x_i)^T + f(x_i)w_i^T - f(x_i)\hat{x}_{i+1|i}^T + w_i f(x_i)^T \\ &\quad + w_i w_i^T - w_i \hat{x}_{i+1|i}^T - \hat{x}_{i+1|i} f(x_i)^T - \hat{x}_{i+1|i} w_i^T + \hat{x}_{i+1|i} \hat{x}_{i+1|i}^T | u_{1:i}, y_{1:i}]. \end{aligned}$$

Assuming that  $w_i$  is independent of both  $f(x_i)$  and  $\hat{x}_{i+1|i}$ , we can use  $E[xy] = E[x]E[y]$  and  $E[E[x]] = E[x]$ . Knowing that  $w_i \sim N(0, Q)$  and  $\hat{x}_{i+1|i} = E[f(x_i)|u_{1:i}, y_{1:i}]$ , the previous expression simplifies to be

$$\begin{aligned} P_{i+1|i} &= E[f(x_i)f(x_i)^T - f(x_i)\hat{x}_{i+1|i}^T + w_i w_i^T - \hat{x}_{i+1|i}f(x_i)^T + \hat{x}_{i+1|i}\hat{x}_{i+1|i}^T | u_{1:i}, y_{1:i}] \\ &= E[f(x_i)f(x_i)^T] - E[f(x_i)\hat{x}_{i+1|i}^T] + E[w_i w_i^T] - E[\hat{x}_{i+1|i}f(x_i)^T] + E[\hat{x}_{i+1|i}\hat{x}_{i+1|i}^T]. \end{aligned}$$

Further simplifying  $-2E[f(x_i)\hat{x}_{i+1|i}^T] + E[\hat{x}_{i+1|i}\hat{x}_{i+1|i}^T]$  using  $E[f(x_i)]E[\hat{x}_{i+1|i}^T] = \hat{x}_{i+1|i}\hat{x}_{i+1|i}^T$ , gives

$$P_{i+1|i} = \int_{\mathfrak{R}^{n_x}} f(i, x_i, u_i, \theta) f(i, x_i, u_i, \theta)^T \mathbb{N}(x_i; \hat{x}_{i|i}, P_{i|i}) dx_i - \hat{x}_{i+1|i}\hat{x}_{i+1|i}^T + Q_i.$$

For the measurement update, assuming measurement errors are from Gaussian distributions, the likelihood function can be written as

$$p(y_{i+1}|u_{1:i}, y_{1:i}) = \mathbb{N}(y_{i+1}; \hat{y}_{i+1}, P_{yy,i+1|i}),$$

where the measurement prediction, calculated using the same procedure as the prediction step, is

$$\hat{y}_{i+1} = \int_{\mathfrak{R}^{n_x}} h(i+1, x_{i+1}, u_{i+1}, \theta) \mathbb{N}(x_{i+1}; \hat{x}_{i+1|i}, P_{i+1|i}) dx_{i+1}.$$

The associated covariance, calculated using the same procedure as the prediction step, is given by

$$P_{yy,i+1|i} = \int_{\mathfrak{R}^{n_x}} h(x_{i+1})h(x_{i+1})^T \times \mathbb{N}(x_{i+1}; \hat{x}_{i+1|i}, P_{i+1|i}) dx_{i+1} - \hat{y}_{i+1}\hat{y}_{i+1}^T + R_i.$$

Therefore, the joint conditional Gaussian density of the state and measurement is given by

$$\begin{aligned} p\left([x_{i+1}^T y_{i+1}^T]^T | y_{1:i}, u_{1:i}\right) &= \left( \mathbb{N}\left(\begin{bmatrix} \hat{x}_{i+1|i} \\ \hat{y}_{i+1} \end{bmatrix}, \right. \right. \\ &\quad \left. \left. \begin{bmatrix} P_{i+1|i} & P_{xy,i+1|i} \\ P_{xy,i+1|i}^T & P_{yy,i+1|i} \end{bmatrix} \right) \right), \end{aligned}$$

where the cross covariance is calculated as follows, substituting (2.64),

$$\begin{aligned} P_{xy,i+1|i} &= E[(x_{i+1} - \hat{x}_{i+1|i})(y_{i+1} - \hat{y}_{i+1})] \\ &= E[(x_{i+1} - \hat{x}_{i+1|i})(h(x_{i+1}) + v_{i+1} - \hat{y}_{i+1})], \end{aligned}$$

where carrying out the calculation, assuming  $v_{i+1}$  is independent of  $x_{i+1}$  and  $\hat{x}_{i+1|i}$ , and also noting that

$E(x_{i+1}|y_{1:i}, u_{1:i}) = \hat{x}_{i+1|i}$  and  $E(h(x_{i+1})|y_{1:i}, u_{1:i}) = \hat{y}_{i+1}$ , we obtain

$$\begin{aligned} P_{xy,i+1|i} &= E(x_{i+1}h(x_{i+1})^T + x_{i+1}v_{i+1}^T - x_{i+1}\hat{y}_{i+1}^T - \hat{x}_{i+1|i}h(x_{i+1})^T - \hat{x}_{i+1|i}v_{i+1}^T + \hat{x}_{i+1|i}\hat{y}_{i+1}) \\ &= E(x_{i+1}h(x_{i+1})^T) - E(x_{i+1}\hat{y}_{i+1}^T) - E(\hat{x}_{i+1|i}h(x_{i+1})^T) + E(\hat{x}_{i+1|i}\hat{y}_{i+1}) \\ &= \int_{\mathbb{R}^{n_x}} x_{i+1}h(i+1, x_{i+1}, u_{i+1}, \theta)^T \mathbb{N}(x_{i+1}; \hat{x}_{i+1|i}, P_{i+1|i}) dx_{i+1} - \hat{x}_{i+1|i}\hat{y}_{i+1}. \end{aligned}$$

Given a new measurement  $y_{i+1}$ , the posterior density  $p(x_{i+1}|y_{1:i+1}, u_{1:i+1})$  is calculated from the Bayesian filter, resulting in

$$p(x_{i+1}|y_{1:i+1}, u_{1:i+1}) = \mathbb{N}(x_{i+1}; \hat{x}_{i+1|i+1}, P_{i+1|i+1}), \quad (2.47)$$

where

$$\hat{x}_{i+1|i+1} = \hat{x}_{i+1|i} + K_{i+1}(y_{i+1} - \hat{y}_{i+1|i}) \quad (2.48)$$

$$P_{i+1|i+1} = P_{i+1|i} - K_{i+1}P_{yy,i+1|i}K_{i+1}^T \quad (2.49)$$

$$K_{i+1} = P_{xy,i+1|i}P_{yy,i+1|i}^{-1}, \quad (2.50)$$

which, if  $f(\dots)$  and  $h(\dots)$  are linear functions of the state, simplifies to the classical Kalman filter.

The remaining question now becomes how to calculate an integral of the form,

$$\int_{\mathbb{R}^n} g(x)\mathbb{N}(x)dx = \int_{\mathbb{R}^n} g(x)\exp(-x^Tx)dx.$$

Arasaratnam [3, 4] proposes that the best way to do this is (i) transform it into a more familiar spherical-radial integration form, and (ii) subsequently apply a third-degree spherical-radial rule .

First, a transformation must be made to change the variables from the Cartesian space  $x \in \mathbb{R}^n$  to a radius  $r$  and direction  $y$  as follows: let  $x = ry$  with  $y^Ty = 1$ , so that  $x^Tx = r$  for  $r \in [0, \infty)$  [3]. Then, the integral becomes

$$I(f) = \int_0^\infty \int_{U_n} f(ry)r^{n-1}\exp(-r^2)d\sigma(y)dr,$$

where  $U_n$  is the surface of the sphere defined by  $U_n = \{y \in \mathbb{R}^n | y^Ty = 1\}$  and  $\sigma(\dots)$  is the spherical surface measure [3]. This integral can be broken up into a radial component and spherical component which can subsequently be computed numerically using a cubature rule and quadrature rule. The radial integral is given by

$$I = \int_0^\infty S(r)r^{n-1}\exp(-r^2)dr,$$

where  $S(r)$  is defined by the spherical integral with unit weighting function  $w(y) = 1$ ,

$$S(r) = \int_{U_n} f(ry) d\sigma(y).$$

Carrying out both computations and combining them into a third-degree spherical-radial rule, the standard Gaussian weighted integral is calculated

$$I_{\mathbb{N}}(f) = \int_{\mathbb{R}^n} f(x) \times \mathbb{N}(x; 0, I) dx \approx \sum_{i=1}^m \omega_i f(\xi_i),$$

where

$$\begin{aligned} \xi_i &= \sqrt{\frac{m}{2}} [1]_i \\ \omega_i &= \frac{1}{m}, \quad i = 1, 2, \dots, m = 2n. \end{aligned}$$

Here  $[1]_i$  denotes a generator, where a generator  $\mathbf{u}$  in a fully symmetric region is defined by  $\mathbf{u} = (u_1, u_2, \dots, u_r, 0, \dots, 0) \in \mathbb{R}^n$  with  $u_i \geq u_{i+1} > 0, i = 1, 2, \dots, (r-1)$ . For example,  $[1] \in \mathbb{R}^2$  is represented by the points

$$\left( \begin{pmatrix} 1 \\ 0 \end{pmatrix}, \begin{pmatrix} 0 \\ 1 \end{pmatrix}, \begin{pmatrix} -1 \\ 0 \end{pmatrix}, \begin{pmatrix} 0 \\ -1 \end{pmatrix} \right),$$

using the notation that  $[u_1, u_2, \dots, u_r]_i$  is the  $i$ -th point from the set  $[u_1, u_2, \dots, u_r]$ . For more information on the numerical integration details, see [3, 4].

In summary, the algorithm for the cubature Kalman filter (assuming additive noise) proceeds as follows,

*Initialize:* for  $t = 0$

$$\hat{x}_0 = E[x_0]$$

$$P_0 = E[(x_0 - E[x_0])(x_0 - E[x_0])^T]$$

*algorithm:* for  $t = 1, 2, 3, \dots$

Calculate Matrix Square Root

$$P_{t-1|t-1} = S_{t-1|t-1} S_{t-1|t-1}^T$$

Evaluate Cubature Points: for  $i = 1, 2, \dots, 2n_x$

$$X_{i,t-1|t-1} = S_{t-1|t-1} \xi_i + \hat{x}_{t-1|t-1}$$

time-update equations

$$X_{i,t|t-1}^* = f(X_{i,t-1|t-1}, u_{t-1}, \theta)$$

where  $u_{t-1}$  is an exogenous input and  $\theta$  are parameters

$$\hat{x}_{t|t-1} = \frac{1}{2n_x} \sum_{i=1}^{2n_x} X_{i,t|t-1}^*$$

$$P_{t|t-1} = \frac{1}{2n_x} \sum_{i=1}^{2n_x} X_{i,t|t-1}^* X_{i,t|t-1}^{*T} - \hat{x}_{t|t-1} \hat{x}_{t|t-1}^T + Q_{t-1}$$

time-update equations for observation: calculate matrix square root

$$P_{t|t-1} = S_{t|t-1} S_{t|t-1}^T$$

Evaluate Cubature Points: for  $i = 1, 2, \dots, 2n_x$

$$X_{i,t|t-1} = S_{t|t-1} \xi_i + \hat{x}_{t|t-1}$$

$$Y_{i,t|t-1} = h(X_{i,t|t-1}, u_{t-1}, \theta)$$

measurement-update equations

$$\hat{y}_{t|t-1} = \frac{1}{2n_x} \sum_{i=1}^{2n_x} Y_{i,t|t-1}$$

$$P_{yy,t|t-1} = \frac{1}{2n_x} \sum_{i=1}^{2n_x} Y_{i,t|t-1} Y_{i,t|t-1}^T - \hat{y}_{t|t-1} \hat{y}_{t|t-1}^T + R_t$$

$$P_{xy,t|t-1} = \frac{1}{2n_x} \sum_{i=1}^{2n_x} \omega_i X_{i,t|t-1} Y_{i,t|t-1}^T - \hat{x}_{t|t-1} \hat{y}_{t|t-1}^T$$

$$K_t = P_{xy,t|t-1} P_{yy,t|t-1}^{-1}$$

$$\hat{x}_{t|t} = \hat{x}_{t|t-1} + K_t (y_t - \hat{y}_{t|t-1})$$

$$P_{t|t} = P_{t|t-1} - K_t P_{yy,t|t-1} K_t^T$$

where  $Q_{t-1}$  is the process noise covariance and  $R_t$  is the measurement noise covariance.

It should be noted that a distinct advantage of the cubature Kalman filter over the EKF is that it does not require the calculation of derivatives. Other advantages include the lack of tuning parameters, which have been known to have a distinct impact on the effectiveness of convergence on the UKF, and  $2n$  points to propagate as opposed to  $2n + 1$ . The disadvantage of the cubature Kalman filter is the strict enforcement of the Gaussian distributions for the states and observations. Again, similar to the unscented Kalman filter, there are multiple variations of this algorithm for numerical purposes, including a square root implementation. For details on this, we refer the interested reader to [3].

## 2.4 Sampling Based Kalman Filtrals

### 2.4.1 Ensemble Kalman Filter

The main idea of the ensemble Kalman filter (EnKF) is to approximate the error statistics of the estimate by a set of particles sampled from the distribution. Using the work of Majda and Harlim [19], the EnKF is derived accordingly. Unlike the deterministic methods, the prior and posterior error covariances are calculated by the ensemble covariance matrices around the corresponding ensemble mean, instead of the classical covariance equations given in the linear Kalman filter. That is, the covariance is computed

$$P_{x_{i+1}|i} = \frac{1}{N-1} U_{i+1|i} U_{i+1|i}^T \quad (2.51)$$

$$P_{x_{i+1}|i+1} = \frac{1}{N-1} U_{i+1|i+1} U_{i+1|i+1}^T, \quad (2.52)$$

where

$$U_{i+1|i} = [x_{i+1|i}^1 - \hat{x}_{i+1|i}; x_{i+1|i}^2 - \hat{x}_{i+1|i}; \dots; x_{i+1|i}^N - \hat{x}_{i+1|i}] \quad (2.53)$$

$$U_{i+1|i+1} = [x_{i+1|i+1}^1 - \hat{x}_{i+1|i+1}; x_{i+1|i+1}^2 - \hat{x}_{i+1|i+1}; \dots; x_{i+1|i+1}^N - \hat{x}_{i+1|i+1}], \quad (2.54)$$

with  $x_{i+1|i}^j$  being the  $j^{th}$  particle being propagated through the model, and  $x_{i+1|i+1}^j$  is the update of each particle. With this,  $N$  is defined to be the number of particles in which to approximate the distribution and  $\hat{x} = N^{-1} \sum_{j=1}^N x^j$ . From now on,  $U$  shall be defined as the ensemble perturbation matrix as it gives the deviation of each particle from the mean. The advantage of this methodology is that unlike the deterministic methods, there is no need to do an expensive calculation, such as the linearization or statistical transform, to get error statistics. In place of these, each ensemble member is integrated in time through the dynamical model.

To obtain the update equations, the Kalman gain is first calculated, as before. Substituting the en-

semble error covariance results in

$$\begin{aligned}
K_{i+1} &= P_{x_{i+1}|i} H^T (H P_{x_{i+1}|i} H^T + R)^{-1} \\
&= (N-1)^{-1} U U^T H^T (H (N-1)^{-1} U U^T H^T + R)^{-1} \\
&= (N-1)^{-1} U (H U)^T ((N-1)^{-1} (H U) (H U)^T + R)^{-1}.
\end{aligned}$$

In the above expression, and also for the remainder of this chapter, the subscript on  $U$  is omitted for simplicity.

Looking at the Kalman gain equation, it is seen that anywhere the linear operator  $H$  appears, it is coupled to the ensemble perturbation matrix;  $U$ . Due to this consequence, given a nonlinear observation function  $h$ ,  $HU$  can be replaced with the following approximation

$$V = [h(x_{i+1}^1) - \hat{y}_{i+1}; h(x_{i+1}^2) - \hat{y}_{i+1}; \dots; h(x_{i+1}^N) - \hat{y}_{i+1}],$$

where  $\hat{y}_{i+1}$  is the mean of the observation function given each sample,  $\hat{y}_{i+1} = \sum_{j=1}^N h(x_{i+1}^j)$ .

Again, the need for costly calculations can be avoided by using the ensemble approximations in place of deterministic methods.

To get final estimates, the classical Kalman filter update equations are applied to each ensemble member

$$x_{i+1|i+1}^j = x_{i+1|i}^j + K_{i+1}(y_{i+1}^m - h(x_{i+1|i}^j)), \quad (2.55)$$

where  $K_{i+1}$  is defined as above, and the observation,  $y_{i+1}$ , is perturbed accordingly

$$y_{i+1}^m = y_{i+1} + \psi_{i+1}^m, \quad (2.56)$$

where  $\psi_{i+1}^m$  is a Gaussian random variable with mean zero and covariance  $R$ . This perturbation is a Monte Carlo method applied to the Kalman filter formula which yields an asymptotically correct analysis error covariance estimate for large ensemble sizes [19]. In practice, to keep these perturbations unbiased, these random perturbations are generated by first randomly drawing a  $M \times N$  size matrix,  $A$ , where  $N$  is the number of particles and  $M$  is dimension of the data, and take the singular value decomposition of  $(N-1)^{-1} A A^T = F \Sigma F^T$ . Therefore, unbiased random vectors of  $y_{i+1}^m$  are obtained, which is just the column vectors of the matrix  $T = ((N-1)R)^{\frac{1}{2}} F \Sigma^{-\frac{1}{2}} F^T A$  [19]. Since the measurements are being perturbed, the measurement error covariance matrix can be defined to be

$$R = (N-1)^{-1} E E^T,$$

where  $E = [\psi_1, \psi_2, \dots, \psi_N]$  are the ensemble measurement perturbations, with mean zero. In summary, the algorithm for the ensemble Kalman filter is given as follows. An alternate implementation is given



by Evensen [10], and many other implementations also exist.

*Initialize:* for  $i = 0$

$$\hat{x}_0 = E[x_0]$$

$$P_0 = E[(x_0 - E[x_0])(x_0 - E[x_0])^T]$$

*algorithm:* for  $i = 1, 2, 3, \dots$

State Estimation

Sample  $N$  particles from initial distribution: for  $j = 1, \dots, N$

$$x_i^{-j} = f(i-1, x_{i-1}^j)$$

$$\hat{x}_i^- = (N)^{-1} \sum_{j=1}^N x_i^{-j}$$

Covariance Estimation

$$U = [x_i^{-1} - \hat{x}_i^-; x_i^{-2} - \hat{x}_i^-; \dots; x_i^{-N} - \hat{x}_i^-]$$

$$P_i^- = (N-1)^{-1} U U^T$$

Measurement Ensemble

$$y_i^j = y_i + \psi_i^j$$

$$Y = [y_i^1, y_i^2, \dots, y_i^N]$$

$$E = [\psi_i^1, \psi_i^2, \dots, \psi_i^N]$$

$$R = (N-1)^{-1} E E^T$$

$$V = [h(i, x_i^{-1}) - \hat{y}_i; h(i, x_i^{-2}) - \hat{y}_i; \dots; h(i, x_i^{-N}) - \hat{y}_i]$$

unbiased random vectors

$$[F, \Sigma] = \text{svd}((N-1)^{-1} E E^T)$$

$$T = ((N-1)R)^{\frac{1}{2}} F \Sigma^{-\frac{1}{2}} F^T E$$

Kalman Gain Matrix

$$K_i = (N-1)^{-1} U V^T ((N-1)^{-1} V V^T + R)^{-1}$$

State Estimation Update

$$Innov = T - Y$$

$$x_i^j = x_i^{-j} + K_i * Innov$$

Posterior Covariance Update

$$W = [x_i^1 - \hat{x}_i; x_i^2 - \hat{x}_i; \dots; x_i^N - \hat{x}_i]$$

$$P_t = (N-1)^{-1} W W^T$$

### 2.4.2 Ensemble Transform Kalman Filter

Just like the EnKF, the ensemble transform Kalman filter (ETKF) relies on sampling from the proposed normal distribution to obtain the error statistics. The main idea of the ETKF is to take the square root of the covariance matrix, and transform it to a space where it is more robust and well-conditioned [12, 13, 9, 19, 30].

There are multiple methods for taking the square root, the one we shall focus on from here is the ETKF as derived by Bishop [1]. The basic idea is to find a transformation matrix  $T$ ; so that

$$U_{i+1|i+1}U_{i+1|i}^T = UT \quad \text{and} \quad UT(UT)^T = (N-1)^{-1}P_{x_{i+1|i+1}},$$

where  $P_{x_{i+1|i+1}}$  is the sample posterior covariance matrix as previously defined. The posterior ensemble is then generated by taking the posterior mean and adding each column vector from  $U$ . Using the identity

$$A^T(AA^T + R)^{-1} = (I + A^T(R^{-1})A)^{-1}A^TR^{-1}, \quad (2.57)$$

and letting  $V = A$  and  $R$  be the measurement error covariance, The Kalman gain becomes

$$K_{i+1} = (N-1)^{-1}U(I + (N-1)^{-1}V^TR^{-1}V)^{-1}V^TR^{-1}. \quad (2.58)$$

Substituting (2.58) and (2.51) into the posterior covariance formula leads to

$$P_{x_{i+1|i+1}} = (I - \frac{U}{N-1}(I + (N-1)^{-1}V^TR^{-1}V)^{-1}V^TR^{-1}H)\frac{UU^T}{N-1}. \quad (2.59)$$

Factoring out  $\frac{U}{N-1}$  from (2.59) yields

$$P_{x_{i+1|i+1}} = \frac{U}{N-1}(I - (I + \frac{V^TR^{-1}V}{N-1})^{-1}\frac{V^TR^{-1}V}{N-1})U^T. \quad (2.60)$$

Resulting in

$$P_{x_{i+1|i+1}} = \frac{1}{N-1}U(I - (I + B)^{-1}B)U^T, \quad (2.61)$$

where  $B = \frac{V^TR^{-1}V}{N-1}$ . Knowing that  $I - (I + B)^{-1}B = (I + B)^{-1}$  leads to

$$P_{x_{i+1|i+1}} = U((N-1)I + V^TR^{-1}V)^{-1}U^T = U\Sigma U^T = U\frac{TT^T}{N-1}U^T. \quad (2.62)$$

Utilizing this, the ETKF algorithm is obtained.

*Initialize:* for  $i = 0$

$$\hat{x}_0 = E[x_0]$$

$$P_0 = E[(x_0 - E[x_0])(x_0 - E[x_0])^T]$$

*algorithm:* for  $i = 1, 2, 3, \dots$

State Estimation

Sample  $N$  particles from initial distribution: for  $j = 1, \dots, N$

$$x_i^{-j} = f(i-1, x_{i-1}^j)$$

$$\hat{x}_i^- = (N)^{-1} \sum_{j=1}^N x_i^{-j}$$

Covariance Estimation

$$U = [x_i^{-1} - \hat{x}_i^-; x_i^{-2} - \hat{x}_i^-; \dots; x_i^{-N} - \hat{x}_i^-]$$

$$P_i^- = (N-1)^{-1} U U^T$$

Measurement Ensemble

$$y_i^j = y_i + \psi_i^j$$

$$Y = [y_i^1, y_i^2, \dots, y_i^N]$$

$$E = [\psi_i^1, \psi_i^2, \dots, \psi_i^N]$$

$$R = (N-1)^{-1} E E^T$$

$$V = [h(i, x_i^{-1}) - \hat{y}_i; h(i, x_i^{-2}) - \hat{y}_i; \dots; h(i, x_i^{-N}) - \hat{y}_i]$$

SVD of (2.62)

$$[X, \Gamma] = \text{svd}((N-1)I + V^T R^{-1} V)$$

Kalman Gain Matrix

$$K_i = U(X\Gamma^{-1}X^T)V^T R^{-1}$$

State Estimation Update

$$\hat{x}_i = \hat{x}_i^- + K_i(y_i - h(\hat{x}_i^-))$$

Transformation Matrix

$$T = \sqrt{N-1} X \Gamma^{-\frac{1}{2}} X^T$$

$$W = U T$$

Posterior Ensemble and Covariance

$$A = \hat{x}_i + W$$

$$P_i = (N-1)^{-1} A A^T$$

## 2.5 Problem Statement

Consider a state space model of the form

$$x_{i+1} = f(i, x_i, u_i, \theta) + w_i \quad (2.63)$$

$$y_{i+1} = h(i + 1, x_{i+1}, u_i, \theta) + v_{i+1}, \quad (2.64)$$

where  $f$  is a nonlinear function of the state  $x_{i+1} \in \mathcal{R}^{n_x}$ , and  $h$  is a nonlinear function relating the observation  $y_{i+1} \in \mathcal{R}^{n_y}$  to the state. The variable  $u_i \in \mathcal{R}^{n_u}$  is an exogenous control,  $w_i$  and  $v_{i+1}$  are i.i.d. noise processes, and  $\theta$  denote the model parameters.

The objective is to find optimal parameter estimates allowing the best fit to the data. Classically, parameter estimation is done by using an optimization technique to minimize a cost function [29]. Often, the cost function is defined as the sum of the squares of the difference between the model output,  $y_k$ , and observations,  $y_k^{obs}$ , given by

$$J(\theta) = \sum_{k=1}^N \gamma_k [y_k^{obs} - y_k]^2, \quad (2.65)$$

where  $\gamma_k$  is a weighting parameter and  $y_k^{obs} - y_k$  is the residual. This approach is commonly referred to as nonlinear least squares.

While few papers are explicitly concerned with the use of filtering techniques for parameter estimation [14], there are multiple methods which can achieve this goal. The filters previously defined were for state estimation, the optimal combination of the model predictions and observations to obtain an improved estimate of the state of the system; however, utilizing the following methodologies allows the filters to subsequently estimate parameters. The first, and most direct, is to modify the state space representation to accommodate this objective. Since the observations are assumed to be coming from the model, and optimal parameter estimates are the main focus, one method can be obtained by assuming that the parameters have zero dynamics

$$\begin{aligned} \theta_{i+1} &= \theta_i + r_i \\ y_{i+1} &= h(i + 1, x_{i+1}, u_{i+1}, \theta_{i+1}) + v_{i+1}, \end{aligned}$$

where  $r_i$  and  $v_{i+1}$  are i.i.d. noise processes. However, the goal is to not only estimate the parameters, but also to fit the states as accurately as possible. This methodology is known as dual estimation [14]. There are two methodologies to be discussed that directly achieve this. The first of these methods is joint estimation [9, 10, 14, 22, 24, 30]. Joint estimation is done by concatenating the parameters into the

state-space. This gives the following

$$\begin{aligned} z &= [x; \theta] \\ z_{i+1} &= f(i, z_i, u_i) + w_i \\ \theta_{i+1} &= \theta_i + r_i. \end{aligned}$$

A second approach is called the dual filter [22, 23, 24, 31, 32]. Dual estimation is done by concurrently running a state filter and parameter filter in parallel [14, 22, 23]. The state filter estimates the state;  $x_i$ ; using the parameter value from the parameter filter at time  $i - 1$ . While, the parameter filter estimates the parameter,  $\theta_i$ , using the state estimate at time  $i - 1$ . These both propagate forward in time and obtain estimates at each time step. Specifically, the state filter estimates the posterior of the state;  $p(x_{i|i-1}|y_i, \hat{\theta}_{i-1})$ ; given the posterior estimate of the parameter at the previous time point;  $\hat{\theta}_{i-1}$ , while the parameter filter estimates the posterior of the parameter,  $p(\theta_{i|i-1}|\hat{x}_{i-1}, y_i)$ ; given the posterior estimate of the state at the previous time point;  $\hat{x}_{i-1}$ .

## 2.6 Applications

In this section, we will compare the performance of the filtering methodologies presented in the previous sections on several test problems. Their performance will be judged based upon their ability to fit the states, and more importantly, the model parameters accurately given varying levels of state measurements. As stated previously, we will only compare the dual filters and joint filter estimation methods, and not the parameter filters. All computations were done using code written in MATLAB.

These methods will be tested using three examples, the Lorenz equations, an HIV model, and a model predicting cerebral auto-regulation. The first two examples were constructed using simulated data, while the last example uses real patient data. Therefore, for the first two examples, the model is known to be correct, while for the last example, the model is only an approximation of the system. Each example was chosen to present a different challenge. The Lorenz example was selected to test the performance for a highly nonlinear, chaotic system with a temporal shift in parameter values both full and partial state observations. The HIV model was selected to test the performance for a nonlinear model with numerical stiffness, sparse measurements, and multiplicative errors. Lastly, the model predicting cerebral auto-regulation was selected as a real world example utilizing real patient data.

### 2.6.1 Lorenz Equations

The first example is the famous Lorenz 63 equations first studied by Lorenz in 1963 [20]. The system is made up of 3 state equations and 3 model parameters, with nonlinearities present in 2 of the 3 equations. This was chosen because of the well known properties of the chaotic behavior and strong nonlinearities.

Due to the nature of the system, small perturbations to the state can lead to large qualitative changes. This system of ordinary differential equations is given by

$$\begin{aligned}\frac{dx}{dt} &= \sigma(y - x) \\ \frac{dy}{dt} &= x(\rho - z) - y \\ \frac{dz}{dt} &= xy - \beta z.\end{aligned}$$

For this test case, we generate data using the following initial conditions and parameter values with a parameter regime change occurring at time;  $t = 10$ .

$$\begin{pmatrix} x_0 \\ y_0 \\ z_0 \end{pmatrix} = \begin{pmatrix} 0.9 \\ 1 \\ 1.1 \end{pmatrix}, \quad \begin{pmatrix} \sigma \\ \rho \\ \beta \end{pmatrix} = \begin{pmatrix} 10; 7 \\ 28; 21 \\ \frac{8}{3}; 1 \end{pmatrix}, \quad w_k = 0.1, \quad \Delta t = 0.01.$$

This was done to test each algorithm's ability to accurately track the parameters and states when perturbations to the systems dynamics occur. For each case, we start with the initial condition given from above, but with initial parameter values perturbed away from the true solution. The initial parameter values and covariances are

$$\begin{pmatrix} \sigma_0 \\ \rho_0 \\ \beta_0 \end{pmatrix} = \begin{pmatrix} 5 \\ 21 \\ \frac{1}{3} \end{pmatrix}, \quad Q = \begin{pmatrix} 0.001 & 0 & 0 \\ 0 & 0.001 & 0 \\ 0 & 0 & 0.001 \end{pmatrix}, \quad R = \begin{pmatrix} 0.1 & 0 & 0 \\ 0 & 0.1 & 0 \\ 0 & 0 & 0.1 \end{pmatrix}, \quad Q_{\sigma, \rho, \beta} = \begin{pmatrix} 0.5 & 0 & 0 \\ 0 & 0.5 & 0 \\ 0 & 0 & 0.5 \end{pmatrix}.$$

Since the data is simulated, the observation and process noise covariance ( $Q$  and  $R$ , respectively) are known. They are appropriately defined to reflect that knowledge. However, as we are more interested in the application of filtering for parameter estimation, we perturb the initial values of the parameters away from the truth, defined above, and set the parameter process noise covariance,  $Q_{\sigma, \rho, \beta}$ , to appropriately reflect this condition, and to account for the temporal shift in parameter regime. For this example, one hundred runs of each filter with full state observations were performed, perturbing the initial state and parameter values with Gaussian noise distributed  $N(0, 0.1)$ , and the mean run results are presented. To appropriately encapsulate this, the initial covariances were set as follows:

$$P_{x_0} = P_{q_0} = \begin{pmatrix} 0.1 & 0 & 0 \\ 0 & 0.1 & 0 \\ 0 & 0 & 0.1 \end{pmatrix}.$$

Reviewing Figure 2.1, the deterministic methods tracked the state over the whole simulation. It is noted that the results for both the joint and dual UKF and CKF are nearly identical, and therefore differen-

tiation between the UKF and CKF methods on the plots is negligible without much finer granularity. More importantly, the accuracy of the methods' abilities to track the parameters through time, and the parameter regime change, is shown in Figures 2.2 and 2.3. The dual filters' mean parameter estimates are presented in Figure 2.2, with 3 standard deviations plotted around each estimate, and the true parameter value plotted as the solid lines. As before, the difference between the CKF and UKF is negligible, and both track the parameter with the same qualitative features. As can be seen, both dual estimation methods track the parameter values, with a small lag when the regime shift occurs, but quickly adapt and shift to the correct value. From Figure 2.3, the joint estimation methods exhibit more variation for the mean estimates due to erratic changes occurring frequently to the estimates. This is due to the nature of the joint estimation technique. As we are appending the parameters as unobserved states, the method is partitioning the error equally among the states and the parameters, and can pass it back and forth. This translates into the filter moving the state to best fit the data at the cost of the parameter shifting greatly. As the parameter shifts drastically, the state is once again inaccurate and requires another sharp change in the parameter to accommodate. This overcorrection leads to the observed qualitative behavior as the error gets propagated back and forth between the state and parameter. Because the dual filter compartmentalizes the error for the state and parameter into two distinct filters running concurrently, this behavior is not as noticeable. However, since the state filter is using estimates from the parameter filter, and vice versa, to update, the dual filter can also exhibit variation as the error of each filter is still passed, but better handled due to each filter's updated covariance and relegation of error to their respective components. Table 2.1 presents the mean results over the hundred runs for the sum of square truth (SST), the difference between the filters state estimate and the known true solution, the sum of square parameter (SSP), the difference between the true parameter value and the estimated parameter value at final time, each parameter estimate with one standard deviation, and the amount of CPU time each filter took.

Table 2.1: Results for deterministic filters with full state observations over parameter regime shift; joint and dual, averaged over 100 runs.

	truth	j. ukf	j. ckf	j. ekf	d. ukf	d. ckf
SST	0	3.03	3.03	1.14	1.00	0.72
SSP	0	0.12	0.12	0.86	0.031	0.031
$\sigma$ (1 std)	10; 7	7.22 (3.04)	7.22 ( 3.27)	6.91 (0.91)	6.93 (1.02)	6.93 (1.02)
$\rho$ (1 std)	28; 21	21.23 (2.86)	21.23 ( 3.14)	20.63 (0.81)	20.83 (0.47)	20.83 (0.47)
$\beta$ (1 std)	$\frac{8}{3}; 1$	0.87 (0.94)	0.87 (1.14)	0.84 (0.37)	1.01 (0.10)	1.01 (0.10)
CPU (secs)	N/A	5.41	3.54	100.61	7.96	4.78

Next, the ensemble filters are presented for a single run. Figure 2.4 shows the ensemble filters' ability

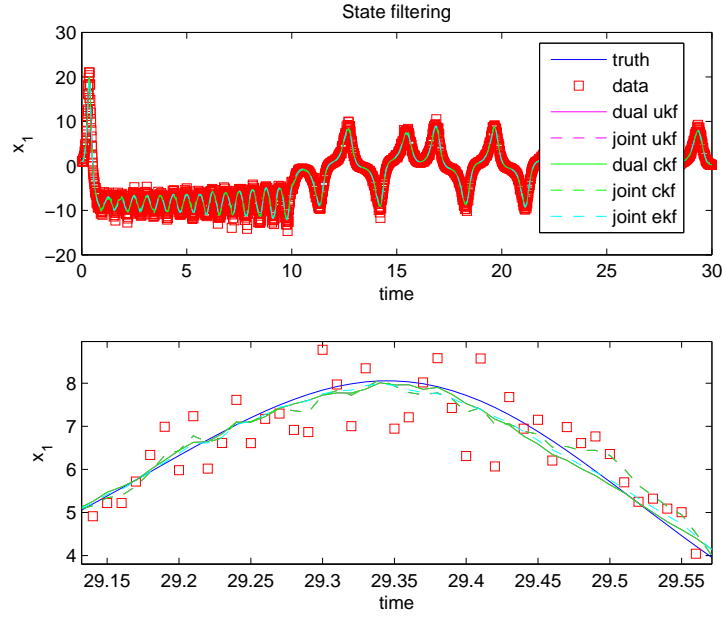


Figure 2.1: Top: Plot of filter estimates for  $x_1$  utilizing both joint and dual filters over all observations. Bottom: Plot of filter estimates for  $x_1$  utilizing both joint and dual filters over short time scale. This gives a better perspective of the methods tracking ability.

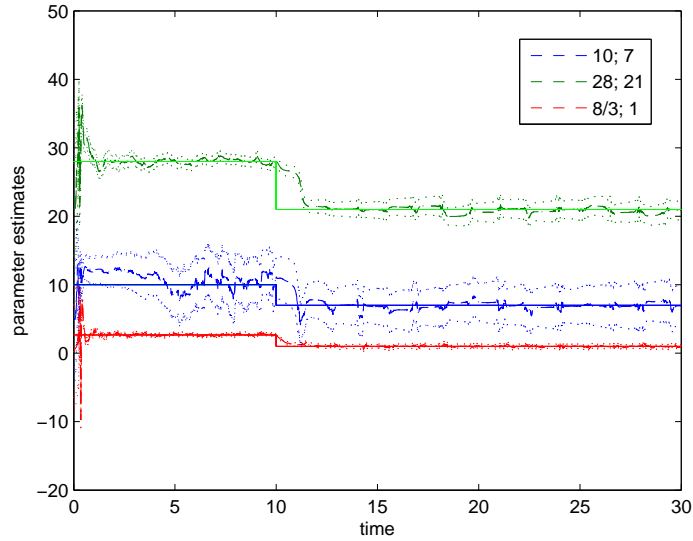


Figure 2.2: Plot of Parameter estimates for the dual UKF and dual CKF along with 3 standard deviations (dotted) over the all observations, as well as true parameter values; green:  $\rho$  blue:  $\sigma$ . red:  $\beta$



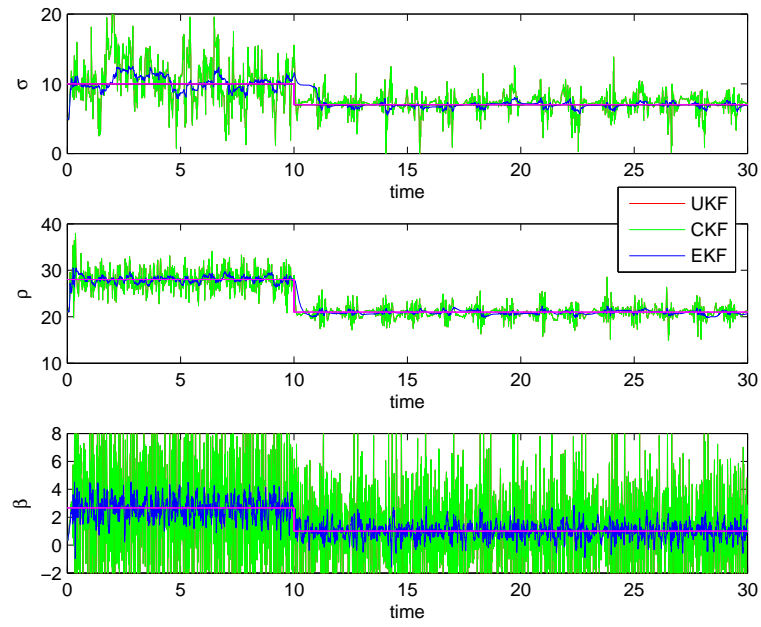


Figure 2.3: Plot of parameter estimates for the joint EKF, joint UKF and joint CKF over all observations, as well as true parameter values (purple lines). UKF and CKF obtained nearly identical results and therefore the UKF (red) is not visible.

to track the state;  $x_1$ ; over the parameter shift. The ensemble filters accurately track the state initially, top of Figure 2.4, but fail to catch the parameter regime shift and therefore, fail to track the state after this event, bottom of Figure 2.4. This is more noticeable in Figure 2.5 where the ensemble parameter estimates are shown, with the solid line being the true parameter value. This inability to catch the shift is due to the nature of the sampling technique underlying the method. At each update, the samples are shifted based upon the covariance, which is shrinking due to the increased confidence and accuracy in the estimates. Therefore, when the parameter shift occurs, the ensemble filters struggle to sample from enough of the parameter space to quickly adjust, making the shift occur slowly and ultimately inaccurately. Table 2.2 presents the sum of squares truth, sum of squares for the parameters, and each parameter estimate with standard deviation for the ensemble filters.

An update implemented to account for the ensemble shrinkage noted above is to append a process noise onto the prior. Instead of calculating the prior solely by propagating the particles through the model

$$x_i^{-j} = f(x_{i-1}^j, i-1, u_{i-1}, \theta),$$

a process noise is added to account for a known underlying model error, which prevents the shrinkage phenomena described previously. The prior calculation then becomes

$$x_i^{-j} = f(x_{i-1}^j, i-1, u_{i-1}, \theta) + w_i,$$

where  $w_i \sim N(0, Q)$ . This perturbs the prior ensemble with covariance;  $Q$ ; to maintain a known process error. For the case described above, this process noise will allow the parameters to span the space more readily, accounting for the shift and properly estimating the parameters.

Table 2.2: Results for ensemble filters with full state observations over parameter regime shift averaged over 100 runs.

	truth	EnKF	ETKF
SST	0	203.69	153.96
SSP	0	42.73	82.94
$\sigma$ (1 std)	10; 7	11.06 (0.005)	15.49(7.54e-4)
$\rho$ (1 std)	28; 21	25.77 (0.0045)	23.69 (5.48e-4)
$\beta$ (1 std)	$\frac{8}{3}$ ; 1	2.87 (5.76e-4)	2.88 (5.92e-5)

The new implementation of the ensemble filters is now presented with mean results over one hundred runs. Figure 2.6 shows the updated ensemble filters' ability to track the states;  $x_1$  and  $x_3$ ; over the parameter shift. From Figure 2.6, the updated ensemble filters do well to accurately track the states over the entire interval, including the parameter shift. The parameter estimates for the updated ensemble fil-

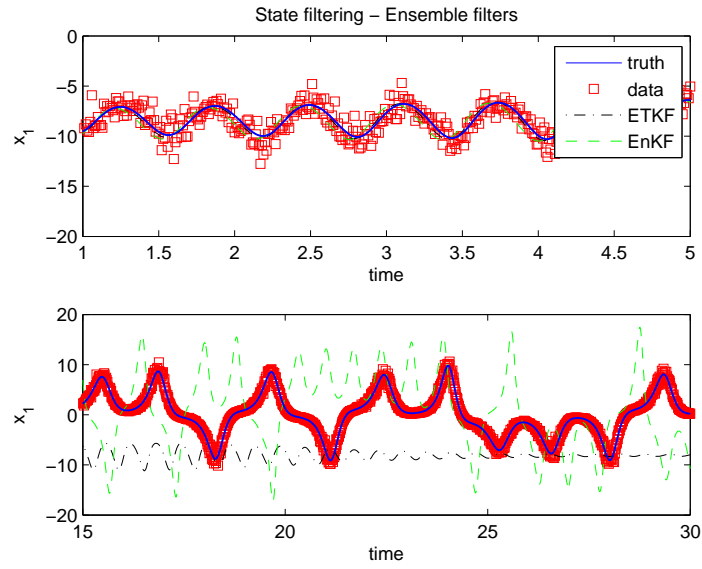


Figure 2.4: Top: Plot of ensemble methods' state filter estimate of  $x_1$  for the Lorenz equations prior to parameter shift. Bottom: Plot of ensemble methods' state filter estimate of  $x_1$  for the Lorenz equations post parameter shift.

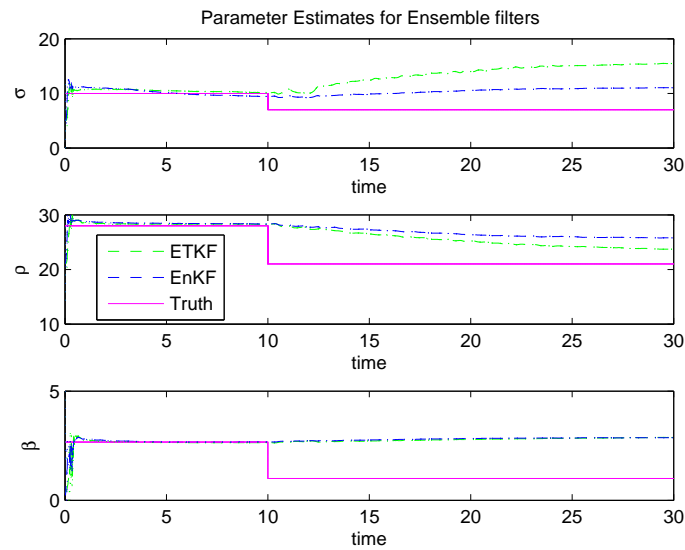


Figure 2.5: Plot of parameter estimates for both ensemble filters over all observations.

ters are presented in Figure 2.7, with the true values plotted as the solid lines. Similar to the deterministic methods, the updated ensemble methods track the parameter estimates accurately over time, including quickly adapting to the parameter shift. However, similar to the joint methods, the updated ensemble methods exhibit a large degree of variation around the mean. Since ensemble methods are based upon random sampling, samples can be drawn that maximize the likelihood for the observed state, but with a large error in the parameter. These deviations in the parameters cause errors in the next update of the state. To account for these errors, the filter corrects the parameters. However, this causes the previous state estimates to be less accurate, which leads to adjustment in the states, and the qualitative features in Figure 2.7. These deviations in the parameters are made worse by the updated sampling due to the random perturbing of the particles with the process noise. This leads to extra deviation in the estimates shown in the parameters compared to the joint and dual methods. One way to account for these deviations would be to decrease the process noise. Table 2.3 presents the mean over the hundred runs for the sum of squares truth, sum of squares for the parameters, each parameter estimate with standard deviation for the updated ensemble filters, and CPU time.

Table 2.3: Results for Updated Ensemble Filters with full state observations averaged over 100 runs

	truth	EnKF	ETKF
SST	0	8.00	3.24
SSP	0	26.3	7.63
$\sigma$ (1 std)	10; 7	6.54 (2.89)	7.74(5.82)
$\rho$ (1 std)	28; 21	21.24 (2.81)	21.32 (5.51)
$\beta$ (1 std)	$\frac{8}{3}$ ; 1	0.15 (1.11)	0.78 (1.21)
CPU (secs)	N/A	45.87	76.11

Next, the parameters values are kept in the chaotic regime for the whole simulation, and only use observations for  $x_1$ . This was done to study the filters' ability to estimate more states than we have observations. This is important as rarely in practice does one obtain full state observations for the system. Doing this over a single execution of each filter, it is seen that the methods seem to deal quite differently with the new situation. From Figure 2.8, all filters do well to track  $x_1$  for which observations are present, however, most of the methods struggle to track  $x_2$ , except for the joint EKF and dual UKF. The bottom plot in Figure 2.8 does not display the dual CKF as it fails to track the state and largely deviates, in orders of magnitude, away from the truth. Figure 2.9 shows the parameter estimates for the methods with observations for  $x_1$  only. Other than the joint EKF, no method seems to show much success in terms of tracking the states or parameters with observations for  $x_1$ . This is likely due to the more complicated procedures each of the filters uses in calculating the covariance; because they not only require the covariance, but also a cross-covariance calculation, to estimate the updated state, errors can be more easily

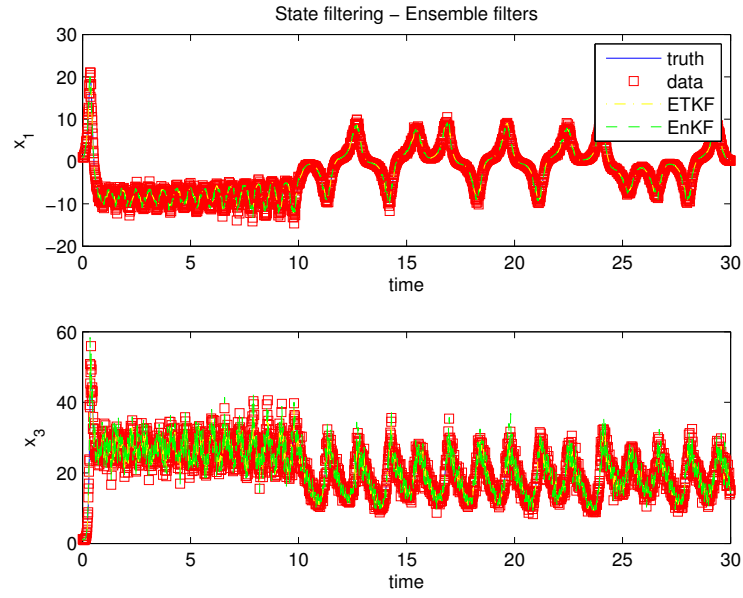


Figure 2.6: Top: Plot of updated ensemble state filter estimates of  $x_1$  for the Lorenz equations over all observations. Bottom: Plot of updated ensemble state filter estimates of  $x_3$  of the Lorenz Equations over all observations.

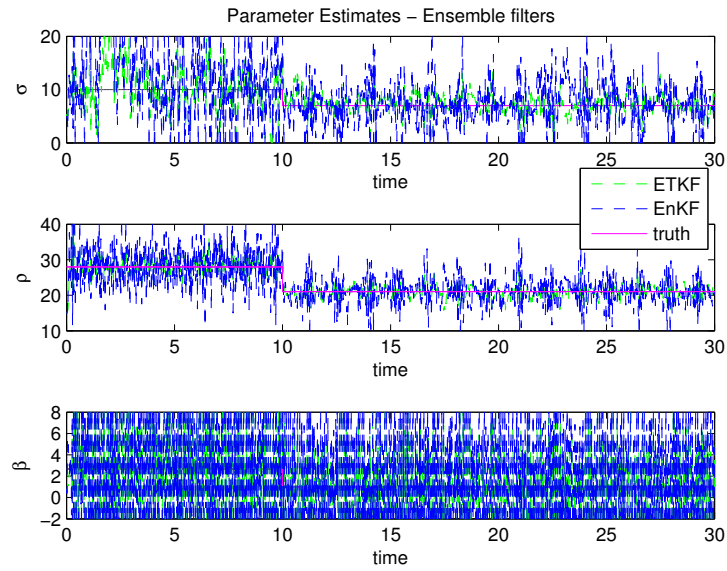


Figure 2.7: Plot of parameter estimates for both updated ensemble filters over all observations along with true parameter values (purple lines).

propagated which leads to less stable results.

Table 2.4: Results for deterministic filters given observations for  $x_1$ .

	truth	j. ukf	j. ckf	j. ekf	d. ukf	d. ckf
SST	0	1.61e4	509.4	6.21	128.48	2.07e9
SSP	0	146.85	26.95	1.45	213.99	343.97
$\sigma$ (1 std)	10	12.61 (4.86)	10.12 ( 32.83)	9.43 (0.7)	7.39 (.17)	0.002 (0.001)
$\rho$ (1 std)	28	17.46 (3.47)	23.59 (47.4)	26.94 (1.2)	42.34 (1.90)	27.25 (111.29)
$\beta$ (1 std)	$\frac{8}{3}$	8.04 (7.03)	5.40 (28.18)	2.65 (0.46)	1.42 (3.14)	18.27 (127.75)

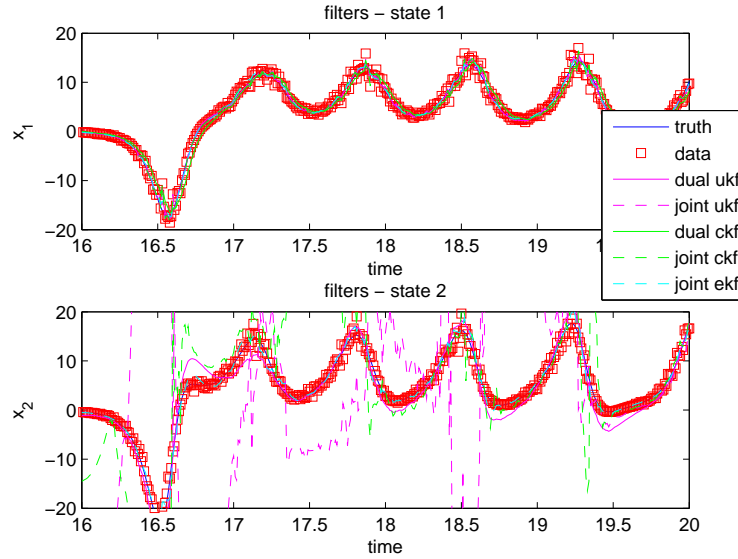


Figure 2.8: Top: Plot of joint and dual state filter estimates for  $x_1$  over short time scale given observations only for  $x_1$ . Bottom: Plot of joint and dual state filter estimates for  $x_2$  over same short time scale given observations only for  $x_1$ .

Moving onto the ensemble methods, Figure 2.10 shows the methods' ability to track both the state with observations;  $x_1$ ; as well as the unobserved states;  $x_3$ . As seen, the ensemble methods have no trouble with the unobserved states, tracking all states accurately over the whole simulation. Reviewing their parameter estimates, Figure 2.11 shows the mean parameter estimate for both ensemble filters and the true parameter value. The ensemble methods quickly adapt their parameter estimates to a neighborhood of the true solution by time,  $t = 5$ . This success by the ensemble methods seems to be due to

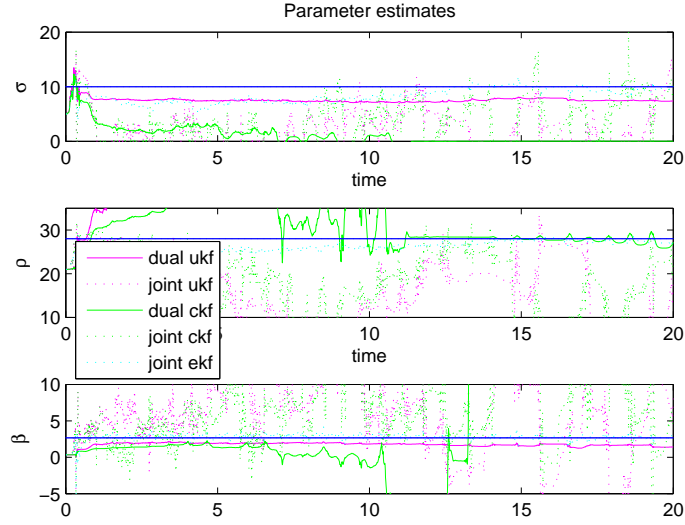


Figure 2.9: Plot of joint and dual filters' parameter estimates given observations only for  $x_1$ .

their underlying theory of sampling. Instead of a deterministic covariance, which can lead to large errors which causes large discrepancies in the estimate, the ensemble methods use a sampling strategy which prevents these errors from propagating into the estimate as easily. This is because though the ensemble might have a few samples with a large variation from the true posterior, these outliers are averaged out by the rest of the ensemble which are more accurately approximating the posterior. The deterministic methods require the covariance to be accurate each step, and one inaccurate step gets propagated forward leading to less and less accurate estimates, as we observed earlier. From Table 2.5, note the accuracy of the ensemble methods for limited state observations, only  $x_1$ .

Table 2.5: Results for ensemble filters given observations for  $x_1$  only

	truth	EnKF	ETKF
SST	0	0.81	0.95
SSP	0	0.27	0.086
$\sigma$ (1 std)	10	10.35 (0.007)	9.87( 0.026)
$\rho$ (1 std)	28	27.62 (0.0038)	27.74 ( 0.019)
$\beta$ (1 std)	$\frac{8}{3}$	2.70 (0.0006)	2.73 (0.00195)

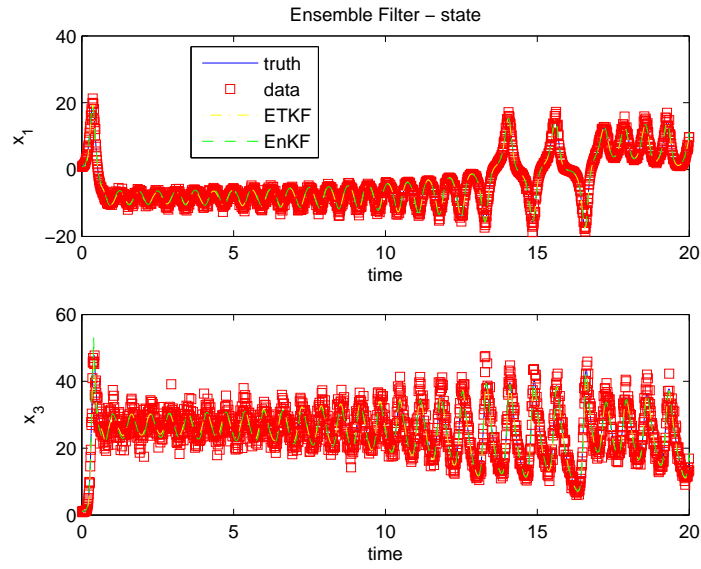


Figure 2.10: Top: Plot of ensemble methods' state filter estimates for  $x_1$  over short time scale given observations only for  $x_1$ . Bottom: Plot of ensemble methods' state filter estimates for  $x_2$  over same short time scale given observations only for  $x_1$ .

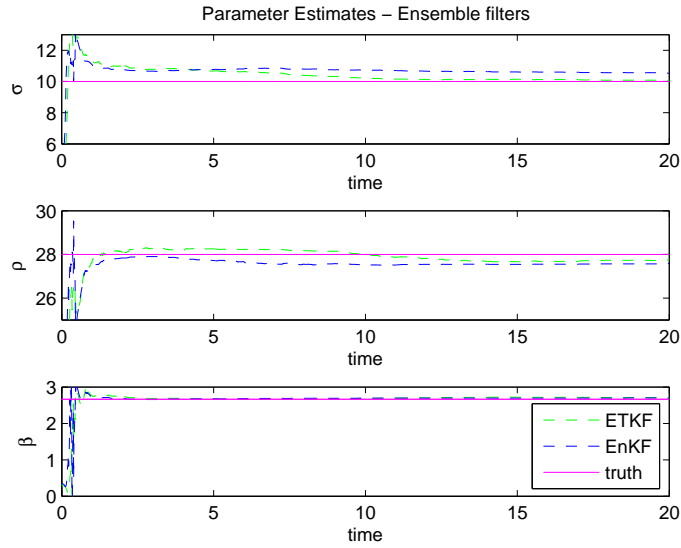


Figure 2.11: Plot of parameter estimates using ensemble filters given observations only for  $x_1$  along with true parameter values (purple lines).



### 2.6.2 HIV model

The second example is a HIV model with quadratic nonlinearities in two of the state equations and six model parameters. HIV is a viral disease that infects healthy T-cells in the body. A simple mathematical model describing the dynamics of HIV in humans is given by [12],

$$\dot{T} = \lambda - dT - kVT \quad (2.66)$$

$$\dot{T}^* = kTV - \delta T^* \quad (2.67)$$

$$\dot{V} = N\delta T^* - cV, \quad (2.68)$$

where  $\lambda$  is the recruitment of uninfected T-cells,  $d$  is the per capita death rate of uninfected cells,  $k$  is the infection rate,  $\delta$  is the death rate of uninfected cells  $T^*$ ,  $N$  is the number of new HIV virons  $V$  per infected cells and  $c$  is the clearance rate. This test case was not only chosen because of the difficulties it provides due to the nonlinearities and its biological background, but more importantly, because of the varying orders of magnitude of the parameters and states. Due to the stiff nature of the system, numerical issues can arise which can cause inaccuracies in the estimates if not appropriately handled by the filter.

To test this model, we create data using the following initial conditions and parameter values,

$$\begin{pmatrix} T_0 \\ T_0^* \\ V_0 \end{pmatrix} = \begin{pmatrix} 1000 \\ 0.0001 \\ 0.001 \end{pmatrix}, \quad \begin{pmatrix} \lambda \\ d \\ k \\ \delta \\ N \\ c \end{pmatrix} = \begin{pmatrix} 10 \\ 0.01 \\ 8e^{-4} \\ 0.7 \\ 100 \\ 13 \end{pmatrix}, \quad w_k = 0.04, \quad \Delta t = 0.5.$$

Unlike the previous example, data is created using a multiplicative error model, with errors given by  $x(1 + \epsilon)$ . This was done as it is often more realistic for biological problems to exhibit multiplicative error in the data as opposed to additive. Also, unlike the previous example, the sampling rate is set to a much larger interval. This is done to test the filters' ability to accurately estimate the parameters over a sparser temporal data set. This is once again important as it is often difficult to obtain dense data sets for biological and biomedical experiments. Using the analysis provided by Fink et al. [12] by calculating the sensitivities and using these to carry out subset selection, only the parameters  $\lambda$ ,  $k$ , and  $\delta$  can be accurately estimated due to identifiability. Similar to the previous example, we start with the initial conditions given, but with the identifiable parameter values perturbed away from the true values, while the unidentifiable parameters are held constant at their known values. To deal with the issues caused by the multiplicative error model and the stiffness, a log transformation is applied to both the model and data. The transformation is defined as  $y_{new} = \log_{10}(y)$ , where  $y$  is the original data, and  $x_{new} = \log_{10}(x)$ , where  $x$  is the original state dynamics. To obtain the new model, we use  $\frac{dx_{new}}{dt} = \frac{1}{\log(10)x} \dot{x}$

and substitute  $10^{x_{new}}$  for  $x$ . The above transformation will scale the errors in the data from multiplicative to additive, fitting the assumptions of the filter, and will also scale the states and parameters so as to prevent numerical errors from the varying orders of magnitude. The initial covariances and parameters are then given by the following, using the log transformed model and data,

$$\begin{pmatrix} \lambda_0 \\ k_0 \\ \delta_0 \end{pmatrix} = \begin{pmatrix} 6 \\ 0.0005 \\ 0.3 \end{pmatrix}, Q = \begin{pmatrix} 0.0001 & 0 & 0 \\ 0 & 0.0001 & 0 \\ 0 & 0 & 0.0001 \end{pmatrix}, R = \begin{pmatrix} 0.02 & 0 & 0 \\ 0 & 0.02 & 0 \\ 0 & 0 & 0.02 \end{pmatrix},$$

$$Q_{\lambda,k,\delta} = \begin{pmatrix} 0.0001 & 0 & 0 \\ 0 & 0.0001 & 0 \\ 0 & 0 & 0.0001 \end{pmatrix}.$$

The observation and process covariances are set appropriately knowing the nature of the simulated data. Similar to the first example, one hundred runs of each filter are conducted by corrupting our intended initial conditions for the states and parameters with Gaussian noise, distributed  $N(0, 0.1)$ . Therefore, the initial covariance for the states and parameters,  $P_{x_0}$  and  $P_{q_0}$ , are set as

$$P_{x_0} = P_{q_0} = \begin{pmatrix} 0.1 & 0 & 0 \\ 0 & 0.1 & 0 \\ 0 & 0 & 0.1 \end{pmatrix}.$$

As the parameterization of the model rarely contributes to the process noise, and can even be negligible, the parameter process noise covariance is set to be very small, or multiple orders of magnitude less than the initial estimate. Figure 2.12, transforming the states and parameters back to the original scaling, we can see that, except for the joint CKF, the filters are all accurately tracking the states qualitatively and quantitatively. Some overshoot on the peaks can be seen by both dual filters and both ensemble filters, but damps out as the state approaches steady state. Figure 2.13 depicts the same overshoot, which can be attributed to the filters convergence to the parameter estimates. Reviewing Figure 2.14, all 3 parameters for both dual filters are taking longer to approach the correct parameter estimate, while for the ETKF,  $k$  is slow to converge to the proper value. This can often be attributed to the model and the sensitivity of the parameters to the data. If the parameters are not sensitive, or sensitive only in selected regions, then the estimates will take longer to converge or won't change much until those regions are evaluated by the filter. For this example, there are far fewer measurements than the previous, which can explain the slower convergence in parameter estimates to the truth.

Comparing the ensemble filters to the deterministic, the EnKF took more iterations to converge to the proper state estimates and had larger error because of this. The ETKF took fewer iterations and this is likely due to the sampling method implemented. Because we are filtering around the log-transformed

Table 2.6: Results for the deterministic filters for the HIV model in  $\log_{10}$  space, averaged over 100 runs

	truth	j. ukf	j. ckf	j. ekf	d. ukf	d. ckf
SST	0	0.0015	0.0015	0.005	17.21	10.88
SSP	0	1.5e-5	1.5e-5	9.2e-6	6.44	5.44
$\lambda$ (1 std)	1	1.002 (0.24)	1.002 (0.07)	1.001 (0.048)	0.98 (0.2)	0.97 (0.2)
$k$ (1 std)	-3.097	-3.1 (0.16)	-3.1 (0.04)	-3.1 (0.033)	-2.85 (0.03)	-2.9 (0.03)
$\delta$ (1 std)	-0.1549	-0.155 (0.16)	-0.155 (0.04)	-0.156 (0.01)	-0.127 (0.01)	-0.138 (0.01)
CPU (secs)	N/A	40.03	39.11	13.53	46.9	41.37

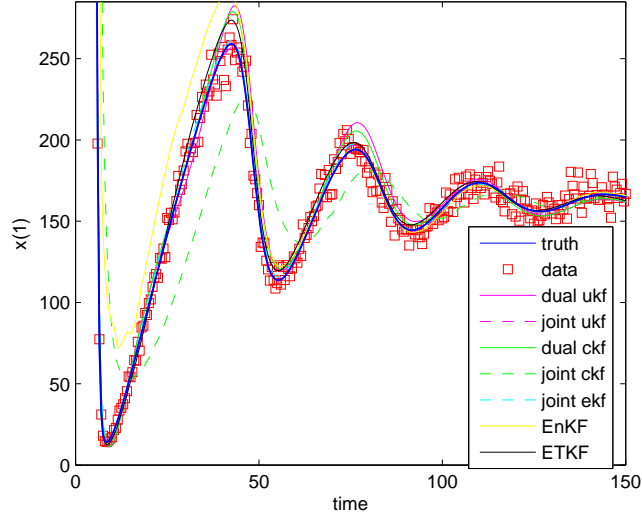


Figure 2.12: Plot of filter estimates for the number of uninfected T cells,  $T^*$ , over all the measurements.

model and data, small errors in log space equate to large deviations in the original space. The ETKF handled this better by using the SVD to ensure more accurate distributions. As the small errors accumulated in the EnKF sampling, the EnKF required more iterations to accurately converge to the correct estimates. However, the EnKF estimates  $\lambda$  more accurately than the ETKF. For our tests, we are using 100 particles to approximate the distribution. Enlarging the number of particles could improve the robustness of the estimates, but at the cost of computational time. Since each particle results in a function evaluation, the computation time increases linearly with the number of particles. Since the deterministic filters all propagate the covariance through a deterministic algorithm, they do not encounter this sampling error. However, because they are solely based upon their deterministic methodology for estimating the covariance, if an error is encountered, the repercussions are directly felt in the estimate and usually results in inaccuracies and divergence. The ensemble methods, though they incorporate a sampling error, do use averaging to correct for these poor estimates and are therefore far more robust to errors in the covariance over the course of a run. Reviewing Tables 2.6 and 2.7, the accuracy for both EnKF and ETKF methods can be seen for this case.

Table 2.7: Results for the Ensemble Filters for the HIV model in  $\log_{10}$  space, averaged over 100 runs

	truth	EnKF	ETKF
SST	0	0.07	0.002
SSP	0	0.04	0.05
$\lambda$ (1 std)	1	0.99 (0.19)	0.96 (0.36)
$k$ (1 std)	-3.097	-3.099 (0.10)	-3.1 (0.06)
$\delta$ (1 std)	-0.1549	-0.157 (0.11)	-0.153 (0.07)
CPU (secs)	N/A	359.3	364.2

### 2.6.3 Autoregulation model

The final example is a model used to describe cerebral autoregulation coupled with intercranial hemodynamics, and shall also incorporate real data as a final test of practicality. Many models have been developed for this purpose, but Ursino and Lodi's [28] (U-L) model is selected as it is simple, but still retains the important features to describe the cerebral blood flow. The goal is to estimate the blood flow velocity in response to changes in arterial blood pressure. A more detailed analysis and derivation is given by Aoi [2]. Viewing arterial pressure as a function of time,  $p_a = p_a(t)$ , and using the diagram of

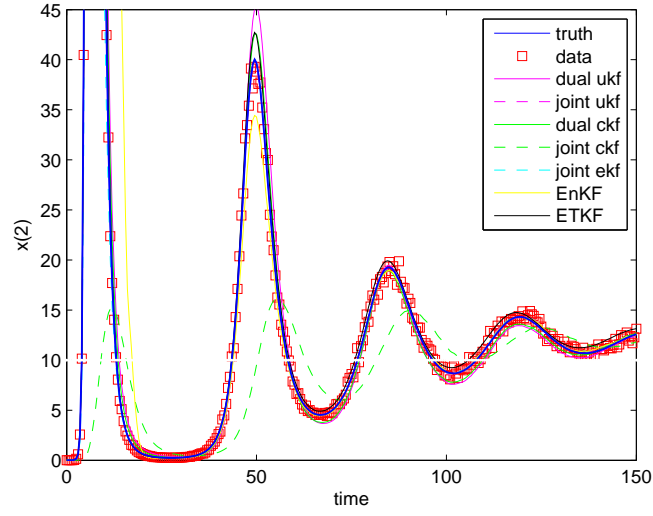


Figure 2.13: Plot of filter estimates for the number of infected T cells

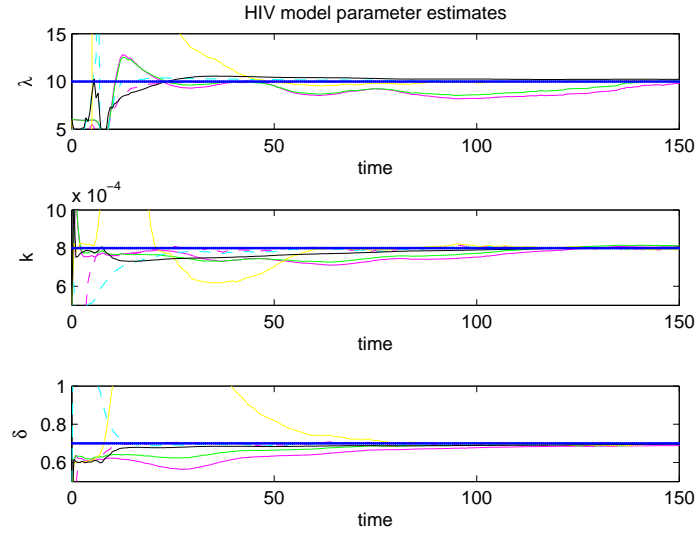


Figure 2.14: Plot of parameter estimates for  $\lambda$ ,  $k$  and  $\delta$  for all the filters; blue dashed line is the true value, solid magenta line is the dual ukf, dashed magenta is the joint ukf, solid green line is the dual ckf, dashed green is the joint ckf, solid cyan line is the joint ekf, solid yellow is the EnKF, and solid black is the ETKF

cerebral dynamics (Figure 2.15) to construct a circuit analogy, the U-L model is given by

$$\begin{aligned}\frac{dp_{ic}}{dt} &= \frac{k_E p_{ic}}{1 + C_a k_E p_{ic}} \left[ C_a \frac{dp_a}{dt} + \frac{dC_a}{dt} (p_a - p_{ic}) + \frac{p_c - p_{ic}}{R_f} - \frac{p_{ic} - p_{vs}}{R_0} \right] \\ \frac{dC_a}{dt} &= \frac{1}{\tau} [-C_a + \sigma(x)],\end{aligned}$$

with observation function

$$v(t_i) = \frac{1}{A_c R_{pv}} \left[ \frac{(p_a - p_{ic})^3}{p_a^2 - 2p_a p_{ic} + p_{ic} + \frac{k_R}{C_a^2 R_{pv}}} \right],$$

where

$$\begin{aligned}\sigma(Gx) &= \frac{(C_{an} + \Delta C_a/2) + (C_{an} - \Delta C_a/2)e^{Gx/k_\sigma}}{1 + e^{Gx/k_\sigma}} \\ R_a &= \frac{k_R}{V_a^2}, \quad V_a = C_a(p_a - p_{ic}) \\ p_c &= \frac{p_a R_{pv} + p_{ic} R_a}{R_{pv} + R_a},\end{aligned}$$

and  $x = \frac{q - q_n}{q_n}$ , where  $q$  is the arterial blood flow defined as,  $q = \frac{p_a - p_c}{R_a}$ . Simplifying to our general state space framework,  $\vec{x} = [p_{ic}, C_a]^T$  is the state vector of intracranial pressure and arterial compliance, respectively,  $v(x, t, \theta)$  is the observation function, and the parameters,  $\theta$ , are given below

$$\theta = \{q_n, p_{vs}, k_E, \tau, G, R_0, R_{pv}, R_f, \Delta C_{a1}, \Delta C_{a2}, C_{an}, k_R, A_c\}.$$

This model has many challenges including nonlinearities, oscillatory input,  $p_a$ , a large number of parameters, single state observation, and stiffness due to varying orders of magnitude in the parameter values. Because of the large number of parameters, we run a subset selection following the same procedure carried out by Fink et al [12] as used in the previous example. This led to 5 of the 13 parameters being found to be identifiable and uncorrelated; they are  $k_E, \tau, G, C_{an}, k_R$ . Before estimating the real data, we first simulated data from the model using nominal values for the parameters and initial conditions, using arterial pressure input from a standard patient. Using stepsize,  $\Delta t = 0.08$ , and noise level,  $w_k = 0.02$ , we created the data with initial conditions,  $[p_{ic}, C_a, \hat{v}]^T = [4.35, 0.15, 77.28]^T$ , and parameter given by Table 2.8.

It is noted that from Table 2.8 the values that were arterial pressure dependent were calculated using the standard patient pressure data. After creating the data, we then went on to estimate the parameters by using a log-transform solely on the parameters.

Setting the covariances appropriately, and perturbing the parameter values to be estimated, we obtain

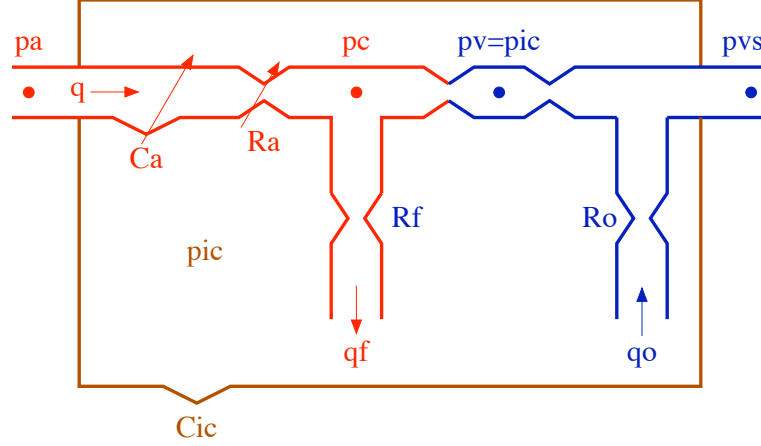


Figure 2.15: Hemodynamic schematic of the simple model of Ursino and Lodi [28]. Arterial (red) and venous (blue) compartments are enclosed within the intracranial space (brown,  $C_{ic}$ : intracranial compliance). Regulated variables ( $C_a$ : arterial compliance,  $R_a$ : arterial resistance) implicitly account for dynamics of hemodynamic variables ( $p_a$ : extracranial arterial blood pressure,  $q$ : MCA territory arterial blood flow,  $p_c$ : capillary blood pressure,  $p_{ic}$ : intracranial pressure,  $p_v$ : intracranial venous blood pressure,  $q_f$ : cerebrospinal fluid (CSF) formation rate,  $q_o$ : CSF outflow rate) and constant hemodynamic variables ( $R_{pv}$ : pial venus flow resistance,  $R_v$ : cortical cerebral venous flow resistance,  $R_f$ : CSF formation resistance,  $R_o$ : CSF outflow resistance,  $p_{vs}$ : venous sinus blood pressure). Reprinted with acknowledgement to Mikio Aoi [2].

our initial conditions as follows

$$\begin{pmatrix} k_{e0} \\ \tau_0 \\ G_0 \\ C_{an0} \\ k_{R0} \end{pmatrix} = \begin{pmatrix} 0.041 \\ 11 \\ 0.6 \\ 0.27 \\ 3e4 \end{pmatrix}, Q = \begin{pmatrix} 0.0001 & 0 & 0 \\ 0 & 0.0001 & 0 \\ 0 & 0 & 0.0001 \end{pmatrix},$$

$$Q_{k_e, \tau, G, C_{an}, k_R} = \begin{pmatrix} 0.0001 & 0 & 0 & 0 & 0 \\ 0 & 0.0001 & 0 & 0 & 0 \\ 0 & 0 & 0.0001 & 0 & 0 \\ 0 & 0 & 0 & 0.0001 & 0 \\ 0 & 0 & 0 & 0 & 0.0001 \end{pmatrix},$$

with  $R = 0.02$ ,  $P_{x_0} = 10I$ , and  $P_{q_0} = 10I$ , where  $I$  is the identity matrix.

Running all the filters over the simulated data, only the ensemble methods successfully converged. While the dual UKF could track the blood flow velocity,  $\hat{v}$ , it failed to get reasonable compliance estimates;  $C_a$  Along with that, the dual UKF not only failed to estimate the parameters, the covariance and

Table 2.8: Parameters of the hemodynamic model of CA. Superscript \* indicates that the value of the parameter was determined by the suggested value in [28]. Subscript  $n$  indicates that the parameter represents a basal value.

Parameter	Description	Initial Value
$p_{cn}$ (mmHg)	Capillary pressure	25*
$p_{icn}$ (mmHg)	ICP	9.5*
$q_n$ (ml/s)	Arterial flow	15.114
$p_{vsn}$ (mmHg)	Venous pressure	6*
$V_{an}$ (ml)	Arterial volume	13.5*
$q_{fn}$ (ml/s)	CSF formation rate	2/300*
$k_E$ (ml <sup>-1</sup> )	Intracranial elastance	.11*
$\tau$ (s)	CA relaxation time	20*
$G$ (unitless)	CA gain	1.5*
$p_{an}$ (mmHg)	Arterial pressure	mean arterial pressure from data
$R_0$ (mmHg · s/ml)	CSF outflow resist.	$(p_{icn} - p_{vsn})/q_{fn}$
$R_f$ (mmHg · s/ml)	CSF formation resist.	$(p_{cn} - p_{icn})/q_{fn}$
$C_{an}$ (ml/mmHg)	Arterial compliance	$V_{an}/(p_{an} - p_{icn})$
$C_{a,mx}$ (ml/mmHg)	Max $C_a$	6 $C_{an}$
$C_{a,mn}$ (ml/mmHg)	Min $C_a$	.5 $C_{an}$
$\Delta C_{a1}$ (ml/mmHg)	$\sigma$ amplitude 1	$2(C_{a,mx} - C_{an})$
$\Delta C_{a2}$ (ml/mmHg)	$\sigma$ amplitude 2	$2(C_{an} - C_{a,mn})$
$R_{an}$ (mmHg · s/ml)	Arterial resistance	$(p_{an} - p_{cn})/q_n$
$R_{pv}$ (mmHg · s/ml)	Pial vein resistance	$R_{an} \frac{p_{icn} - p_{cn}}{p_{cn} - p_{an}}$
$k_R$ (mmHg <sup>3</sup> · s/ml)	Resistance coefficient	$V_{an}^2 \frac{p_{an} - p_{cn}}{C_{an}^2 q_n}$
$A_c$ (cm <sup>2</sup> )	Area of MCA	0.25
$C_{a0}$ (ml/mmHg)	Initial $C_a$	$C_{an}$
$P_{ic0}$ (mmHg)	Initial ICP	$p_{icn}$

confidence in the parameter estimates diverged over time. The dual CKF failed to solve as it encountered numerical errors and completely diverged. The joint filters also failed to estimate due to the limited state observations coupled with the large number of parameters. The lack of success of the deterministic filters stem from their covariance estimation methodology. As they each are using a linearization or numerical approximation to characterize the covariance of the posterior distribution, they are not capturing the true posterior of this system. As these errors accumulate, the confidence in the estimates diverges and the filter resolves to solely fitting the data. This creates poor confidence in the state estimates and a complete failure in the parameter estimates. The ensemble methods succeed in this instance because their covariance calculation is based upon sampling which is more robust to errors. As before, the few poor approximations are cancelled out by the large number of accurate particles, keeping the estimate and covariance closer to the true posterior. To compare the ensemble filter's success to a standard approach in real application, we also ran a nonlinear least squares estimation using Levenberg-Marquardt, LM. From Figure 2.16, the ensemble method, ETKF, is comparable to the nonlinear least squares fit us-



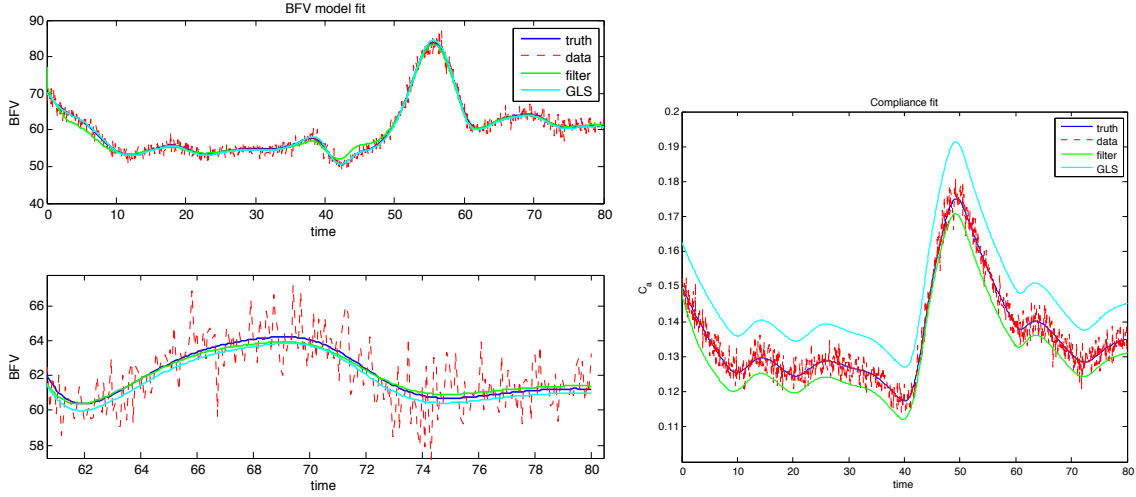


Figure 2.16: Left: simulated data,  $\hat{v}$  (red), true blood flow velocity (blue), filter estimate for simulated blood flow velocity (green), NLS estimate for simulated blood flow velocity (cyan). Bottom plot displays the simulated blood flow velocity and fits due to both methodologies over a shorter time scale. Right: Plot of hidden state  $C_a$  with added noise (red), true solution (blue), filter estimate (green), and NLS estimate (cyan).

ing Levenberg-Marquardt for blood flow; however, the filter seems to more accurately approximate the hidden state;  $C_a$ . The improved fit of the hidden state;  $C_a$ , is likely due to the model's requirement of the patient's blood pressure as an input in terms of predicting blood flow velocity. This adds a level of complexity in that the parameters can not only have sensitivity to the model, but to the input data,  $p_a$ . Any deviations in patient pressure can alter parameter estimates, and the filter is able to capture this due to allowing the parameters to contain temporal dynamics, unlike the NLS approach. The EnKF also converged successfully for this problem, but the results were left out as they were less accurate than the ETKF. From Figure 2.17, the filter's convergence to the parameter estimates can be seen. As mentioned in the previous example, if the parameters are only sensitive in specific areas, they will only shift once those regions are encountered. Also, given that patient pressure data is required in the model as an input,  $\frac{dp_a}{dt}$ , to predict blood flow velocity, the shifts to the estimates can also be related to the sensitivity of the parameters to the inputs. This can explain the convergence plots for each parameter. The full results are displayed in Table 2.9; only a single run is presented as the time for computation was orders of magnitude greater than the previous examples.

Moving onto the real patient data, and using the knowledge gained from the simulated data, we go on to use the ETKF to estimate both the blood flow velocity and parameters for the autoregulation model. Again, we compare the results to the standard nonlinear least squares approach using LM. Using the initial conditions and parameter estimates from the simulated data, the fit to the blood flow velocity is seen in Figure 2.18 for both methods. The sum of squares residual (SSR) and parameter estimates

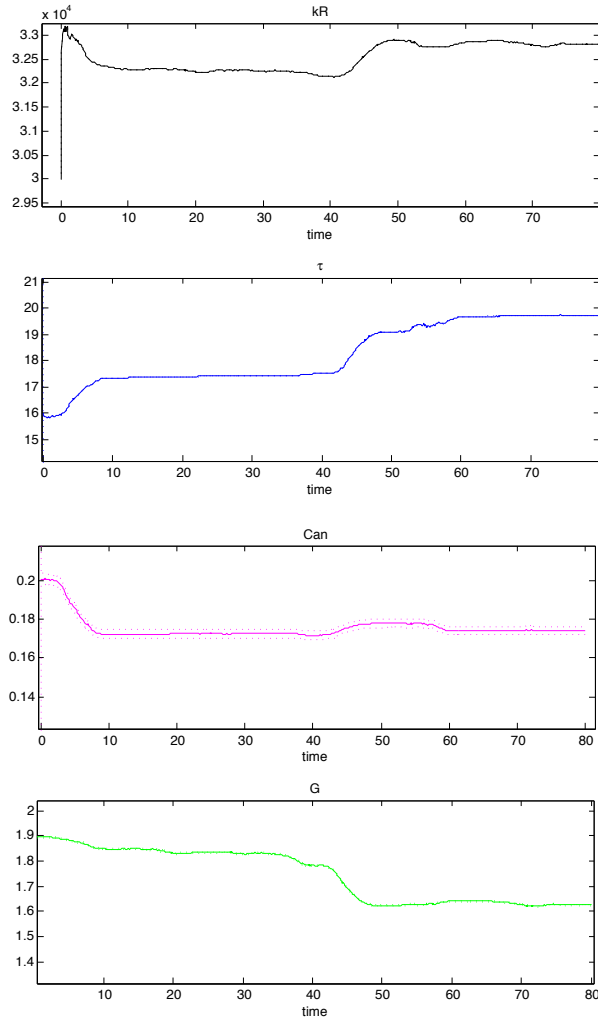


Figure 2.17: parameter estimates for 4 of the 5 parameters for the U-L autoregulation model; (from top to bottom) 1:  $kR$  2:  $\tau$  3:  $C_{an}$  4:  $G$

Table 2.9: Results of ETKF vs. LM for simulated blood flow data with parameters in  $\log_{10}$  space

	truth	NLS	ETKF
SST	0	2.09e3	1.82e3
SSP	0	25.98	24.92
$Ke$ (1 std)	-0.9586	-0.6861	-1.4686 ( 0.0048)
$\tau$ (1 std)	1.301	2.0237	1.2334 (0.002)
$G$ (1 std)	0.1761	1.0035	0.0227 (0.0019)
$C_{an}$ (1 std)	-0.8342	0.0917	-0.9075 (0.003)
$kR$ (1 std)	4.6335	4.5453	4.7344 (0.0004)

are given in Table 2.10. One issue in comparing the filter to the nonlinear least squares approach is that we are looking at the SSR which will be biased towards the NLS approach. Since NLS is based upon a minimization of the residuals, it should exhibit a theoretical minimum for the problem. However, if the covariance is increased for the model while putting large confidence in the data, the filter will track the data without any regard for the model, and it will minimize the residual, but with little regard to the model. So, though the SSR is useful in terms of knowing how well the model may be fitting the data in a relative viewpoint, it is not the best metric for comparison of these two methods. More thought needs to be put into an optimal method to objectively compare the efficiency of each method for a given model fit, full loglikelihood of fit may be more appropriate method. Reviewing the results, the qualitative differences can be seen in the two estimation methods, with the lower SSR for the NLS likely due to the under shoot of the filter when the blood flow dips before reaching its maximum. Reviewing the estimates, substantial differences can be seen which account for the different dynamics. All in all, the ETKF produces comparable results to the NLS, and the fit can be seen in Figure 2.18.

Table 2.10: Results of ETKF vs. LM for real blood flow data with parameters in  $\log_{10}$  space

	NLS	ETKF
SSR	3.58e3	3.80e3
$Ke$ (1 std)	-0.93	-0.89 (0.0022)
$\tau$ (1 std)	1.00	1.09 (0.0009)
$G$ (1 std)	0.33	0.28 (0.0009)
$C_{an}$ (1 std)	-0.75	-0.72 (0.0009)
kR (1 std)	4.61	4.68 (0.0009)

## 2.7 Conclusion

In comparing a multitude of nonlinear filtering techniques for parameter estimation, a number of advantages for each method have been witnessed. The joint extended Kalman filter seems to exhibit the best start point for any state and parameter estimation problem due to its simplicity in implementation coupled with accurate results. It handled the nonlinear dynamics in each example well, even with limited state knowledge. It resolved the parameter accurately, and with high confidence, in each example and was robust to each examples' challenges. Though it did not present the best fit to the states in each case, it did resolve the parameter estimates accurately, and with high confidence, while being robust to each challenge presented. The UKF, both dual and joint, exhibited success in estimation of both the states and parameters as long as there was adequate data present. These methods struggled in the Lorenz example when only one state was being observed. Their level of robustness and accuracy were good, but depen-

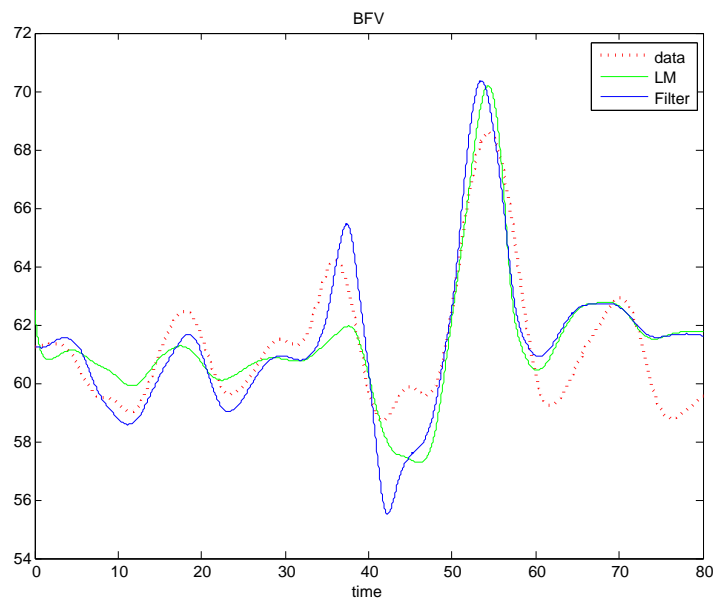


Figure 2.18: Plot of blood flow velocity data (red), filter estimate for the blood flow velocity (blue) and NLS model estimate for blood flow velocity (green). The NLS approach is using optimized values

dent upon high levels of state knowledge. However, the ability to run without model linearizations gives this method a distinct advantage in runtime and simplicity that the EKF does not exhibit. The joint CKF and dual CKF exhibited equivalent results to the UKF methods, but with failure in many cases where the UKF methods still succeeded. The negligible difference in accuracy coupled with the higher failure rate makes the CKF method's less usefulness in applications. The ensemble method's only shortcoming is its inability to span the space well in long runs. Since it does well to converge to the appropriate answer, the confidence in the estimate increases and large changes take longer to be corrected. Updating the ensemble with the model and parameter noise processes, the ensemble Kalman filters overcame this adversity and produced the best results in state and parameter estimates for real data. The only other potential drawback is the increase in computational time as it scales proportionally to the number of particles. However, if time is not an issue, the ensemble methods were comparable to the best estimates, with high confidence, in all three examples. The ensemble methods were also the only methods to converge on the real data. While the other methods could not sufficiently handle the covariance updates for the final example, the ensemble methods demonstrated a high level of robustness and success in the most challenging problems. In cases of extreme complexity and challenge, the ensemble methods seem to be the best method to choose.

Overall, although the extended Kalman filter is the best start point due to simplicity, the ensemble filters were the best filter for our applications. The UKF obtained the same level of accuracy as the CKF in all examples where both converged, however, the UKF converged more frequently than the CKF. The dual UKF and CKF exhibited less variation in estimates and failed less frequently than their joint counterparts. The EKF succeeded in estimating both the states and parameters in the first two applications, but failed in the last application. The ensemble filters managed to succeed in every example including the real data problem.

We have used nonlinear filtering techniques for the estimation of both the states and parameters and shown comparable results when compared to the standard cost function minimization method. In cases where online parameter estimation is necessary or parameter values can shift temporally, nonlinear filtering has shown favorable results.

## REFERENCES

- [1] Anderson, B. "An Ensemble Adjustment Filter for Data Assimilation." Monthly Weather Review, Vol. 129, 2001, Pgs. 2884-2903
- [2] Aoi, M. Nonlinear, Noninvasive Assessment of Patient-Specific Cerebral Autoregulation in Stroke Subjects. PhD thesis, North Carolina State University, 2011.
- [3] Arasaratnam, I. and Haykin, S. "Cubature Kalman Filters." IEEE Transactions in Automatic Control. Vol. 54, 2009. Pgs. 1254-1269.
- [4] Arasaratnam, I., Haykin, S., and Hurd, T. "Cubature Kalman Filtering for Continuous-Discrete Systems: Theory and Simulations." IEEE Transactions on Signal Processing. Vol. 58, No. 10, 2010, Pgs. 4977-4993
- [5] Arulampalam, S. M., Maskell, S., Gordon, N., and Clapp, T. "A Tutorial on Particle Filters for Online Nonlinear/Non-Gaussian Bayesian Tracking." IEEE Transactions on Signal Processing. Vol. 50, no. 2, 2002, Pgs. 174-188.
- [6] Bishop, C.H., Etherton, B.J., and Majumdar, S.J. "Adaptive Sampling with the Ensemble Transform Kalman Filter. Part I: Theoretical Aspects." Monthly Weather Review. Vol. 129, Pgs. 420-436.
- [7] Candy, J. V. Bayesian Signal Processing: Classical, Modern and Particle Filtering Methods. New Jersey: John Wiley and Sons, Inc., 2009.
- [8] Daum, F. "Nonlinear Filters: Beyond the Kalman Filter." IEEE AE Systems Magazine. Vol. 20, No. 8, 2005. Pgs. 57-69.
- [9] Evensen, G. Data Assimilation: The Ensemble Kalman Filter. New York: Springer, 2009.
- [10] Evensen, G. "The Ensemble Kalman Filter for Combined State and Parameter Estimation." IEEE Control Systems Magazine. Vol. 29, 2009. Pgs. 83-104.
- [11] Evensen, G. "The Ensemble Kalman Filter: Theoretical Formulation and Practical Implementation." Ocean Dynamics. Vol. 54, 2003. Pgs. 539-560.

- [12] Fink, M., Attarian, A., and Tran, H. "Subset Selection for Parameter Estimation in an HIV Model." PAMM. Vol. 7, No. 1, 2008. Pgs. 1121501-1121502.
- [13] Gershgorin, Majda, and Harlim, J. "Mathematical Strategies for Filtering Turbulent Dynamical Systems." Discrete Contin. Dynam. Syst. A, Vol. 27, No. 2, 2010. Pgs. 441-486
- [14] Haykin, S. Kalman Filtering and Neural Networks. New York: John Wiley and Sons, Inc., 2001.
- [15] Hunt, B., Kostelich, E., and Szunyogh, I. "Efficient Data Assimilation for Spatiotemporal Chaos: A Local Ensemble Transform Kalman Filter." Physica D, Vol. 230, 2007, Pgs. 123-137.
- [16] Julier, S., J. and Uhlmann, J. K. "A New Extension of the Kalman filter to Nonlinear Systems." In Proc. of Aerosense: The 11th Int. Symp. on Aerospace/Defense Sensing, Simulation and Controls. 1997.
- [17] Kalman, R. E. "A New Approach to Linear Filtering and Prediction Problems." ASME J. Basic Engineering. Vol. 82, 1960, Pgs. 34-45.
- [18] Kelley, C.T. Iterative Methods for Optimization. SIAM, Philadelphia, PA, 1999.
- [19] Lewis, F. L. Optimal Estimation. New York: John Wiley and Sons, Inc., 1986.
- [20] Lorenz, E. N. "Deterministic Nonperiodic Flow." Journal of the Atmospheric Sciences. Vol. 20, 1963. Pgs. 130-141.
- [21] Majda, A.J. and Harlim, J. Filtering complex turbulent systems. Cambridge University Press, UK, 2012.
- [22] Mordakhani, H., Sorooshian, S., Gupta, H.V., and House, P.R. "Dual state-parameter estimation of hydrological models using ensemble Kalman filter." Advances in Water Resources. Vol. 28, Pgs. 135-147.
- [23] Nelson, A.T. Nonlinear Estimation and Modeling of Noisy Time-series by Dual Kalman Filtering Methods. PhD Thesis, Oregon Graduate Institute, 2000.

- [24] Nelson, L.W. and Stear, E. "The simultaneous on-line estimation of parameters and states in linear systems." IEEE Transactions on Automatic Control. Vol. AC-12, 1996, Pgs. 438-442.
- [25] Ristic, B., Arulampalam, S., and Gordon, N. Beyond the Kalman Filter: Particle filters for tracking applications. Boston: Artech House, 2004.
- [26] Sarkka, S. "On Unscented Kalman Filtering for State Estimation of Continuous-Time Nonlinear Systems." IEEE Transactions on Automatic Control. Vol. 52, No. 9, 2007. Pgs. 1631-1641.
- [27] Sarkka, S. Bayesian Filtering and Smoothing. Cambridge University Press, UK, 2013.
- [28] Ursino, M. and Lodi, C. A. "A Simple Mathematical Model of the Interaction between Intracranial Pressure and Cerebral Hemodynamics." Journal of Applied Physiology. Vol. 82, 1997. Pgs. 1256-1269.
- [29] Wann, E. and Van Der Merwe, R. "The Unscented Kalman Filter for Nonlinear Estimation." Adaptive Systems for Signal Processing, Communications, and Control Symposium, IEEE. 2001. Pgs. 153-158.
- [30] Wan, E. and Van Der Merwe, R. "The Square-Root Unscented Kalman Filter for State and Parameter Estimation." IEEE International Conference on Acoustics, Speech and Signal Processing. Vol. 6, 2001. Pgs. 3461-3464.
- [31] Wan, E.A., Van Der Merwe, R., and Nelson, A.T. "Dual Estimation and the Unscented Transformation," in S.A. Solla, T.K. Leen, and K.R. Muller, Eds. Advances in Neural Information Processing Systems 12, Cambridge, MA: MIT Press, 2000, Pgs. 666-672.
- [32] Wan, E.A., and Nelson, A.T. "Dual Kalman Filtering for nonlinear prediction, estimation and smoothing." Advances in Neural Information Processing Systems. Vol. 9, 1997.



## Chapter 3

# Physiology Background

Given the overview of filtering techniques in the previous chapter, and their application to modeling problems, the purpose is to utilize these filtering methods to help better understand the control systems of the cardiovascular system. However, before proceeding to do so, this chapter presents an overview of the physiology of the cardiovascular system, including vasculature and the autonomic regulation aspects governing blood flow. General information comes from Boron and Boulpaep [1], Brunton et al. [2], and Fox [6].

### 3.1 The Cardiovascular System

The primary responsibility of the cardiovascular system (CVS) is the transportation of nutrients (amino and fatty acids, vitamins, hormones, etc) and oxygen to the tissues; and removing wastes (i.e. carbon dioxide and urea) from the body. Using blood as a transport mechanism, the CVS consists of two main components, the large systemic division and smaller pulmonary division, connected by the heart. The pulmonary branch, consisting of the pulmonary arteries, capillaries, and pulmonary veins, pumps blood from the right ventricle to the lungs and then returns to the left atrium, which then fills into the left ventricle and is ejected into systemic circulation throughout the body, consisting of the aorta, arterial branches, capillaries, veins, and venae cavae. Blood finally returns to the right atrium where the process repeats; this is illustrated in Figure 3.1. These two divisions form a closed circuit which are serially connected, and serve important functions. The pulmonary branch facilitates exchange of oxygen and carbon dioxide within the lungs, while the systemic branch facilitates the transportation of blood and nutrients while draining wastes from the tissues and organs of the body. Although both branches are governed by the heart similarly, they exhibit different operating conditions. Systemic circulation has a much higher volume, it's vessels are longer and thicker, and it operates with a higher pressure within the arteries with more resistance to flow. The operating blood pressures for each branch are visualized in Figure 3.2.

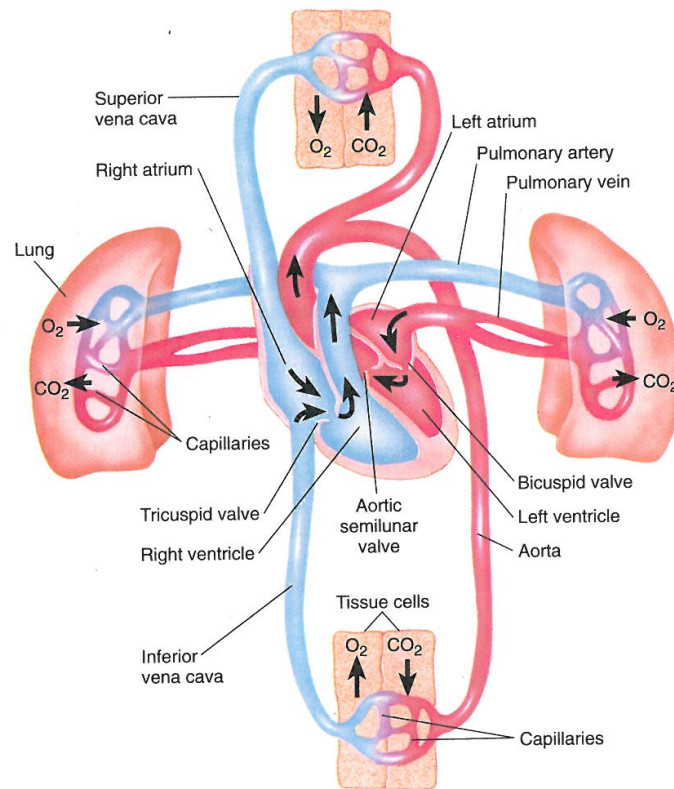


Figure 3.1: Blood flow from the left ventricle through the systemic arteries and veins to the right atrium. It is then ejected from the right ventricle and pumped through the pulmonary circulation back to the left atrium. Systemic arteries and pulmonary veins are  $O_2$ -rich,  $CO_2$ -poor blood, while systemic veins and pulmonary arteries are  $O_2$  poor and  $CO_2$  rich. Reprinted from [6].

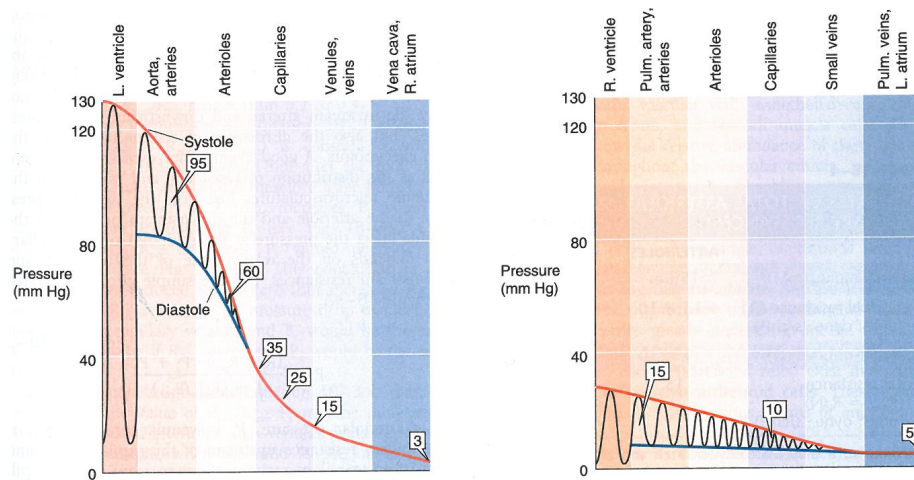


Figure 3.2: Left: Typical pressure during systemic circulation. Right: Typical pressure in pulmonary circulation. In both, the oscillations represent variations in time, not distance. Reprinted with permission from [1].

This entire process is controlled by the heart. The centerpiece for the vasculature and cardiac cycle, the heart consists of four chambers, two each for the left and right hearts which feed the systemic and pulmonary systems, respectively. Each side of the heart consists of an atrium and ventricle with the former being a primer for the latter [4]. Each side of the heart outputs the same volume of blood per unit time, deemed the cardiac output (CO) [m/s]. Valves at the inlet and outlet of the ventricles allow pressure to build up, preventing back-flow of blood. Atrioventricular valves separate the atria from the ventricles, and semilunar valves are located at the exit of the ventricles. For the left ventricle, the mitral valve separates the atrium from the ventricle and the aortic valve is the outlet. For the right ventricle, the tricuspid valve separates the atrium and the pulmonary valve is the outlet. These heart chambers work in synchrony due to electrical coupling of the cardiac muscle fibers. The pumping of the heart is activated by an electrical cascade triggered by an action potential, which starts in the sinoatrial (SA) node and spreads through the myocardial cells of the right and left atria. Since fibrous tissue separates the atria and ventricles, the electrical impulse cannot directly travel down the heart, but requires the special modified, conducting myocardial cells of the atrioventricular node (AV) to continue. This signal then cascades down the bundle of His along the interventricular septum, where it splits into right and left bundles branches. The signal finally arrives at the Purkinje fibers within the ventricular walls resulting in the contraction of cardiac muscle cells and the pumping of the heart [2]. More specifically, the direct consequence of this process is the cardiac cycle. Defined in Figure 3.4, starting at 'F', upon completing contraction, the aortic valve closes resulting in the diastole phase in which the left ventricle undergoes isovolumetric relaxation. Once the isovolumetric relaxation ends and the pressure in the atrium is greater than the ventricle, the mitral valve between the left atrium and left ventricle opens resulting in the left

ventricle filling with blood passively, 'A'. Then as the volume increases to the point that pressure starts to increase, upon arriving at 'C', the mitral valve closes and isovolumetric contraction occurs. The left ventricle begins to contract increasing the pressure without changing the volume. Finally, 'D', the pressure increases to the point the aortic valve opens causing ventricular ejection, the systole phase. During each of these contractions of the left ventricle, blood is transported through the aorta at pressures between 80 and 120 mmHg. Traveling through systemic circulation, the arteries branch into arterioles then into capillaries where oxygen ( $O_2$ ) and nutrients diffuse across the vessel barrier while carbon dioxide ( $CO_2$ ) and other metabolites diffuse in the reverse direction into the blood stream (see Figure 3.5). Subsequently, this semi-deoxygenated, waste filled blood is transported through the veins, and venous side of systemic circulation, back to the right atria at pressures around  $\sim 2$ mmHg [6]. By contrast, in the pulmonary branch, blood flow operates at a relatively low pressure, with a lower right ventricle pressure of  $\sim 25$ mmHg, but higher venous pressure of  $\sim 8$ mmHg [6].

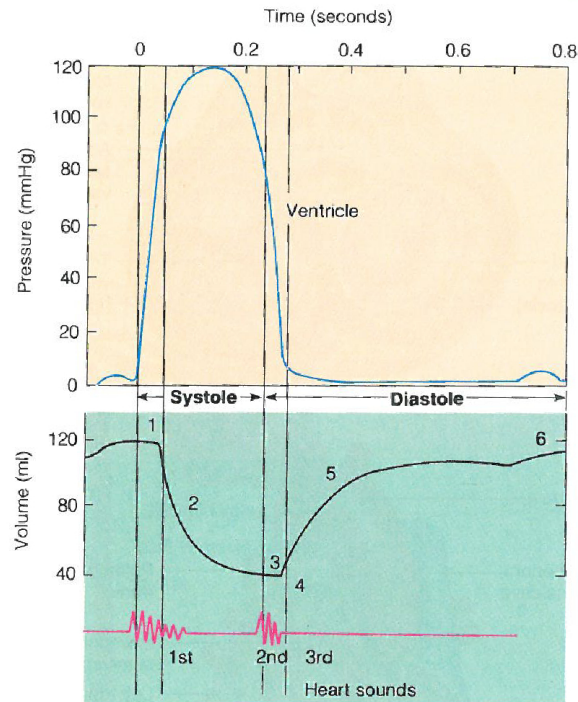


Figure 3.3: Diagram of a typical cardiac cycle. The figure shows the relationship between heart sounds and the intraventricular pressure and volume. The top graph represents the pressures in the left ventricle and left atrium. The bottom graph shows the ventricular volume. Reprinted with permission from [6].

In terms of blood volume, the average total blood volume within the body is  $\sim 5$  liters; however, this is not uniformly distributed throughout the body, but divided amongst the systemic circulation

(~85%), pulmonary circulation (~10%), and the heart (~5%) [1]. Within circulation, the majority of the total blood volume is contained in the venous component. In general, the veins serve as the storage vessels while the arteries' purpose is to regulate blood flow and pressure throughout the body. As the flow goes through the arterial network, the number of vessels and the total cross-sectional area of the vasculature increases exponentially as blood travels into the capillaries (Figure 3.5). These capillaries receive blood from the arterioles for distribution throughout tissues. The network of capillaries form a mesh-like structure made up mostly of endothelial cells wide enough only to accommodate a single red blood cell (about  $2\text{-}5\mu\text{m}$ ). Due to loss of pressure as the system branches and the vessels' radius narrow, the blood flow rate is relatively slow at the capillaries making diffusion of metabolites between tissues and the vessels easy [1]. Unlike the arterial network which has high pressure and elastic vessels, the venous network acts as a conduit for metabolite removal from the tissue and is primarily collagen, a non-elastic connective tissue. This leads to their high compliance, the ability to store a large volume of blood while incurring minimal change, giving the veins the name "capacitance vessels." [1, 4]. Due to the greatly reduced blood pressure in the venous system being insufficient to return blood to the heart (Figure 3.2), veins have infrastructure to ensure one way flow known as venous valves. These venous valves are a function of the veins passing between skeletal muscle groups that provide a massaging action, which prevents flow away from the heart [6]. This feature of the veins ensures blood returns to the heart where the cardiac cycle can repeat. A complete cardiac cycle typically lasts 0.8s, which corresponds to a average heart rate of 75 beats/min [1, 4].

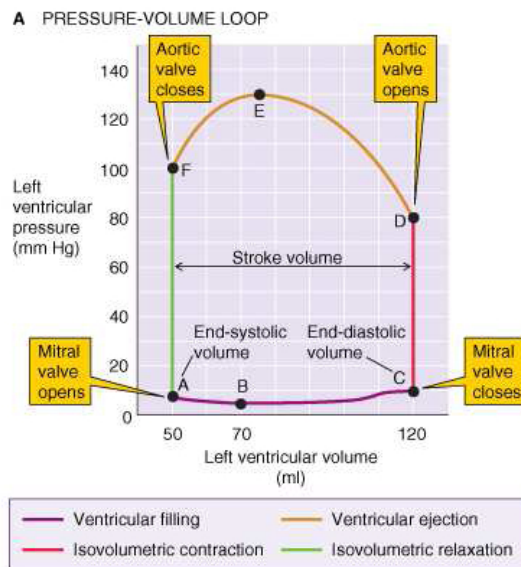


Figure 3.4: Pressure-volume loop and four phases of the cardiac cycle. Line segments represent AC: Diastole, CD: Contraction, DF: systole, FA: relaxation. Reprinted with permission from [1].

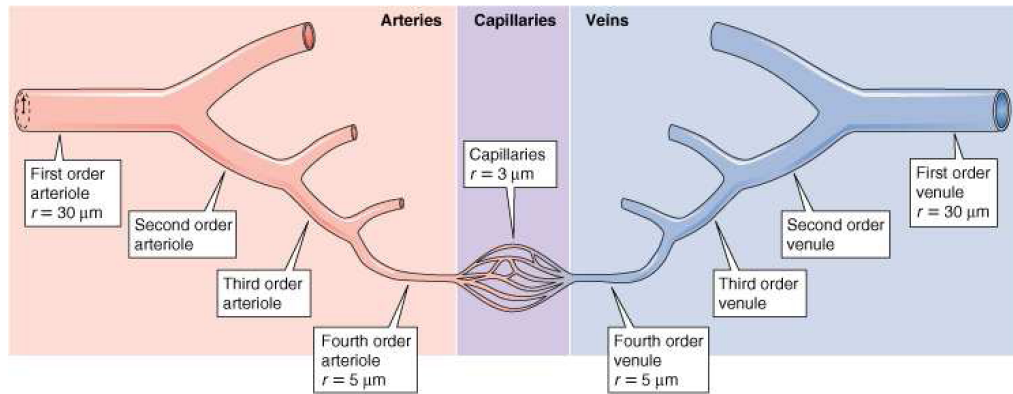


Figure 3.5: Branching structure of the typical vascular bed. Reprinted with permission from [1].

## 3.2 Cardiovascular Regulation

Autonomic regulation uses information about blood pressure and blood gas concentrations, obtained by baroreceptors and chemoreceptors, and sends it to the CNS via afferent sensory neurons to produce an output signal, which is utilized by the body through transport through efferent motor neurons. In the CNS, cardiovascular activity is regulated by the medulla. Baroreceptors, located in the carotid sinus and aortic arch, respond to perturbations in vessel wall distention due to arterial pressure change. Decreased arterial pressure results in small wall distention, which results in a decrease in baroreceptor firing rate. The medulla assimilates this information and activates the sympathetic nervous system as described above to rectify these deviations. Neurotransmitters, norepinephrine and epinephrine, are released which trigger the cascade of effects from the sympathetic system such as increased heart rate, increased cardiac contractility and increased vascular resistance. This leads to an increase in stroke volume and cardiac output leading to an increase in arterial pressure which rectifies the baroreceptor decrease viewed and signaled to the medulla [4]. Because the sympathetic control of heart rate and regulation is a more gradual process, not able to exert beat-by-beat control, the parasympathetic system is also withdrawing during this time which helps mediate the increase of heart rate [8].

All of the mechanics governing the heart and cardiovascular system are controlled by the body to maintain a level of stability known as "homeostasis." When a stimulus perturbs the system away from baseline, a feedback is activated to regulate the system and return it to homeostasis. A sensor in the system recognizes a disturbance and sends correcting information via an integrator to the effector, which acts to bring the property back to intended operating values. One of the main global feedback control mechanisms found in the body is the autonomic nervous system, which utilizes the central nervous system (CNS) for signal integration and the peripheral nervous system (PNS) for signal dissemination

[4].

The hypothalamus and solitary tract nucleus are generally regarded as the loci of integration of autonomic nervous function, among which contains blood pressure and respiration. The sympathetic system is not essential to life in a controlled environment, but lack of the system becomes more evident in times of stress [2]. In other words, the sympathetic nervous system is always active and used to constantly adjust to a changing environment. When the sympathetic nervous system is active, heart rate is increased, blood pressure rises, and blood flow is shifted from the skin and splanchnic region to skeletal muscle. This can be seen from a head-up tilt experiment through the arterial baroreflex regulation. As the tilt occurs, the drop in pressure causes the sympathetic activation through the baroreflex, which results in increased heart rate and contractility [9]. The parasympathetic system is antagonizing to the sympathetic and is more necessary for survival as its primary concern is conservation of energy and maintaining organ function. Because of its antagonizing theme, it affects the cardiovascular system by slowing heart rate and lowering blood pressure. In general, the parasympathetic system responds to deviations due to the direct connection via the vagus nerve (a delay of 0.5 s), while the sympathetic nervous system must synapse through the ganglia (reflex response delay of 2.0 s) [7]. Friedman et. al. [10] used a pharmacological autonomic blockade to show the effects of a subject with autonomic dysfunction through an impaired parasympathetic pathway. This has been shown to lead to an increased heart rate and blood pressure. These pathways and their affects are shown in Figure 3.6

During head-up tilt, blood pools in the legs due to gravity which decreases blood pressure in the upper body activating the sympathetic system. The sympathetic system causes an increase in heart rate via the sinoatrial node, increase in automaticity and conduction velocity in the atrioventricular node, increase in automaticity and conduction velocity in the Purkinje bundle, and an increase in contractility, conduction velocity, and rate of atrioventricular pacemakers in the ventricle to account for this decreased blood pressure. However, the parasympathetic system decreases the heart rate via the sinoatrial node, decreases contractility and shortens AP duration in the atria, decreases conduction velocity in atrioventricular node, and causes a slight decrease of contractility in the ventricle. This is done through modulation via neurotransmitters [2].

For a normally functioning heart, the primary mechanism by which cardiac output is maintained is the recruitment of preload reserve; a dynamic reduction of venous capacitance that results in centralization of peripheral blood volume and enhanced venous return, thereby increasing left ventricle end diastolic volume which leads to an increase in stroke volume [4]. If this is not functioning correctly or the heart is experiencing acute circulatory stress, the sympathetic branch of the autonomic nervous system can be activated which will increase the myocardial contractility, increased heart rate, and increased vascular resistance. This will all work to increase the preload recruitment and help provide sufficient forward cardiac output to the body.

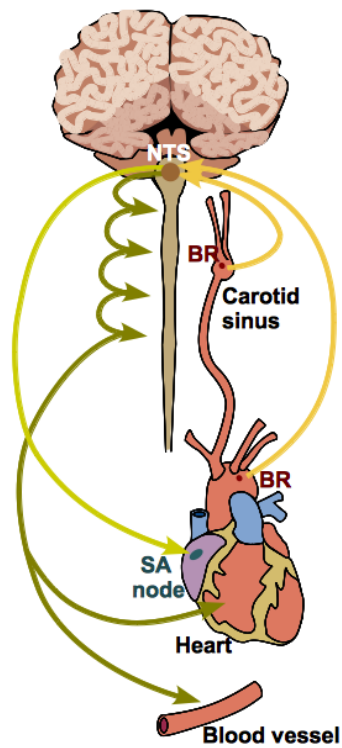


Figure 3.6: Diagram of the pathways by which the sympathetic and parasympathetic system's interact with the heart and vasculature. As seen, the sympathetic system synapses through the ganglia in the spine (green paths) while the parasympathetic has a more direct connection (yellow paths). The sympathetic system can affect both the heart and vasculature, while the parasympathetic only directly affects the heart. Reprinted with acknowledgement to Alison Margolskee.



## REFERENCES

- [1] Boron, W.F. and Boulpaep, E.L. Medical Physiology. Philadelphia, PA: Saunders, 2003.
- [2] Brunton, L.L., Lazo, J.S., and Parker, K.L. The Pharmacological Basis of Therapeutics. New York: McGraw-Hill, 2006.
- [3] Bugenhagen, S., Cowley, A., and Beard, D. "Identifying physiological origins of baroreflex dysfunction in salt-sensitive hypertension in the Dahl SS rat." Physiological Genomics. 2010. Vol. 42, Pgs. 23-41.
- [4] Ellwein, L.M. *Cardiovascular and Respiratory Regulation, Modeling, and Parameter Estimation*. PhD Thesis. North Carolina State University, 2008.
- [5] "Schematic overview of the cardiovascular system." Diagram, 2012, Biology-Forums.com, <http://biology-forums.com/index.php?action=gallery;sa=view;id=9172>, Web, April 8th 2014.
- [6] Fox, S.I. Human Physiology. New York, NY: McGraw-Hill, seventh edition, 2002.
- [7] Heldt, T., Shim, E., Kamm, R., and Mark, R. "Computational Modeling of Cardiovascular Response to Orthostatic Stress." Journal of Applied Physiology. 2002. Vol. 92, Pgs. 1239-1254.
- [8] Olufsen, M., Ottesen, J., Tran, H., Ellwein, L., Lipsitz, L., and Novak, V. "Blood pressure and blood flow variation during postural change from sitting to standing: model development and validation." Journal of Applied Physiology. 2005. Vol. 99, Pgs. 1523-1537.
- [9] Ottesen, J., and Olufsen, M. "Functionality of the baroreceptor nerves in heart rate regulation." Computer Methods and Programs in Biomedicine. 2005. Vol. 101, Pgs 208-219.
- [10] Triedman, J., and Paul, J. "Blood pressure modulation by central venous pressure and respiration. Buffering effects of the heart rate reflexes." Circulation. 1994. Vol. 89, Pgs. 169-179.

## Chapter 4

# Time Varying Resistance in a Baroreflex Regulation Model During Head-Up Tilt

### 4.1 Introduction

Over short time scales (seconds to minutes), the body's requirement to distribute and maintain adequate amounts of oxygenated blood to vital areas is paramount to maintain homeostasis. This feature is controlled via multiple mechanisms, but primarily by the baroreflex system, which senses changes in aortic and carotid blood pressure, stimulating the sympathetic and parasympathetic systems. The sympathetic system induces alterations in heart rate, cardiac contractility, vascular resistance, and compliance, while the parasympathetic system induces rapid changes in heart rate and cardiac contractility [18, 47, 58].

A number of modeling studies have been carried out to elucidate further understanding of these mechanisms and their interplay [4, 24, 32, 40, 42, 45, 46, 55, 58]. Most of these studies can be separated into two categories, models predicting baroreflex regulation of heart rate as a function of blood pressure [4, 32, 42, 55] and models predicting blood pressure dynamics as function of heart rate [24, 28, 40, 46, 58]. A few other studies include more elaborate models predicting the interaction between the cardiovascular and respiratory systems [2, 10, 55]. Finally, numerous studies, e.g. [11, 17, 21, 31, 51, 54, 57] assess baroreflex regulation quantitatively via analysis of the measured signals using a variety of signal processing methods, most commonly based on transfer function analysis.

This chapter focusses on development of a model that uses heart rate to predict arterial blood pressure dynamics during head-up tilt (HUT) [11, 17, 21, 51, 58]. HUT is a non-invasive test often used to determine the ability of the body to maintain blood flow and pressure for patients suffering from syncope, lightheadedness, and dizziness [30, 38]. The test starts with a patient lying on a tilt-table in supine position, after steady signals have been recorded, the patient is tilted head-up to an angle of 60-70 degrees. In response to the tilt, gravity pools 500-1000ml of blood in the lower extremities [30, 58]. The result is a decrease in venous return, which causes a decrease in cardiac filling, and blood pressure

in the upper body (above the body's center of gravity), while the blood pressure in the lower body (below the body's center of gravity) is increased. The body senses this change in blood pressure by baroreceptors located in the aortic arch and carotid sinuses, and responds by sympathetic activation and parasympathetic withdrawal [58]. This autonomic neural modulation leads to an increase in heart rate, cardiac contractility, vascular resistance, and vascular tone.

This study compares two methods for prediction of neural regulation of cardiac contractility and vascular resistance. Focus is on estimating time-varying changes of these quantities in response to HUT. Similar to the study by Williams et al. [58], the first method uses piecewise linear splines, while the second uses the "Ensemble Transform Kalman Filter" (ETKF) for prediction of these quantities. Moreover, we show that the Delayed-Rejection Adaptive Metropolis Hastings (DRAM) algorithm can be used for prediction of parameter uncertainties within the spline methodology, and compared to variability obtained from the ETKF.

The remainder of the chapter shall proceed as follows; the mathematical model will first be derived in two parts. Then, identifiability and sensitivity will be considered. Next, the linear spline methodology will be explained, along with the use of DRAM for parameter uncertainty. The Kalman filtering methodology will follow. Lastly, the results and discussion will be presented.

## 4.2 Mathematical Model

This section presents the cardiovascular model developed in [58] to describe blood flows, volumes, and pressures in the systemic circulation during HUT and is split into two parts: a lumped cardiovascular model predicting dynamics while patient is resting, and a model predicting the dynamic shifts due to the response to the HUT.

### 4.2.1 Lumped cardiovascular model

The basic cardiovascular model is derived through an analogy of an electrical RC-circuit with pressure analogous to flow, charge analogous to volume, compliance analogous to capacitance, and resistance consistent for both. Using Figure 4.1, it can be seen that the model contains 5 compartments representing the arteries and veins in the upper and lower body of systemic circulation, comprised of "Wind-kessel" components linked to a compartment representing the left ventricle. For this model, the upper body compartments include arteries and veins in the head, thorax, and abdomen, while the lower body compartments include all the vessels in the legs. Given the RC-circuit framework, the model will be able to predict blood pressure and flow in the compartments, but will not accurately capture the pulsatile nature of the wave-propagation in the arterial network. Therefore, this study is limited to the prediction of the systolic and diastolic pressures.

Within each of the four arterial and venous compartments (indexed by  $i$ ), pressure  $p_i$  (mmHg) and

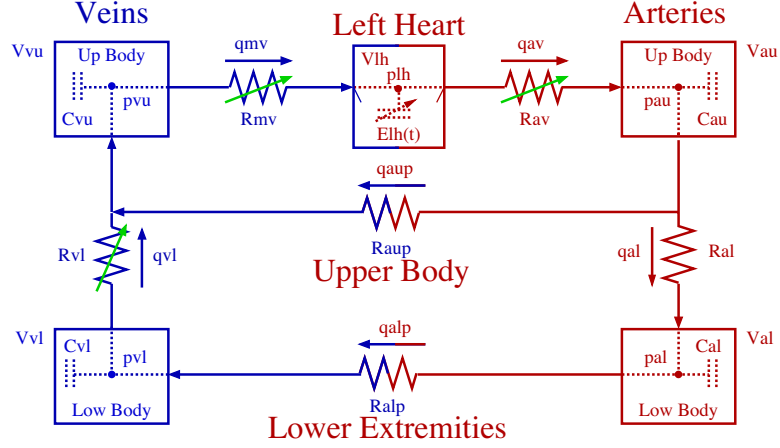


Figure 4.1: Compartment model used for predicting HUT dynamics in the systemic circulation. The model includes five compartments representing the left heart (lh), arteries (a), and veins (v) in the upper (u) and lower (l) body. Flows are marked by  $q$ , pressures by  $p$ , volumes by  $V$ , resistors by  $R$ , compliances by  $C$ . The opening and closing of the aortic (av) and mitral (mv) valves and prevention of retrograde flow through systemic veins are modeled via pressure-varying resistors.

volume  $V_i$  (ml) can be related by

$$V - V_{un} = C(p - p_{ext}), \quad (4.1)$$

where  $V_{un}$  (ml) is the unstressed volume,  $C$  (ml/mmHg) is the compartment compliance, and  $p_{ext} = 0$  (mmHg) is the pressure in the surrounding tissue.

Using Ohm's law to describe the volumetric flow,  $q$ , between two compartments is given by

$$q = \frac{p_{in} - p_{out}}{R}, \quad (4.2)$$

where  $p_{in}$  and  $p_{out}$  are the pressures on each side of the resistor,  $R$  (mmHg s/ml), respectively. Differentiating (4.1) with respect to time and applying Ohm's law (4.2), we obtain the system of ordinary differential equations for pressure of the form

$$\frac{dV}{dt} = C \frac{dp_i}{dt} = \frac{p_{i-1} - p_i}{R_{i-1}} - \frac{p_i - p_{i+1}}{R_i}.$$

This holds and is valid since we assume that  $C$  (ml/mmHg) is constant. This formulation is used for the four body compartments, but a different formulation is derived for the heart due to the changes in volume in accordance with pumping. For the heart compartment, the change in volume is obtained by the differential equation,

$$\frac{dV_{lh}}{dt} = q_{in} - q_{out}.$$

For the heart, pressure is calculated directly by using the pressure-volume relation

$$p_{lh} = E_{lh}(V_{lh} - V_{un}), \quad (4.3)$$

where  $E_{lh}$  is the elastance (reciprocal of the compliance). The pumping of the heart is achieved by introducing a variable elastance function [10] that depends on the heart rate,  $H$ , and includes a defined time for the start of relaxation. Using the elastance function proposed by Ellwein [10], our elastance becomes

$$E_{lh}(\tilde{t}) = \begin{cases} \frac{E_{max}-E_{min}}{2} [1 - \cos(\frac{\pi\tilde{t}}{T_M})] + E_{min}, & 0 \leq \tilde{t} \leq T_M \\ \frac{E_{max}-E_{min}}{2} [\cos(\frac{\pi(\tilde{t}-T_M)}{T_R}) + 1] + E_{min}, & T_M \leq \tilde{t} \leq T_M + T_R \\ E_{min} & T_M + T_R \leq \tilde{t} \leq T, \end{cases} \quad (4.4)$$

where  $\tilde{t}$  is the time within a cardiac cycle,  $E_{min}$  and  $E_{max}$  denote the maximum and minimum elastance, respectively. Then, for each cardiac cycle,  $T = \frac{1}{H}$ , elastance is increasing over the interval  $0 \leq t \leq T_M$ , decreasing for  $T_M \leq t \leq T_M + T_R$ , and held constant at its minimum value,  $E_{min}$ , during diastole,  $T_M + T_R \leq t \leq T$ . The values for final time,  $T$ , and the time of maximal elastance,  $T_M$ , are obtained from data while  $T_R$  is a model parameter.

Lastly, the heart valves are modeled using a time-varying resistance for which a large resistance  $R_{cl}$  represents a closed valve, while a small resistance  $R_{op}$  is indicative of an open valve. This is modeled smoothly as

$$R_v = R_{cl} - \frac{R_{cl} - R_{op}}{1 + e^{-\beta(p_{in} - p_{out})}}, \quad (4.5)$$

where  $p_{in}$  and  $p_{out}$  denote the pressures in the compartments on either side of the valve.

Using these relations, the system of differential equations becomes

$$\begin{aligned} \frac{dp_{au}}{dt} &= (q_{av} - q_{al} - q_{aup})/C_{au}, \\ \frac{dp_{al}}{dt} &= (q_{al} - q_{alp})/C_{al}, \\ \frac{dp_{vl}}{dt} &= (q_{alp} - q_{vl})/C_{vl}, \\ \frac{dp_{vu}}{dt} &= (q_{aup} + q_{vl} - q_{mv})/C_{vu}, \\ \frac{dV_{lh}}{dt} &= q_{mv} - q_{av}, \end{aligned}$$

where

$$\begin{aligned}
q_{av} &= \frac{p_{lh} - p_{au}}{R_{av}}, \\
q_{aup} &= \frac{p_{au} - p_{vu}}{R_{aup}}, \\
q_{al} &= \frac{p_{au} - p_{al}}{R_{al}}, \\
q_{alp} &= \frac{p_{al} - p_{vl}}{R_{alp}}, \\
q_{vl} &= \frac{p_{vl} - p_{vu}}{R_{vl}}, \\
q_{mv} &= \frac{p_{vu} - p_{lh}}{R_{mv}}.
\end{aligned}$$

In the equations for the flows,  $q$ , the left ventricular pressure,  $p_{lh}$ , is calculated using (4.3). The abbreviations can be seen in Table 4.1, below.

Table 4.1: Subscript descriptions used in compartment model from [58].

Abbreviation	Details
<i>av</i>	aortic valve
<i>au</i>	upper body arteries
<i>al</i>	lower body arteries
<i>aup</i>	upper body "peripheral" vascular bed
<i>alp</i>	lower body "peripheral" vascular bed
<i>vu</i>	upper body veins
<i>lh</i>	left ventricle (heart)

### 4.2.2 HUT model dynamics

The model derivation thus far has dealt with the cardiovascular dynamics while in the supine position. Once the HUT occurs, gravity will affect the system by causing blood to pool in the lower extremities which leads to an increase in pressure in the lower body, while also decreasing pressure in the upper body. This response is accounted for by modeling the hydrostatic pressure on each compartment. Using the pressure at the level of the carotid arteries as a reference point, an extra term is added to the flows to ( $q_{al}$ ) and from ( $q_{vl}$ ) the lower body compartments. For simplicity, we assume the tilt-axis is placed at the level of the lower body compartments. Using the calculation from [39] for the gravitational effects,

the modified flow equations are given by

$$q = \frac{\rho g h \sin(\theta(t)) + p_{in} - p_{out}}{R} \quad (4.6)$$

$$\theta(t) = \begin{cases} 0, & t < t_{st} \\ v_t(t - t_{st}), & t_{st} \leq t \leq t_{st} + t_{ed} \\ 60, & t > t_{st} + t_{ed}, \end{cases}$$

where  $\rho$  (g/ml) is the blood density,  $g$  (cm/s<sup>2</sup>) is the gravitational acceleration constant,  $h$  (cm) is the absolute difference in height between the upper and lower body compartments,  $\theta(t)$  is the tilt angle (in radians),  $v_t = 15$  degrees/second is the tilt speed, while  $t_{st}$  and  $t_{ed}$  denote the time at which the tilt begins and finishes, respectively. The hydrostatic pressure between the upper and lower body compartments is incorporated through the term,  $\rho g h \sin(\theta(t))$ , which will be used in the cardiovascular model.

### 4.3 Sensitivity Analysis, Identifiability, and Subset Selection

Given the model described above, understanding the sensitivity of the parameters is important due to their effect on the system output. Parameters for which the model output is insensitive cannot be estimated reliably [25], neither can parameters that are correlated. Parameters that are either insensitive or correlated are not identifiable [5, 6, 8, 14, 26, 41]. The recent study by Kelley and Ipsen [25] also shows that estimates for correlated parameters are not reliable when using the Levenberg-Marquardt algorithm.

#### 4.3.1 Sensitivity Analysis

The sensitivities are classically calculated as

$$S(t; \theta) = \frac{\partial y(t; \theta)}{\partial \theta}, \quad (4.7)$$

where  $y$  is the model output and  $\theta$  denotes the model parameters. The sensitivities are the coefficients of the first order truncation of the Taylor expansion of the observation function, and give a quantitative understanding of how the output will change with respect to a change in the parameter [3]. Considering their function in the calculation of standard errors for parameter estimates, the sensitivities can indicate regions where data provide more information on the parameters and help in determining parameter identifiability [6, 26]. When the system is linear in the parameters, the sensitivities can be calculated analytically; however, when the model is nonlinear, this calculation is carried out by linearizing around current values of the parameter [43]. This dependency on the current value means the sensitivities are a local analysis and will vary based on the initial values of the parameters. This presents challenges due

to the importance of the sensitivities in both determining the identifiability of parameters and in terms of estimating parameters which allow more accurate predictions of the data.

Given a system defined by ordinary differential equations

$$\frac{dx}{dt} = f(t, x; \theta), \quad x(0; \theta) = x_0, \quad (4.8)$$

$$y(t, \theta) = g(t, x(t, \theta); \theta), \quad (4.9)$$

where  $y(t; \theta)$  is the observation function and  $x(t; \theta)$  are the state variables, the sensitivities are calculated by

$$S(t; \theta) = \frac{\partial y}{\partial \theta} = \frac{dg}{dx} \frac{dx}{d\theta} + \frac{dg}{d\theta}. \quad (4.10)$$

The partial derivatives of the observation function are easily calculated, however, the partial derivative of the state equations with respect to the parameters requires the solutions of the ordinary differential equations (4.8). This is obtained by solving the following

$$\frac{d}{dt} \frac{\partial x(t; \theta)}{\partial \theta} = \frac{df(t, x; \theta)}{dx(t; \theta)} \frac{\partial x(t; \theta)}{\partial \theta} + \frac{df(t, x; \theta)}{d\theta}. \quad (4.11)$$

Using the model we derived previously, the sensitivities are calculated and used to rank the parameters from most to least sensitive. The base model during the supine position will be used to calculate the sensitivities. It contains  $n = 12$  parameters,  $\theta = [R_{aup}, R_{al}, R_{vl}, R_{alp}, C_{au}, C_{al}, C_{vl}, C_{vu}, T_R, E_{min}, E_{max}, V_{un, lh}]$ . Given that the model output will only include arterial blood pressure, the sensitivities are calculated as

$$S = \frac{\partial p_{au}}{\partial \tilde{\theta}}, \quad (4.12)$$

where  $\tilde{\theta}$  is the log-scaled parameters. To carry out the sensitivity calculation, we obtain the Jacobians by using a forward difference approximation

$$\begin{aligned} \frac{df}{d\tilde{\theta}_i} &= \frac{f(t, x, \tilde{\theta} + h e_i) - f(t, x, \tilde{\theta})}{h}, \\ \frac{df}{dx_i} &= \frac{f(t, x + h e_i, \tilde{\theta}) - f(t, x, \tilde{\theta})}{h}, \end{aligned}$$

where  $e_i = [0 \dots 0 \overset{i}{1} 0 \dots]^T$  is the unit vector in the  $i$ 'th component direction,  $h = \sqrt{\chi}$  is the step-size, and  $\chi = 10^{-8}$  is the integration tolerance used for the numerical solution of the dynamical system. Using the 2-norm to get the total sensitivity [46], the sensitivities are ranked in Fig 4.2.



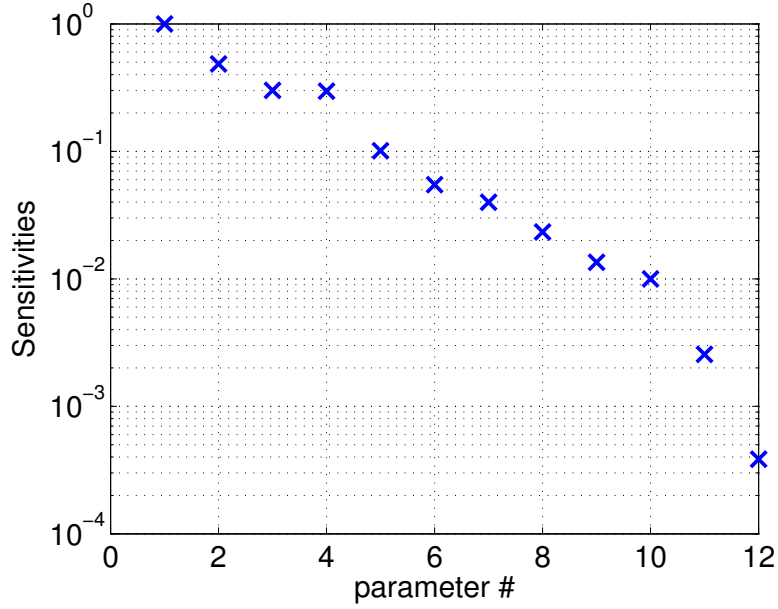


Figure 4.2: Ranked total sensitivities,  $\|\partial p_{au}/\partial \tilde{\theta}\|_2$ , for CV model. Ranked from most to least sensitive. 1:  $E_{max}$  2:  $E_{min}$  3:  $C_{au}$  4:  $R_{aup}$  5:  $R_{vl}$  6:  $C_{al}$  7:  $C_{vu}$  8:  $C_{vl}$  9:  $T_R$  10:  $R_{al}$  11:  $R_{alp}$  12:  $V_{un, lh}$

#### 4.3.2 Subset Selection

A number of methods have been developed which utilize the information provided by the sensitivities to provide a subset of parameters which are identifiable and uncorrelated [5, 6, 8, 14, 26, 41]. The method developed by Burth [5] followed by the method constructed by Olufsen [41] were used to obtain the subset of parameters to be estimated. The first uses a singular value decomposition and QR factorization to identify the subset of parameters. The sensitivity matrix defined in (4.12) is decomposed as  $S(\tilde{\theta}) = U\Sigma V^T$ , where  $\Sigma$  is a diagonal matrix with the singular values of  $S$ . The numerical rank of  $S$ ,  $\rho$ , is used to predict the number of identifiable parameters. Using the tolerance  $\epsilon$ , the numerical rank of  $S$  is the largest  $k$  for which  $\sigma_{n-k+1} > \epsilon\sigma_n$ . For this study,  $\epsilon$  is the square root of the integration tolerance  $\sqrt{\chi}$ . Using  $\rho$ , the matrix of eigenvectors  $V$  can be written as  $[V_\rho V_{n-\rho}]$ . The parameters represented by the  $\rho$  highest eigenvectors are then found using QR-factorization with column pivoting. The subset is finally found by  $V_\rho^T P = QR$ , where  $Q$  is an orthogonal matrix, and the first  $\rho$  elements of  $R$  form an upper triangular matrix with diagonal elements in decreasing order. The permutation matrix  $P$  is used to reorder the parameter vector  $\tilde{\theta} = P^T \tilde{\theta}$ . Lastly, the partition  $\tilde{\theta} = [\tilde{\theta}_\rho, \tilde{\theta}_{n-\rho}]$ , where  $\tilde{\theta}_\rho$  contains the first  $\rho$  sensitive elements, while the  $\tilde{\theta}_{n-\rho}$  contains the parameters that are less sensitive. Using this, we estimate the parameters,  $\tilde{\theta}_\rho$ , while holding the remaining,  $\tilde{\theta}_{n-\rho}$ , at their nominal values. This can lead to bias in the computations, but reduces the variance of the estimates [5]. Estimating more parameters will decrease the bias, but can increase the variance for the parameters; the goal is to balance the bias and variance

allowing minimal prediction error [41].

The other method used to calculate a subset is based upon computing pair-wise correlations. The principle is to exclude correlated parameters from the set to be estimated until no correlation remains [43]. The *correlation matrix*,  $c$ , is used to evaluate the correlations

$$c_{i,j} = \frac{C_{i,j}}{\sqrt{C_{i,i}C_{j,j}}}. \quad (4.13)$$

Here  $c_{i,j}$  describes the degree of correlation between parameter  $i$  and  $j$ , with numeric value between 0 and 1. A parameter pair  $(i, j)$  is considered correlated, iff  $|c_{i,j}| > \gamma$  for  $\gamma \rightarrow 1$ .  $C$  is the correlation matrix, the inverse of the Hessian,  $C = \mathcal{H}^{-1}$ , which is given by  $\mathcal{H} = 1/\sigma^2 S^T S$ . This inversion of the Hessian requires the sensitivity matrix,  $S$ , to be nonsingular. Although no theoretical predictions exist to define a appropriate value for  $\gamma$ , we used  $\gamma = 0.85$  for our analysis [41].

The covariance matrix  $C$  can also be used for the calculation of the standard error [6], defined by

$$s_k = \sqrt{C_{k,k}}, \quad k = 1, \dots, q$$

which is used in the confidence interval calculation, for a given level  $100(1 - \alpha)\%$ , as follows

$$\Theta_{conf,k} = [\theta_k - t_{1-\alpha/2} s_k, \theta_k + t_{1-\alpha/2} s_k]$$

where  $\alpha \in [0, 1]$  and  $t_{1-\frac{\alpha}{2}} \in \mathfrak{R}$  [41]. The critical value  $t_{1-\alpha/2}$  is computed from a student's t-distribution  $t_{K-q,\alpha}$  with  $K - q$  degrees of freedom determined by the probability  $P[T \geq t_{1-\alpha/2}] = \alpha/2$ . When  $K$  is large, the degrees of freedom can be approximate by  $\infty$  and the critical value  $t_{1-\alpha/2} \rightarrow 1.96$ . A confidence interval can be constructed for each possible realization of data of size  $K$  that could be collected, then  $100(1 - \alpha)\%$  of these intervals would contain the true value of the parameter  $\theta_k$  [41]. However, although these confidence intervals can be computed, they are statistically optimistic due to linear approximation of the nonlinear model in the neighborhood of the best parameter estimate [9, 48].

## 4.4 Methods

Optimal parameter values were calculated by William et al [58] for steady state while the patient was in supine position. Using these optimized parameter estimates, sensitivity analysis and subset selection was carried out for the complete model incorporating the tilt dynamics. The purpose is to identify parameters which are sensitive, uncorrelated, and identifiable, and to study parameters which are impacted by autonomic regulation. Using the sensitivities and subset selection, the parameters  $\theta = [R_{aup}, E_{min}]$  are estimated while holding the remaining parameters at their optimized values from steady state. Knowing  $R_{aup}$  and  $E_{min}$  will vary in time due to autonomic regulation, the linear spline methodology is first exam-

ined, along with parameter uncertainty through DRAM, followed by the Kalman filtering methodology.

#### 4.4.1 $R_{aup}$ and $E_{min}$ estimation

The regulation of  $R_{aup}$  and  $E_{min}$  is modeled by defining a set of nodes for each parameter linked through piecewise linear functions of time as developed by Williams [58]. These parameters are defined as  $X(t) = \{R_{aup}(t), E_{min}(t)\}$  and are given by

$$X(t) = \sum_{i=1}^N \gamma_i H_i(t), \quad (4.14)$$

$$H_i(t) = \begin{cases} \frac{t-t_{i-1}}{t_i-t_{i-1}}, & t_{i-1} \leq t \leq t_i \\ \frac{t_{i+1}-t}{t_{i+1}-t_i}, & t_i \leq t \leq t_{i+1} \\ 0, & \text{otherwise,} \end{cases}$$

where the unknown coefficients,  $\gamma_i, i = 1 \dots N$ , are the nodes representing the parameter with  $N$  being the number of nodes along the time span analyzed. These  $N$  nodes were then estimated through nonlinear optimization, and were specified and positioned to properly obtain the parameter dynamics.

#### 4.4.2 Nonlinear Optimization and Parameter Estimation

To estimate the model parameters, we employed nonlinear optimization to minimize the least square error between the model prediction and the measured data. This was done by constructing the residual (4.16), the difference between the model and the measured data, formulated from the observation function which relates the observation to the state. The observation function relies on the assumption that the measurements are described fully by some underlying function of the model plus an error term which represents the measurement noise, defined below

$$y_i^d = h(t_i, x_m(t_i; \theta_\rho, \theta_{n-\rho}), \theta) + \epsilon_i, \quad i = 1, 2, \dots, K \quad (4.15)$$

where  $h$  is the observation function,  $y^d$  are the measured data,  $x_m$  are the model states,  $\theta$  are the parameters,  $\epsilon$  are the measurement noise, and  $K$  is the number of measured data. This definition relies on the assumption that the errors are independent, identically distributed (i.i.d.) random variables with mean  $E[\epsilon_i] = 0$ , covariance  $cov(\epsilon_i, \epsilon_j) = 0$ , and constant variance  $var(\epsilon_i) = \sigma^2$ . Defining the observation

function (4.15) as the arterial blood pressure,  $p_{au}$ , the residuals are constructed as follows

$$R = \frac{1}{\sqrt{K}} \left[ \frac{p_{au,1}^m - p_{au,1}^d}{p_{au,1}^d}, \frac{p_{au,2}^m - p_{au,2}^d}{p_{au,2}^d}, \dots, \frac{p_{au,K}^m - p_{au,K}^d}{p_{au,K}^d} \right], \quad (4.16)$$

where  $p_{au,1}^m$  is the first model prediction and  $p_{au,1}^d$  is the first observed data. Given that only the systolic and diastolic pressure of each cardiac cycle are observed for optimization, the arterial pressures becomes,  $p_{au}^d = [p_{au,1}^{sys}, p_{au,2}^{sys}, \dots, p_{au,K}^{sys}, p_{au,1}^{dia}, p_{au,2}^{dia}, \dots, p_{au,K}^{dia}]$ . Using the residual (4.16), the objective function for optimization is constructed as the sum of squares error given by

$$\bar{\theta}_\rho = \arg \min_{\theta_\rho} J(\theta), \quad (4.17)$$

$$J(\theta) = R^T R = \frac{1}{K} \sum_{i=1}^K \frac{|y^m(t_i; \theta_\rho, \theta_{n-\rho}) - y_i^d|}{y_i^d}, \quad (4.18)$$

where  $y^m$  is the model prediction for  $p_{au}$  and  $y_d$  is the observed measurement of arterial pressure. The scaling by  $y^d$  is done to ensure that all quantities in the output vector are similar in magnitude and equal in weight. As stated previously, the time varying parameters  $[R_{aup}, E_{min}]$  will be estimated while the remaining unidentifiable parameters  $\theta_{n-\rho}$  will be held constant at their nominal values. The time varying parameters were estimated through the linear spline methodology by minimizing the cost function (4.18) using the Levenberg-Marquadt algorithm [29]. The upper and lower bounds for the parameters were set to be a factor of 4 from their nominal values for the optimization algorithm.

#### 4.4.3 Uncertainty Quantification and DRAM

The linear spline method previously described by Williams et al [58] will give an estimate of the parameters, but understanding the variability around those estimates is also important. Understanding the uncertainty and confidence in the estimates is not only important for the parameters specifically, but the system overall. Uncertainty quantification is crucial to obtaining the variability of each estimate, and Markov Chain Monte Carlo is one known method used to calculate this uncertainty.

The purpose of MCMC is to estimate the expectation  $E_\pi[f]$ , where  $f$  is a function with distribution  $\pi$ , by constructing a Markov chain with invariant distribution equivalent to  $\pi$  whose sample path average is used to approximate the expectation of  $\pi$  [19, 52, 53]. More specifically, assuming the Markov chain has  $\pi$  as its unique stationary and limiting distribution, and simulating, the mean of  $f$  along a realization of the sample path of the chain of length  $N$  becomes  $\frac{1}{N} \sum_{i=1}^N f(X_i)$ , where the  $X$ 's are the samples along the chain [19]. However, MCMC has also become increasingly useful as a method to simulate complex,

nonstandard multivariate distributions [7]. There are two central methods for MCMC, the dimension reduction based approach used in Gibbs sampling, and the propose and reject based method used in the Metropolis-Hastings algorithm [22, 36, 53]. We shall focus on the latter for this study due to ease of implementation.

The Metropolis-Hastings (MH) algorithm is built off of the foundation of an accept-reject method. Because we are dealing with a Markov chain, the proposal distribution  $q(x, y)$  from which we generate a new value of the chain is dependent on the current state of the process [7]. For this approach, assuming the process  $X$  is at current value  $x$ , a new value  $Y$  is proposed by sampling from our proposal  $q(x, y)$  and is accepted with probability

$$\alpha(x, y) = \min \left[ \frac{\pi(y)q(y, x)}{\pi(x)q(x, y)}, 1 \right], \quad (4.19)$$

otherwise, the proposed value  $Y$  is rejected and the chain remains at  $x$ . For this algorithm to successfully draw samples from  $\pi$ , two conditions are required to hold, ergodicity and reversibility. By defining the acceptance probability by (4.19), detailed balance is satisfied by the first term within the  $\min$  function which means the chain is reversible [52]. For ergodicity to hold, the chain is required to be irreducible and aperiodic. This means that if  $x$  and  $y$  are in the domain of  $\pi(\cdot)$  then it must be possible to move from  $x$  to a new position  $dy$  in a finite number of iterations, and the number of moves required to move from  $x$  to  $dy$  is not necessarily a multiple of some integer [7]. This is satisfied by a proposal  $q(x, y)$  with positive density on the same support as  $\pi$  or with a restricted support. A number of extensions and strategies have been proposed to improve the efficiency of the resulting MCMC estimators: adaptation [19, 20] and delayed rejection [19, 53].

The first of these enhancements, delayed rejection, is based upon the idea that instead of advancing the iteration and retaining the position of the chain after a MH proposal rejection, a second stage proposal, conditioned on the previous rejection, be computed such that reversibility of the Markov chain is preserved [19]. This process can be extended to a fixed or random number of stages, and can also be used to combine different proposal distributions. Assuming a proposed sample  $Y_1$  from  $q_1(x, y_1)$  was tried and rejected, a second stage proposal  $Y_2$  is generated from  $q_2(x, y_1, y_2)$  depending on the current position and what has been proposed and rejected. This secondary proposal is accepted with probability

$$\beta(x, y_1, y_2) = \quad (4.20)$$

$$\min \left[ \frac{\pi(y_2)q_1(y_2, y_1)(1 - \alpha(y_2, y_1))q_2(y_2, y_1, x)}{\pi(x)q_1(x, y_1)(1 - \alpha(x, y_1))q_2(x, y_1, y_2)}, 1 \right], \quad (4.21)$$

maintaining the Markov chain's reversibility with regards to the invariant distribution  $\pi$ .

The second enhancement is based upon the idea of adapting or tuning the proposal distribution covariance determined by the distribution of the states in the sample path thus far. Assuming Gaussian proposal distribution, the covariance matrix is calibrated using the sample path of the MCMC chain. Because of the adaptation, the covariance now depends on the history of the chain in addition to the

current state, resulting in the stochastic chain no longer being Markovian. However, due to the ergodic properties still maintained, Haario [20] has proved that the adaptive metropolis (AM) chain simulates the target distribution  $\pi$ .

The proposal distribution is adapted by taking the current position of the Markov chain,  $X_n$ , and centering the Gaussian proposal around that position while setting the covariance to be

$$C_n = s_d \text{Cov}(X_0, X_1, \dots, X_{n-1}) + s_d \epsilon I_d \quad (4.22)$$

where  $s_d$  is a parameter that depends only on the dimension  $d$  of the state space on which  $\pi$  is defined,  $\epsilon > 0$  is a constant we choose to be very small, and  $I_d$  denotes an identity matrix of dimension  $d$  [20, 19]. For adaptation, an initial covariance,  $C_0$ , is chosen based upon prior knowledge of the system, and a time index  $n_0 > 0$  is defined as the length of the non-adaptation period which results in the following covariance

$$C_n = \begin{cases} C_0, & n \leq n_0 \\ s_d \text{Cov}(X_0, \dots, X_{n-1}) + s_d \epsilon I_d, & n > n_0. \end{cases} \quad (4.23)$$

Applying the definition of the covariance matrix for a given set of points  $X_0, \dots, X_k \in \mathfrak{R}^d$  obtains

$$\text{Cov}(X_0, \dots, X_k) = \frac{1}{k} \sum_{i=0}^k X_i X_i^T - (k-1) \bar{X}_k \bar{X}_k^T, \quad (4.24)$$

where  $\bar{X}_k = \frac{1}{k+1} \sum_{i=0}^k X_i$  and the elements of  $X_i \in \mathfrak{R}^d$  are arranged such that  $X_i$  is a column vector. Substituting (4.24) into (4.23), we get that, for  $n > n_0$ , the covariance  $C_n$  satisfies the recursive formula

$$C_{n+1} = \frac{n-1}{n} C_n + \frac{s_d}{n} (n \bar{X}_{n-1} \bar{X}_{n-1}^T - (n+1) \bar{X}_n \bar{X}_n^T + X_n X_n^T + \epsilon I_d), \quad (4.25)$$

which allows for a more computationally efficient means to update the covariance matrix since  $\bar{X}_n$  also follows an obvious recursive formula. The choice of  $n_0$  is free, but is used to delay the number of iterations till the adaptation occurs. Haario [20] found that adaptation should not be done at each iteration, but at given intervals. Setting  $n_0$  to be the index that defines the length between the non-adaptation periods improves the mixing properties of the algorithm [19]. The parameter  $\epsilon$  is used to ensure that the covariance,  $C_n$ , does not become singular. For practical purposes, the scaling parameter is set to be  $s_d = 2.4^2/d$  as this optimizes the mixing properties of the MH in cases of Gaussian targets and Gaussian proposals [15].

Combining these strategies and incorporating them into the original Metropolis-Hastings algorithm provides the procedures required for the Delayed-Rejection Adaptive Metropolis Hastings (DRAM) algorithm. More information on the properties and implementation can be found in Haario [19]. Using this, parameter uncertainty was predicted following the procedure outlined in the chemical reactions

problem (example 2) by Haario et al [19].

#### 4.4.4 Nonlinear filter - Ensemble Transform Kalman Filter

The main purpose of this study is to optimally estimate the state of the system, and model parameters  $R_{aup}$  and  $E_{min}$ , given a set of noisy observations. One method to accomplish this has already been discussed, but an alternate method is the Kalman filter [27]. The ensemble transform Kalman filter is used due to its utility in solving complex and challenging problems, explicitly cardiovascular based systems as detailed in chapter 2 [35].

### 4.5 Results

Using the five compartment cardiovascular model, results were obtained for the HUT dynamics by accounting for the hydrostatic pooling of blood in the legs by enacting controls through the application of piecewise linear spline functions defined in (4.14). Holding the unidentifiable parameters at their nominal values, the remaining  $\rho$  identifiable parameters are discretized as  $\theta_\rho = [\gamma_i, R_{aup}, \gamma_i, E_{min}]$  and approximated with nodes,  $N = 33$ , spaced out across the time domain. Using the initial conditions for the states and nodes, given below, we minimize the cost function (4.18) using the Levenberg-Marquardt method [29],

$$\begin{pmatrix} p_{au0} \\ p_{al0} \\ p_{vl0} \\ p_{vu0} \\ V_{lh0} \end{pmatrix} = \begin{pmatrix} 67.71 \\ 3.5 \\ 66.35 \\ 3.75 \\ 60 \end{pmatrix}, \quad \begin{pmatrix} R_{aup0} \\ E_{min0} \end{pmatrix} = \begin{pmatrix} 0 \\ 0 \end{pmatrix}.$$

Figure 4.3 shows the diastolic and systolic arterial blood pressure data along with the model fit for  $p_{au}$ . The plot gives an overview of the model fit to the diastolic and systolic pressure data with a qualitative focus on the HUT dynamics. The subplot displays the histogram of the residuals for the NLS fit overlaid with the theoretical Gaussian distribution.

The time varying parameters,  $R_{aup}$  and  $E_{min}$ , obtained by minimizing the least squared error (4.18) using the residual (4.16) are depicted in Figure 4.6 and Figure 4.7, respectively. Using the NLS results, a DRAM run was used to obtain a better understanding of the uncertainty of each estimate over the time scale. The DRAM routine was run for 2000 samples with a burn-in of 300 samples. Each plot shows the mean, taken to be the NLS estimates for each node in the linear piecewise spline, along with first and second standard deviation intervals calculated using the DRAM methodology. Along with the NLS estimates and the confidence intervals, the figures also present the estimates of  $R_{aup}$  and  $E_{min}$  obtained

using the Ensemble Transform Kalman filter using the initial conditions provided below

$$\begin{pmatrix} p_{au0} \\ p_{al0} \\ p_{vl0} \\ p_{vu0} \\ V_{lh0} \end{pmatrix} = \begin{pmatrix} 67.7088 \\ 3.5 \\ 66.3546 \\ 3.75 \\ 60 \end{pmatrix}, Q = \begin{pmatrix} 0.5 & 0 & 0 & 0 & 0 \\ 0 & 0.0001 & 0 & 0 & 0 \\ 0 & 0 & 0.05 & 0 & 0 \\ 0 & 0 & 0 & 0.1 & 0 \\ 0 & 0 & 0 & 0 & 0.05 \end{pmatrix},$$

$$R = 0.1, Q_{R_{aup}, E_{min}} = \begin{pmatrix} 1e-6 & 0 \\ 0 & 1e-6 \end{pmatrix},$$

with  $P_{x_0} = 1e^{-6}I$  and  $P_{q_0} = 1e^{-8}I$ , where  $I$  is the identity matrix. The confidence intervals, two standard deviations, for the filter are also presented as the dashed red lines. Figure 4.3 displays the diastolic and systolic blood pressure data along with the model fit utilizing the ETKF for  $p_{au}$ . The subplot again depicts the histogram of residuals from the filter fit overlaid with the theoretical Gaussian distribution. As the filter estimates the distributions in real time, a better understanding of the fit can be viewed in the absolute value of the residuals over the time interval seen in Figure 4.5. Reviewing the plot, we would expect approximately 95% of the data to be within  $2\sigma$ . Over the time course of the experiment, 413 observations were collected. Of these, 31 were outside of the  $2\sigma$  interval resulting in 92.5% being within the calculated filter confidence interval. Although this metric gives us a theoretical understanding of the filters accuracy in prediction, it can be seen that a large number of the points outside of the interval are between the  $t = [80, 100]$  interval when the tilt occurs. This interval is where the greatest changes are occurring due to effects of gravity and the body's regulation of the physiological processes. Table 4.2 gives a quantitative overview of the two methods fit to the pressure data.

Table 4.2: Results of ETKF vs. NLS for blood pressure

	NLS	ETKF
RMSE	1.9658	0.7414
$\sigma_{residual}^2$	3.8583	0.5508
$J_{cost}$	3.8642	0.5497

Further validation and evaluation can be gathered by examining the dynamics of the unobserved states. As no data is available for those states, only the qualitative behavior and average values can be assessed. Figure 4.4 depicts the filter dynamics for the lower body arterial pressure  $p_{al}$ , venous pressure  $p_{vl}$ , upper body venous pressure  $p_{vu}$  and the volume of the left ventricle  $V_{lh}$ . As the tilt occurs, the effect of gravity results in an increase in pressure to the lower extremities as the blood pools for both the arterial and venous compartments. This same process causes a decrease of pressure in the upper body



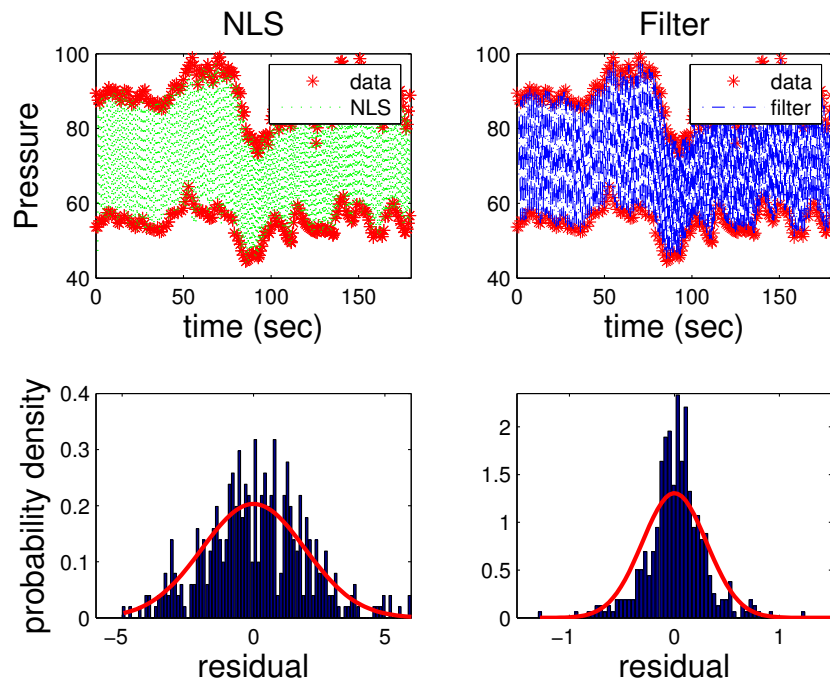


Figure 4.3: Plot of Nonlinear Least Squares and Ensemble Transform Kalman Filter fit to Pressure data,  $p_{au}$ , and Residual distributions.

which results in less blood returning to the heart and therefore a smaller volume. The dynamics of the unobserved states match these assertions.

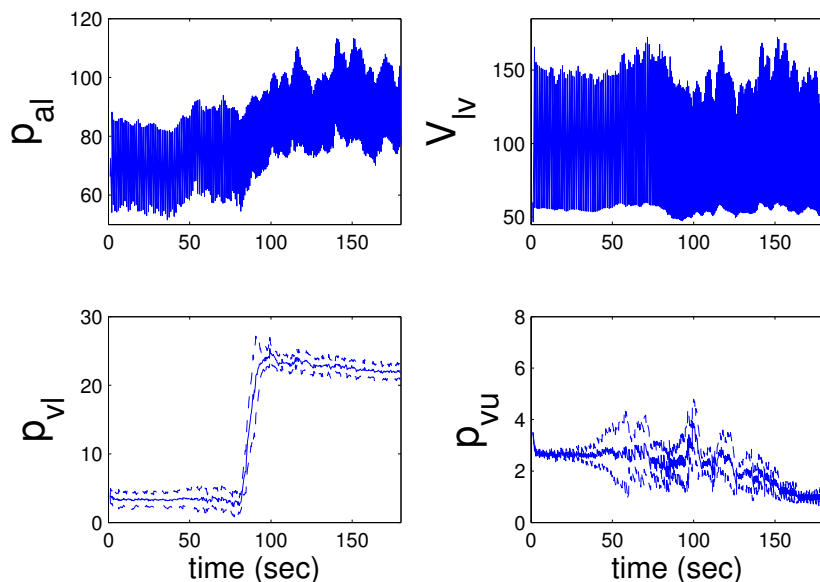


Figure 4.4: Plots of ETKF results of unobserved states as described; upper left:  $p_{al}$ , lower left:  $p_{vl}$ , upper right:  $V_{lv}$ , lower right:  $p_{vu}$ .

## 4.6 Discussion and Conclusion

The focus of this work was to better understand the cardiovascular regulation during HUT. This was accomplished by constructing a simple five compartment lumped model built using basic physiological principles and modeling the  $\rho$  identifiable parameters;  $R_{aup}$  and  $E_{min}$ ; as time varying parameters using both the linear spline approach which utilized nonlinear optimization to minimize the residual, and the Ensemble Transform Kalman filter methodology. Performing model analysis through sensitivity analysis and subset selection, these parameters were selected due to being sensitive and non-correlated, but also because of their significance in terms of autonomic response to HUT.

In response to performing the tilt, peripheral resistance immediately drops (Figure 4.6). This could be a result of changes in hydrostatic pressure in the lower compartments or due to activation of skeletal muscle [51, 57]; however, as the tilt is performed in a relaxed environment, muscle action should not be activated during the procedure and therefore changes in hydrostatic pressure is likely the reason. After the initial drop in resistance, a rebound occurs due to contraction of smooth muscles in the

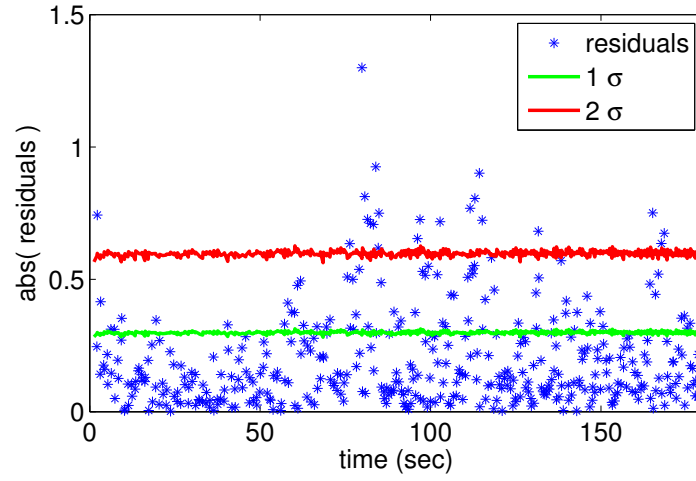


Figure 4.5: Absolute value of residuals with  $\sigma$  and  $2\sigma$  from the filter fit for  $p_{au}$ . Assuming the residuals are normally distributed, 68% of the data should fall under the  $1\sigma$  line while 95% should fall under the  $2\sigma$  line.

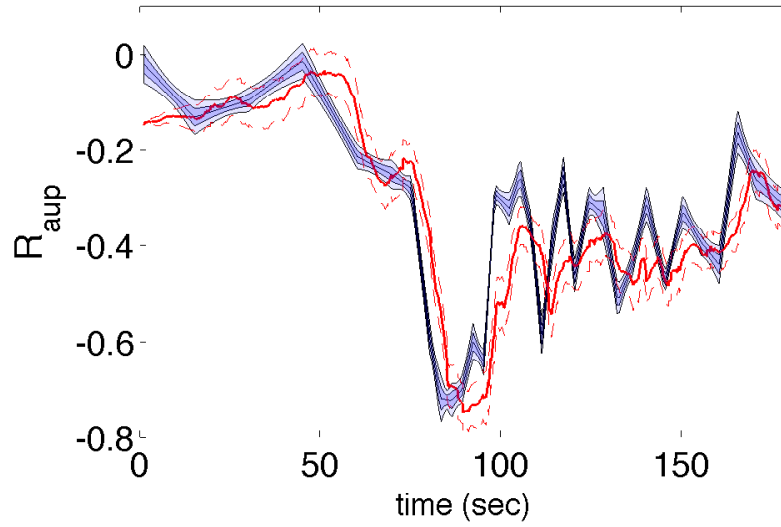


Figure 4.6: NLS estimate for  $R_{aup}$  along with confidence bounds derived through DRAM compared to ETKF estimate for  $R_{aup}$  with confidence intervals in log scale.

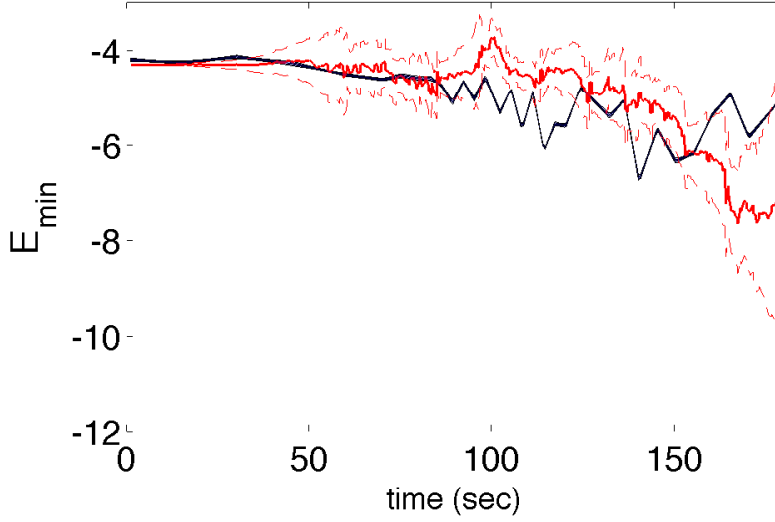


Figure 4.7: NLS estimate for  $E_{min}$  along with confidence bounds derived through DRAM compared to ETKF estimate for  $E_{min}$  with confidence intervals in log scale.

muscular and elastic arteries, respectively, while also increasing nerve traffic through parasympathetic withdrawal along with sympathetic efferent nerve excitation [58]. This sympathetic activation also has a positive inotropic effect on the heart which decreases the left ventricle's elastance (Figure 4.7) allowing the heart to increase preload volume and therefore, cardiac output. The drop in blood volume observed, Figure 4.4, immediately following the tilt coincides with results seen in previous studies; Smith et al [50] and Matzen et al [34] reported a 25% reduction in ventricular blood volume while Enish et al [11] and Lieshout et al [31] reported a decrease in stroke volume following HUT [58]. This decrease in left ventricular volume is an immediate consequence of the decrease of filling pressure, which concurs with experimental results [11]. The lower compartment venous pressure ( $p_{vl}$ ) increases as a result of the gravitational pooling of blood, which agrees with previous findings [17], while the upper venous pressure ( $p_{uv}$ ) also simultaneously drops, as reported in literature [21, 31].

Using the general NLS framework, we expect observations to be of the form (4.15) with the assumption that errors will be Gaussian due to the central limit theorem. Comparing the NLS and filter residuals distributions, the filter does a better job to explain the variation in pressure by minimizing the residual variance. The differences in these residual distributions and fits are described quantitatively by reviewing Table 4.2. Although the filter is also assuming Gaussian distributions for both the measurement error and model error, the filter can better represent the residual distribution because it can take the model error into account. This accounts for error that would be associated with the measurements otherwise, inappropriately, and can cause bias to the estimates. More specifically, this study is using a model which simplifies the cardiovascular system into 5 lumped compartments. This is being used

to explain the underlying physiological processes without explicitly accounting for such features as the sympathetic or parasympathetic nervous system. The filter exhibits a better fit and methodology because the processes that are not well understood, or incorporated into the model, can be accounted for through the model error of the filter. This will appropriately relegate the error of the different components of the model to their respective states.

Reviewing the estimates for  $R_{aup}$  for both the filter and linear spline in Figure 4.6, the qualitative features are consistent for both methods. Although discrepancies are visible between the two methods in terms of general dynamics, the linear spline method is discretizing the time domain up and approximating the dynamics through the optimization of each node. Since this is not continuous like the filter, the linear spline can only approximate the dynamics where the nodes are positioned. In this case, the filter shows the maximum value for the  $R_{aup}$  around  $t = 60$ , while the linear spline positioned this maximum at  $t = 45$  as that is where the closest node was positioned. This feature allows the filter to give more accurate estimates of where the dynamics occur temporally since it does not rely on discretization. This also becomes a statistical issue as if we want to further capture the dynamics using more nodes, we are intrinsically decreasing the degrees of freedom with each addition node and expecting a better fit. This gives rise to model selection issues in terms of optimal number of nodes for each parameter. Comparing the confidence intervals for each method, they appear consistent for both methods over the time frame.

Figure 4.7 gives an overview of the fits for  $E_{min}$  using both the linear spline and ETKF. Before the HUT ( $t = 80$ ), both methods are consistent in predicting little to no change to the estimate. Once the HUT occurs, the methods display differences in their estimate of the minimum ventricular elastance,  $E_{min}$ . The filter has an increase in the confidence of the estimate over this time and ends with a lower estimate than the spline and larger confidence, encapsulating the spline estimate within the confidence bounds. The differences in the estimate and the confidence of these methods shows how the incorporation of modeling error into the system can have an effect on our perceived dynamics. The spline shows less variation overall and greater confidence in the estimate due to the assumptions that all the error in the fit is solely due to the observations. This leads to a higher confidence in the estimate and less deviation of the estimate over the time scale. However, when this assumption does not hold, the filter more appropriately captures the parameter dynamics, and uncertainty in those estimates.

While other studies have been proposed to predict blood pressure regulation [24, 40], we utilized a simplified, five compartment model derived by Williams et al. [58] to better understand the body's response to orthostatic stress during head-up tilt. By using arterial pressure data, utilizing parameter estimation to fit our model, and capturing the dynamics of resistance and elastance, we obtain a better understanding of the interplay between the cardiovascular system and autonomic activation. Utilizing both linear spline optimization and Kalman filtering, we highlight the benefits of Kalman filtering through the estimation of  $R_{aup}$  and  $E_{min}$  and the uncertainty associated with those parameters. Due to the nature of biological modeling in general, and cardiovascular modeling specifically, simplifications are often implemented due to the complexity of the systems. Kalman filtering presents a methodology

to account for the errors inherent to these model simplifications. While the current study only presented analysis for a single subject, the results show that the model and methodology can be used for larger, varying groups of subjects. Future work should consider estimation for more subjects or utilization of a nonlinear mixed effects engine to estimate the variability among a population. Also, to have a better understanding of the model misspecification, the filter can be incorporated into optimization and the model noise can become parameters which can also be estimated.

## REFERENCES

- [1] Bishop, C.H., Etherton, B.J., and Majumdar, S.J. "Adaptive Sampling with the Ensemble Transform Kalman Filter. Part I: Theoretical Aspects." Monthly Weather Review. Vol. 129, 2001, Pgs. 420-436.
- [2] Batzel, J.J., Kappel F., Schneditz, D., and Tran, H.T. Cardiovascular and respiratory systems. Modeling, analysis and control. Philadelphia, PA: SIAM, 2007.
- [3] Bortz, D.M. and Nelson, P.W. "Sensitivity Analysis of a Nonlinear Lumped Parameter Model of HIV Infection Dynamics." Bulletin of Mathematical Biology. Vol. 66, 2004, Pgs. 1009-1026.
- [4] Bugenhagen, S., Cowley, A., and Beard, D. "Identifying physiological origins of baroreflex dysfunction in salt-sensitive hypertension in the Dahl SS rat." Physiological Genomics. Vol. 42, 2010, Pgs 23-41.
- [5] Burth, M., Berghese, G. C., and Velez-Reyes, M. "Subsect Selection for Improved Parameter Estimation in On-Line Identification of a Synchronous Generator." IEEE Transactions on Power Systems. Vol. 14, No. 1, 1999, Pgs. 218-225.
- [6] Capaldi, A., Behrend, S., Berman, B., Smith, J., Wright, J., and Lloyd, A. "Parameter Estimation and Uncertainty Quantification for an Epidemic Model." Mathematical Biosciences and Engineering. Vol. 9, No. 3, 2012, Pgs. 553-576.
- [7] Chib, S. and Greenberg, E. "Understanding the Metropolis-Hastings Algorithm." The American Statistician. Vol. 49, No. 4, 1995, Pgs. 327-335.
- [8] Cintron-Arias, A., Banks, H.T., Capaldi, A., and Lloyd, A. "A sensitivity matrix based methodology for inverse problem formulation." Journal of Inverse and Ill-posed Problem. Vol. 17, No. 6, Pgs. 545-564.
- [9] Dochain, D. and Vanrolleghem, P.A. Dynamical modeling and estimation in wastewater treatment processes. IWA Publishing, London. 2001.

- [10] Ellwein, L.M. Cardiovascular and Respiratory Regulation, Modeling and Parameter Estimation. PhD thesis, North Carolina State University, 2008.
- [11] Enishi, K., Tajima, F., Akimoto, H., and Mita, R. "Initial Drop of Blood Pressure during Head-up Tilt in Patients with Cerebrovascular Accidents." Environmental Health and Preventative Medicine. Vol. 9, 2004, Pgs. 228-233.
- [12] Evensen, G. Data Assimilation: The Ensemble Kalman Filter. New York: Springer, 2009.
- [13] Evensen, G. "The Ensemble Kalman Filter: Theoretical Formulation and Practical Implementation." Ocean Dynamics. Vol. 54, 2003. Pgs. 539-560.
- [14] Fink, M., Attarian, A., and Tran, H. "Subset Selection for Parameter Estimation in an HIV Model." PAMM. Vol. 7, No. 1, Pgs. 1121501-1121502.
- [15] Gelman, A.G., Roberts, G.O., and Gilks, W.R. "Efficient Metropolis jumping rules." in: Bernardo, J.M., Berger, J.O., David, A.F., and Smith, A.F.M. (Eds.), Bayesian Statistics. V. Oxford University Press, Pgs. 599-608.
- [16] Grimmett, G. and Stirzaker, D. Probability and Random Processes. New York: Oxford University Press, 2001.
- [17] Groothuis, J., Poelkens, F., Wouters, C., Kooijman, M., and Hopman, M. "Leg intravenous pressure during head-up tilt." Journal of Applied Physiology. Vol. 105, 2008, Pgs. 811-815
- [18] Guyton, A.C. and Hall, J.E. Textbook of Medical Physiology. W.B. Saunders Company, Philadelphia, PA, 9th edition, 1996.
- [19] Haario, H., Laine, M., and Mira, A. "DRAM: Efficient adaptive MCMC." Statistics and Computing. Vol. 16, 2006, Pgs. 339-354.
- [20] Haario, H., Saksman, E., Tamminen, J. "An adaptive Metropolis Algorithm." Bernoulli. Vol. 7, No. 2, 2001, Pgs. 223-242.



- [21] Harms, M., Van Lieshout, J., Jenstrup, M., Pott, F., and Secher, N. "Postural effects on cardiac output and mixed venous oxygen saturation in humans." Experimental Physiology. Vol. 88, No. 5, 2004, pgs. 611-616.
- [22] Hastings, W.K. "Monte Carlo Sampling Methods Using Markov Chains and Their Applications." Biometrika Trust. Vol. 57, No. 1, 1970, Pgs. 97-109.
- [23] Haykin, S. Kalman Filtering and Neural Networks. New York: John Wiley and Sons, Inc., 2001.
- [24] Heldt T., Shim, E.B., Kamm, R.D., and Mark, R.G. "Computational modeling of cardiovascular response to orthostatic Stress." Journal of Applied Physiology. Vol. 92, 2002, Pgs. 1239-1254.
- [25] Ipsen, I.C.F., Kelley, C.T., and Pope, S.R. "Rank-deficient nonlinear least squares problems and subset selection". SIAM J Numer Anal., Vol. 49, 2011, Pgs. 1244-1266.
- [26] Jacquez, J.A. and Greif, P. "Numerical Parameter identifiability and estimability: Integrating identifiability, estimability, and optimal sampling design." Mathematical Biosciences. Vol. 77, No. 1, 1985, Pgs. 201-227.
- [27] Kalman, R. E. "A New Approach to Linear Filtering and Prediction Problems." ASME J. Basic Engineering. Vol. 82, 1960, Pgs. 34-45.
- [28] Kappel, F. and Peer, R.O. "A mathematical model for fundamental regulation processes in the cardiovascular system." J. Math. Biol., Vol. 31, 1993, Pgs. 611-631.
- [29] Kelley, C.T. Iterative Methods for Optimization. SIAM, Philadelphia, PA, 1999.
- [30] Lanier, J.B., Mote, M.B., and Clay, E.C. "Evaluation and Management of orthostatic hypertension." American Family Physician. Vol. 84, 2011, Pgs. 527-536.
- [31] Lieshout, J., Harms, M., Porr, F., Jenstrup, M., and Secher, N. "Stroke Volume of the heart and thoracic fluid content during head-up and head-down tilt in humans." Acta anaesthesiologica scandinavica. vol. 49, 2005, Pgs. 1287-1292

- [32] Mahdi, A., Sturdy, J., Ottesen, J.T., Olufsen, M.S. "Modeling the afferent dynamics of the baroreflex control system"." PLoS Comp Biol, DOI:10.1371/journal.pcbi.1003384, Dec 2013.
- [33] Majda, A.J. and Harlim, J. Filtering turbulent complex systems Cambridge University Press., UK, 2012.
- [34] Matzen, S., Perko, G., Groth, S., Friedman, D.B., and Secher, N.H. "Blood volume distribution during head-up tilt induced central hypovolaemia in man." Clinical Physiology. Vol. 11, 1991, Pgs. 411-422.
- [35] Matzuka, B., Aoi, M., Attarian, A., and Tran, H. "Nonlinear Filtering Methodologies For Parameter Estimation." *submitted: Mathematical Biosciences and Engineering*. 2012.
- [36] Metropolis, N., Rosenbluth, A.W., Rosenbluth, M.N., and Teller, A.H. "Equation of State Calculations by Fast Computing Machines." Journal of Chemical Physics. Vol. 21, No. 6, 1953, Pgs. 1087-1092.
- [37] Miao, H., Xia X., Perelson, A.S., and Wu H. "On identifiability on nonlinear ODE models and applications in viral dynamics", SIAM Rev, Vol. 53, 2011, Pgs. 3-39.
- [38] Miller, T.H. and Kruse, J.E. "Evaluation of Syncope." American Family Physician. Vol. 72, 2005, Pgs. 1492-1500.
- [39] Olufsen, M.S., Ottesen, J.T., Tran, H.T., Ellwein, L.M., Lipsitz, L.A., and Novak, V. "Blood Pressure and Blood Flow Variation During Postural Change from Sitting to Standing: Model Development and Validation." Journal of Applied Physiology. Vol. 99, 2005, Pgs. 1523-1537.
- [40] Olufsen, M., Ottesen, J., Tran, H., Ellwein, L., Lipsitz, L., and Novak, V. "Blood pressure and blood flow variation during postural change from sitting to standing: model development and validation." Journal of Applied Physiology. Vol. 99, 2005, Pgs. 1523-1537.
- [41] Olufsen, M.S. and Ottesen, J.T. "A Practical approach to parameter estimation applied to model predicting heart rate regulation." Journal of Mathematical Biology. 2012.

- [42] Olufsen, M.S., Tran, H.T., Ottesen, J.T., REU Program, Lipsitz, L.A., and Novak, V. "Modeling baroreflex regulation of heart rate during orthostatic stress", Am J Physiol. Vol. 291, 2006, Pgs. R1355-R1368.
- [43] Olsen, C.H., Mehlsen, J., Ottesen, J.T., Tran, H.T., and Olufsen, M. "Global Sensitivity and Identifiability Analysis Applied to a Model Predicting Baroreflex Regulation During Head-Up Tilt." International Workshop on Innovative Simulation for Healthcare. 2012, Pgs. 81-86.
- [44] Ottesen, J.T. and Olufsen, M.S. "Functionality of the baroreceptor nerves in heart rate regulation." Comp Meth Prog Biomed. Vol. 101, 2011, Pgs. 208-219.
- [45] Ottesen, J., and Danielsen, M. "Modeling Ventricular contraction with heart rate changes." Journal of Theoretical Biology. Vol. 222, 2003, Pgs. 337-346.
- [46] Pope, S.R., Ellwein, L.M., Zapata, C.L., Novak, V., Kelley, C.T., and Olufsen, M.S. "Estimation and identification of parameters in a lumped cerebrovascular model." Mathematical Biosciences and Engineering. Vol. 6, 2009, Pgs. 93-115.
- [47] Robertson, D.W., Low, P.A., and Polinsky, R.J. Primer on the Autonomic Nervous System. Academic Press, San Diego, CA, 2nd edition, 2004.
- [48] Rodriguez-Fernandez, M., Egea, J.A., Banga, J.R. "Novel metaheuristic for parameter estimation in nonlinear dynamic biological systems." BMC Bioinformatics. Vol. 7, No. 483, 2006, Pgs. 1-18.
- [49] Segers, S., Qasem, A., Backer, T., Carlier, S., Verdonck, P., and Avolio, A. "Peripheral Oscillatory Compliance is Associated with Aortic Augmentation Index." Hypertension. Vol. 37, 2001, Pgs. 1434-1439.
- [50] Smith, J.J. and Ebert, J. General response to orthostatic stress. CRC Press, Boca Raton, FL, 1990.
- [51] Sprangers, R., Wesseling, K., Imholz, A., Imholz, B., and Wieling, W. "Initial Blood pressure fall on stand up and exercise explained by changes in total peripheral resistance." Journal of applied physiology. Vol. 70, 1991, Pgs. 523-530.

- [52] Stirzaker, D. Elementary Probability. New York: Cambridge University Press, 2003.
- [53] Tierney, L. and Mira, A. "Some Adaptive Monte Carlo Methods for Bayesian Inference." Statistics in Medicine. Vol. 18, 1999, Pgs. 2507-2515.
- [54] Triedman, J. and Paul, J. "Blood pressure modulation by central venous pressure and respiration. Buffering effects of the heart rate reflexes." Circulation. Vol. 89, 1994, Pgs. 169-179.
- [55] Ursino, M. and Magosso, E. "Role of short-term cardiovascular regulation in heart period variability: a modeling study ." Am J Physiol Vol. 284, 2001, Pgs. H479-H1493.
- [56] Velez-Reyes, M. and Verghese, G.C. "Subset Selection in Identification and Application to Speed and Parameter Estimation for Induction Machines." Proceedings of the 4th IEEE Conference on Control Applications. 1995, Pgs. 991-997.
- [57] Wieling, W., Harms, M., Harkel, A., van Lieshout, J., and Sprangers, R. "Circulatory response evoked by a 3 s bout of dynamic leg exercise in humans." Journal of Physiology. Vol. 494, No. 2, 1996, Pgs. 601-611.
- [58] Williams, N.D., Wind-Willassen, Ø., Mehlsen, J., Ottesen, J.T., and Olufsen, M.S. "Patient Specific Modeling of Head-Up Tilt." Mathematical Medicine and Biology. 2013, Pgs. 1-28.

## Chapter 5

# Pharmacokinetics and Pharmacodynamics

The previous chapter highlighted the benefits of using nonlinear filtering techniques in modeling using a single subject, and alluded to the potential benefit in utilizing its application in larger, varying groups of subjects. This chapter presents the background for pharmacokinetics and pharmacodynamics, fields associated with quantifying the properties of drugs and their effects within populations. The main concepts presented in this chapter come from Gabrielsson and Weiner [3] and Riviere [4].

In general, pharmacokinetics is used to understand how the body affects the drug, while pharmacodynamics is how the drug affects the body.

### 5.1 Pharmacokinetics

Pharmacokinetics (PK) is best defined as the study of absorption, distribution, and elimination of drugs within the body [1, 4]. More specifically, the study of the time course of drug concentration disposition through the different body spaces such as plasma, blood, urine, cerebrospinal fluid, and tissues. A drug can be administered to the body any number of ways including intravenous (IV), intramuscular (IM), subcutaneous (SC), oral (PO), topical (TOP), and inhalation (IN). Upon administration, the drug undergoes absorption, which is defined as the process in which the drug moves into the bloodstream. Based upon the dosage applied and the method administered, the time course and the amount absorbed can vary significantly (intravenous vs. oral). The primary quantity of interest is the concentration of free, nonprotein-bound drug dissolved in the blood because this is the fluid that carries the drug throughout the body from which samples for drug analysis can be readily and repeatedly collected. For the majority of drugs, the concentration in the systemic circulation is in equilibrium with the extracellular fluid of well-perfused tissues; therefore, the plasma drug concentration in systemic circulation generally reflects the extracellular drug concentration. A drug must generally be present at its site of action in a tissue at

a sufficient concentration for a sufficient period of time to produce the intended pharmacological effect [4]. Figure 5.1 illustrates the process a drug undergoes to create an effect, including administration, absorption, distribution, and elimination.

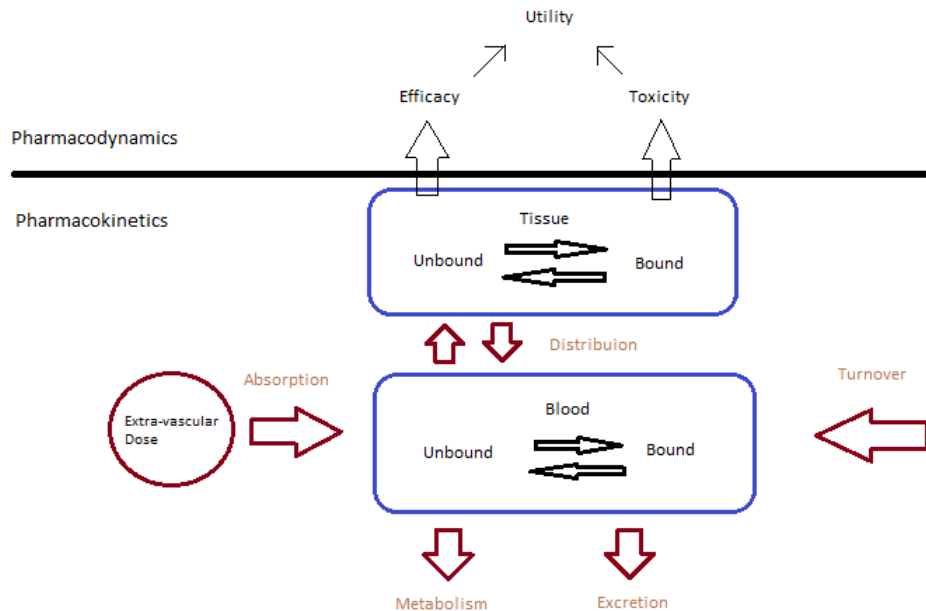


Figure 5.1: Schematic representation illustrating the interplay between absorption, distribution, binding, and elimination (excretion and metabolism) kinetics as well as dynamics of a drug.

For a drug to have its effect, it must reach its targeted site of action in its intended molecular form. To do so, the drug must be transported through a number of boundaries and barriers to distribute to its targeted location. Membrane barriers, and the resistance they offer to drug movement, often define the modeling structure utilized for pharmacokinetic analysis [4]. Biological spaces are defined by the functionality of these barriers. The most effective barriers such as the skin or areas of the gastrointestinal or respiratory tracts protect the organ from the external environment. Upon traversing the protective membranes, the drug will enter the interstitial fluid compartment before entering the blood stream through the absorption process. After leaving the plasma compartment and traveling into the target tissue, again the drug will encounter the interstitial fluid compartment before passing through the target cell membrane and into the intracellular fluid to arrive at the intended cellular organelle target; a simplified depiction of this process is displayed in Figure 5.2.

The compositions of the membranes governs the type of transport required for the drug to traverse the boundaries. A basic model for a cellular membrane was proposed by Davson and Danielli [2] and

postulates that the membrane is a heterogenous composition of varying lipids along with proteins, which help stabilize the membrane. The location of the proteins within the lipid matrix is primarily a consequence of their hydrophobicity and hydrophilicity. Evidence indicates that lipid-based membranes are permeable to non-polar lipid soluble compounds and polar water-soluble compounds with sufficient lipid solubility [4]. These will diffuse through the hydrophobic lipid regions of the membrane. The rate of this diffusion will be proportional to the concentration gradient across the membrane and can be quantified by Fick's law of diffusion

$$\text{Rate of Diffusion}(mg/s) = \frac{D(cm/s)P}{h(cm)}(X_1 - X_2)(mg), \quad (5.1)$$

where  $D$  is the diffusion coefficient for the specific penetrant,  $P$  is the partition coefficient of the penetrant between the membrane and the external medium,  $h$  is the membrane thickness, and  $X_1 - X_2$  is the concentration gradient across the membrane.

Another variable that affects the diffusion across membranes is the pH. Nonionized weak organic acids and bases are more permeable than ionized acids and bases. The amount of drug in the ionized versus nonionized form is directly related to the  $pK_a$  (negative logarithm of the acidic dissociation constant) of the drug and the pH of the medium on both sides of the membrane. It is the nonionized drug that is governed by Fick's law and easily able to diffuse. The ratio of ionized to nonionized drug is given by the Henderson-Hasselbalch equation:

For acids:

$$pK_a - pH = \log[(HAcid)^o / (Acid)^-]. \quad (5.2)$$

For bases:

$$pK_a - pH = \log[(HBase)^+ / (Base)^o]. \quad (5.3)$$

The equations are identical as they involve the ratio of protonated to non-protonated moieties. The only difference is that for an acid, the protonated form  $(HAcid)^o$  is neutral, while, for a base the protonated form  $(HBase)^+$  is ionized.

While passive diffusion is the usual route of transmembrane permeation for non-polar, small molecules, there are other mechanisms by which substances can pass a membrane barrier. One example is protein carrier-mediated active transport. In the case of active transport, the carrier protein binds to the drug and carries it against the concentration gradient, allowing entry of hydrophilic or charged compounds which normally cannot cross the membrane through passive diffusion. Also, unlike diffusion, the rate of transport is saturable if the proportion of mediators to amount of drug is small; thus, it is no longer concentration dependent. Other examples of transport are pores which only allow relatively small molecules to pass through independent of lipid solubility, through dissolution in water thereby traveling where the water goes, and through endocytosis by which the compound binds to the surface of the membrane, the membrane invaginates the compound, and interiorizes the compound through a

number of mechanisms.

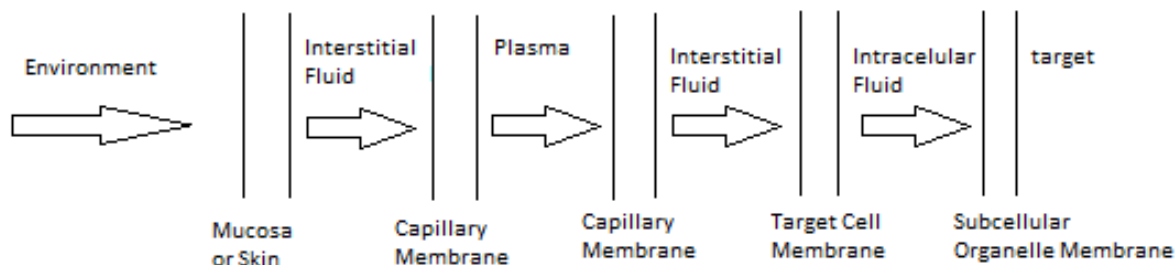


Figure 5.2: Illustration of the absorption, distribution, and transport of a drug through the various barriers and membranes to its target.

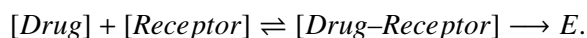
## 5.2 Pharmacodynamics

While this thesis will not address pharmacodynamic modeling, this section is included for completeness.

Once a drug reaches its site of action, the drug binds to a receptor at that site to cause an effect. Pharmacodynamics can be defined as the study of the time course of the biological effect of drugs, the relationship between the effect and drug exposure, and the drug blood concentration and drug response [3].

Pharmacodynamics concerns the interplay of drug-receptor binding. Receptors are the macromolecules that are associated with chemical signaling within and between cells. Agonists are ligands that bind to a certain receptor, thereby increasing the proportion in an active form, and activate a biological response. Antagonists are compounds that reduce the action of another compound by deactivating or diminishing the biological response. The amount of activity of a compound, either in terms of concentration or amount needed to cause a desired effect, defines the potency. Generally, the main interest of pharmacodynamics is the efficacy of a drug, defined as the degree to which agonists produce varying responses, even when occupying the same proportion of receptors [3]. Typically, ligands are competing for receptors and the ligand with the highest affinity will bind.

The law of mass action is often used to describe receptor occupancy and the most applicable receptor occupancy model is below





Assuming response is proportional to the number of receptors occupied at a particular time, models are then constructed to quantify important features. Typically, the maximal drug induced response  $E_{max}$ , the baseline effect,  $E_0$ , and the plasma concentration corresponding to the half-maximal difference between the baseline and maximal response  $EC_{50}$  describe the efficacy. Using modeling to understand the concentration to response relationship, these parameters can be quantified to elucidate the dose-response profile.

## REFERENCES

- [1] Aarons, L. "Pharmacokinetic and pharmacodynamic modelling in drug development." Statistical Methods in Medical Research. Vol. 8, No. 3, 1999, Pgs. 181-182.
- [2] Davson, H., and Danielli, J.F. Permeability of Natural Membranes, 2nd edition. London, UK: Cambridge University Press, 1952.
- [3] Gabrielsson, J. and Weiner, D. Pharmacokinetic and Pharmacodynamic Data Analysis: Concepts and Applications Stockholm, Sweden: Swedish Pharmaceutical Press, 2006.
- [4] Riviere, J. Comparative Pharmacokinetics Principles, Techniques, and Applications. West Sussex, UK: John Wiley, and Sons, 2011.
- [5] Sheiner, L.B. and Steimer, J.L. "Pharmacokinetic/Pharmacodynamic Modeling in Drug Development." Annual Review of Pharmacology and Toxicology. Vol. 40, 2000, Pgs. 67-95.

## Chapter 6

# Stochastic Nonlinear Mixed Effects - A Metformin Case Study

### 6.1 Introduction

Nonlinear mixed effects modelling is a common and powerful methodology for analyzing repeated measures to characterize the pharmacokinetic (PK) and pharmacodynamic (PD) properties of a drug [1, 22, 23, 26]. Within this modeling framework, the variability is decomposed into inter-individual and intra-individual variability. The inter-individual variability accounts for factors that facilitate heterogeneity of subjects within the population. The intra-individual (residual) variability is not only associated with the errors due to measurement collection such as assay sensitivity, dosing, and sampling, but also with errors due to model misspecification, approximations due to model evaluation, and model parameters [36]. This requires these errors to all be independent such that the residuals remain uncorrelated, however, this does not always hold for fitted models [12].

Errors in dosing, sampling history, and model misspecification may introduce time-dependent error variances, or serial correlations [12]. Typically, model misspecification and serial correlation is diagnosed through the examination of the residuals, however, some serial correlation is considered unavoidable and how it directly relates to the model can be difficult to ascertain. Karlsson *et al.* [12] concluded that neither accuracy nor precision of the structural parameters improved with the recognition of serial correlations, but that such improvement can only be obtained through an improved structural model. However, consideration of autocorrelated error structures can lead to more accurate variance components. Furthermore, time-dependent errors due to inaccurate recordings of sample times in complex dosing studies can be difficult to handle, let alone potential time dependencies within the model parameters [36]. This has led to suggesting the inclusion of autoregressive, AR(1), models to help account for these time correlated errors [3, 5, 12].

All of these uncertainties can affect the results and are frequently attributed to not fully understand-

ing the governing processes or the complexity being too great to fully quantify. An alternate and more sophisticated method for handling models with structural misspecifications and serial correlations is the use of stochastic differential equations (SDE) [22, 35]. This approach is more flexible with regards to specifying models with different residual error correlation patterns, while still including the statistical functionality of the AR(1) model [22]. These grey-box models are stochastic state space models utilizing SDEs to describe the dynamics of the states in continuous time while incorporating a discrete time measurement equation. An immediate advantage and consequence of SDE models is the ability to relegate the intra-individual error associated with model misspecification into a system noise term for unspecified dynamics and the intra-individual error associated with measurement noise accounting for uncorrelated errors, such as assay error, into their respective components [16, 35].

Following the procedures presented by Overgaard *et al.* [22] and Tornøe *et al.* [36], this chapter aims to implement SDEs into an nonlinear mixed effects modeling framework to elucidate the benefits of this methodology in terms of population pharmacokinetic analysis. Using Metformin clinical data in a PK example, the purpose is to illustrate the application of SDEs to model development and diagnostics through (1) separation of system noise from measurement noise within the intra-individual variability, (2) accounting for serially correlated residuals, and (3) estimation of time-varying parameters similar to deconvolution. Secondly, the purpose is to compare the results of multiple numerical SDE solvers to the common ordinary differential equation (ODE) approach.

## 6.2 Nonlinear Mixed Effects

Nonlinear mixed effect models are used for repeated measures, and can be thought of as a hierarchical modeling framework involving both fixed-effects for population parameters and random effects incorporating uncertainty associated with inter- and intra- individual variability [24, 25, 34]. The intra-individual variability is described in the first stage by the difference between the individual predictions and observations modeled as

$$y_{i,j} = g(x_{i,j}, \phi_i) + e_{i,j}, \quad e_{i,j} \sim N(0, \sigma^2) \quad i = 1, \dots, N, \quad j = 1, \dots, n_i \quad (6.1)$$

where  $y_{i,j}$  is the  $j$ th response for the  $i$ th individual,  $g(\cdot)$  is the nonlinear observation function for the individual specific parameter set  $\phi_i$  and state dynamics,  $x_{i,j}$ ,  $N$  is the number of individuals (or repeated measures), and  $n_i$  is the number of measurements for each individual. The residual error terms  $e_{i,j}$  are assumed to be independently and identically distributed (i.i.d.) normal random variables with mean zero and variance  $\sigma^2$ .

The state dynamics  $x$  are used to quantify the behavior of the system. These are most commonly

modeled using ordinary differential equations (ODEs) [22] described below

$$\frac{dx}{dt} = f(t, x, u; \phi_i), \quad x(0; \phi) = x_0, \quad t \geq t_0, \quad (6.2)$$

where  $x$  is an  $M$ -dimensional dependent variable vector,  $x_0$  is the initial conditions,  $f(\cdot)$  is the model,  $t$  is an independent variable,  $u$  is an exogenous input, and  $\phi_i$  is the  $O$ -dimensional parameter vector. As we are interested in decomposing the noise affecting the system into a model misspecification term representing the uncertainty associated with unknown or incorrectly specified dynamics and measurement noise term accounting for uncorrelated errors such as assay error [16, 22, 35, 36], this is accomplished through the incorporation of stochastic differential equations (SDEs). Stochastic differential equations allow the system noise to be added directly to the differential equations which accounts for random variations to the evolution of the states that may not be strictly accounted for within the structural model [22]. This leads to the following SDE model formulation

$$\begin{aligned} dx_i &= f(x_i, u_i, t, \phi_i)dt + \sigma_w dw, \\ w_{it} - w_{is} &\sim N(0, |t - s|I), \end{aligned} \quad (6.3)$$

where  $x$ ,  $u$ ,  $t$ ,  $f(\cdot)$ , and  $\phi$  are as previously defined. The identity matrix is denoted by  $I$  and  $\sigma_w dw$  is the system noise. The structural model  $f(\cdot)$  is the drift term, the matrix  $\sigma_w$  is a scaling diffusion term, while  $w$  is a standard Wiener process, commonly referred to as Brownian motion [10, 36]. The standard Wiener process  $w$  is a nonstationary stochastic process with mutually independent (orthogonal) increments ( $w_t - w_s$ ) which are normally distributed with mean zero and variance  $|t - s|I$  [8, 15]. When the diffusion term  $\sigma_w$  is zero, the SDE (6.3) reduces to an ODE (6.2), and therefore, the physiological interpretation of the parameters is preserved within the SDE model formulation [36].

The inter-individual variability is accounted for in the second stage by modeling the individual parameters as

$$\phi_i = h(\theta, Z_i) \exp(\eta_i), \quad \eta_i \sim N(0, \Omega), \quad (6.4)$$

where  $h(\cdot)$  is the parameter structural model, which is a function of the fixed-effects parameters  $\theta$  and potential covariates  $Z_i$ . The random effects  $\eta_i$  describe each individual's variation from the population, and are independent and multivariate normally distributed with mean zero and covariance  $\Omega$ . This results in a multivariate log-normal distribution for the individual parameters [22]. Finally, the set of population parameters to be estimated in the nonlinear mixed effects model utilizing SDEs represent the intra-individual variability, inter-individual variability, model misspecification or system noise, and fixed-effects parameters and are given by the set  $(\sigma^2, \Omega, \sigma_w, \text{ and } \theta)$ , respectively.

A number of methods exist to estimate parameters for the model (6.1), but we shall focus on maximum likelihood estimation due to its strength in testing hypotheses and constructing confidence intervals. Maximum likelihood estimation also has a number of optimal properties in estimation including

sufficiency, consistency, efficiency, and parameterization invariance [21]. For more details, Davidian and Giltinan [5] give a description and comparison for various estimation methods for nonlinear mixed-effects models. Maximum likelihood estimation is based upon maximizing the marginal density

$$L(\theta, \sigma^2, \sigma_w, \Omega) \propto \prod_{i=1}^N \int p_1(\mathcal{Y}_{in_i} | \eta_i, \theta, \sigma^2, \sigma_w, d_i) p_2(\eta_i | \Omega) d\eta_i \quad (6.5)$$

$$= \prod_{i=1}^N \int \exp(l_i) d\eta_i, \quad (6.6)$$

where  $L$  is the population likelihood function,  $\mathcal{Y}_{ij} = [y_{i1}, \dots, y_{in_i}]$  represents all observations of the  $i$ th individual up to time  $t_{ij}$ , and, assuming a normal conditional density, the first-stage distribution is

$$p_1(y_{in_i} | \eta_i, \theta, \sigma^2, \sigma_w, d_i) \approx \prod_{j=1}^{n_i} \frac{\exp(-\frac{1}{2} e_{ij}^T R_{i(j|j-1)}^{-1} e_{ij})}{\sqrt{|2\pi R_{i(j|j-1)}|}}, \quad (6.7)$$

where  $e_{i,j} = y_{i,j} - g(x_{i,j}, \phi_i)$  is the residual from (6.1) and  $R_{i(j|j-1)}$  is the prediction covariance, while the second-stage distribution (6.4) remains  $p_2(\eta_i | \Omega)$ . The *a posteriori* log-likelihood function for the random effect of the  $i$ th individual is now

$$l_i = -\frac{1}{2} \sum_{j=1}^{n_i} (e_{ij}^T R_{i(j|j-1)}^{-1} e_{ij} + \log |2\pi R_{i(j|j-1)}|) - \frac{1}{2} \eta_i^T \Omega^{-1} \eta_i - \frac{1}{2} \log |2\pi \Omega|. \quad (6.8)$$

A number of methods exist to approximate the population likelihood (6.6). Sparse grid techniques provide one method which yields accurate results for a broad classes of functions [4, 7, 29, 31, 32]. More details for this method are given by Smith [28]. Due to the necessity to update parameter estimates, the sparse grid technique requires a gradient descent method to accomplish this.

Another method is Monte Carlo integration. This offers the advantages that the convergence is independent of the dimension of parameter space [28] and parameter estimates are easily updated within an expectation maximization framework. As the focus is utilizing SDEs within nonlinear mixed effect models, Monte Carlo integration is chosen as it does not depend on the smoothness of the population likelihood (6.6). Utilizing Monte Carlo integration techniques to approximate the population likelihood (6.6), the critical step to estimation is dependent upon selecting the appropriate sampling distribution [23]. In general, quasi-Monte Carlo sampling is preferred as it has shown a faster rate of convergence ( $O(\ln R^p/R)$ ) and better assurance of error over classical Monte Carlo [27]. From Monte Carlo integration, the expected value of  $f(x)$  under a distribution  $p$ , defined as  $I[f]$ , is

$$I[f] = E_p[f(x)] = \int f(x) p(x) dx \simeq \frac{1}{N} \sum_{k=1}^N f(x^{(k)}). \quad (6.9)$$

If  $p(x)$  is not easily sampled from but easily evaluated for a given  $x$ , a sampling distribution  $q(x)$  can be used such that

$$\begin{aligned} I[f] &= \int f(x) \frac{p(x)}{q(x)} q(x) dx \\ &\simeq \frac{1}{N} \sum_{k=1}^N \tilde{w} f(x^{(k)}), \quad \tilde{w} = \frac{p(x^{(k)})}{q(x^{(k)})}, \end{aligned} \quad (6.10)$$

known as importance sampling. Applying the importance sampling methodology to the population likelihood (6.5), we obtain

$$L(\theta, \sigma^2, \sigma_w, \Omega) \propto \prod_{i=1}^N \int p_1(\mathcal{Y}_{in_i} | \eta_i, \theta, \sigma^2, \sigma_w, d_i) \frac{r(0, \Omega)}{q(\eta_i, \omega_i)} q(\eta_i, \omega_i) d\eta_i, \quad (6.11)$$

where we sample from  $q(\eta_i, \omega_i)$ , the sampling distribution, assuming a Gaussian distribution with mean centered around each individual's  $\eta_i$  with individual covariance  $\omega_i$ . The individual log-likelihood then becomes

$$l_i = -\frac{1}{2} \sum_{j=1}^{n_i} \left( e_{ij}^T R_{i(j|j-1)}^{-1} e_{ij} + \log |2\pi R_{i(j|j-1)}| \right) + \frac{1}{2} \eta_i^{(k)T} \Omega^{-1} \eta_i^{(k)} + \frac{1}{2} \log |2\pi \Omega| - \frac{1}{2} \zeta_i^{(k)T} \omega_i \zeta_i^{(k)} - \frac{1}{2} \log |2\pi \omega_i|, \quad (6.12)$$

where  $\eta_i^{(k)}$  is an  $O$ -dimensional sample for the individual  $\eta_i$  taken from the sampling distribution,  $\zeta_i^{(k)} = \eta_i^{(k)} - \eta_i$  is the deviation of the sample  $\eta_i^{(k)}$  from the prior mean  $\eta_i$ , and

$$\log(\tilde{w}) = \frac{1}{2} \eta_i^{(k)T} \Omega^{-1} \eta_i^{(k)} + \frac{1}{2} \log |2\pi \Omega| - \frac{1}{2} \zeta_i^{(k)T} \omega_i \zeta_i^{(k)} - \frac{1}{2} \log |2\pi \omega_i| \quad (6.13)$$

represent the importance weights,  $\tilde{w} = r(0, \Omega)/q(\eta_i, \omega_i)$ . This individual *a posteriori* log-likelihood function is based on the one-step prediction error [22, 36]. As previously stated, when no system noise is present ( $\sigma_w = 0$ ), the SDE model will reduce to the more familiar ODE, and therefore, the one-step prediction covariance will reduce to the ODE residual covariance,  $R_{i(j|j-1)} = \sigma^2$  [22].

The one-step prediction output  $\hat{y}_{i(j|j-1)}$  is the optimal prediction of the  $j$ th measurement before that measurement is observed while  $R_{i(j|j-1)}$  is the covariance for that prediction [36]. Thus, the Gaussian conditioned densities are completely described by

$$\hat{y}_{i(j|j-1)} = E[y_{ij} | \mathcal{Y}_{i(j-1)}, \phi_i, \sigma^2, \sigma_w, d_i], \quad (6.14)$$

$$R_{i(j|j-1)} = V[y_{ij} | \mathcal{Y}_{i(j-1)}, \phi_i, \sigma^2, \sigma_w, d_i], \quad (6.15)$$

where  $\hat{y}_{i(j|j-1)}$  and  $R_{i(j|j-1)}$  are the conditional mean and covariance, respectively, of  $y_{ij}$  conditioned on all previous measurements up to time  $t_{j-1}$  for individual  $i$  denoted by  $\mathcal{Y}_{i(j-1)} = [y_{i1}, \dots, y_{i(j-1)}]$ . The

subscript notation  $i(j|j-1)$  utilized in equations (6.14) and (6.15) refer to the prediction at  $j$  based on all  $j-1$  measurements for individual  $i$  [36].

The one step prediction errors are now calculated as

$$e_{ij} = y_{ij} - \hat{y}_{i(j|j-1)}, \quad e_{ij} \sim N(0, R_{i(j|j-1)}). \quad (6.16)$$

This one-step prediction  $\hat{y}_{i(j|j-1)}$  and covariance  $R_{i(j|j-1)}$  are calculated using the nonlinear extensions of the Kalman filter [13, 14].

## 6.3 Kalman Filter

Using the work presented by Overgaard [22] and Tornøe [35, 36], the derivation and implementation of the various Kalman filters within the nonlinear mixed effects framework is now presented.

### 6.3.1 Extended Kalman Filter Implementation

The Kalman filter [13] is a recursive algorithm, which calculates the optimal state of a system by taking a weighted average of the probability distribution from the model and the probability distribution from the measurement, assuming the model is linear and the distributions are Gaussian. When these restrictive assumptions do not hold, adjustments to the Kalman filter must be made, as discussed in Chapter 2. The Extended Kalman filter (EKF) is an efficient extension to the Kalman filter which accounts for nonlinear models by using the linearized model within the classical filter equations. This provides estimates for the conditional mean and covariance for the assumed Gaussian conditional densities needed within the likelihood function in equation 6.8.

The EKF equations are grouped into two components: the prediction step and the update step. The prediction step consists of predicting the state and output variables ahead to the next measurement, while the update step utilizes the measurement to update the state predictions.

The one-step state predictions of the EKF, which are the optimal (minimum variance) prediction of the mean and covariance, are calculated by solving the state and covariance prediction equations from time  $t_{j-1}$  until  $t_j$ , where  $t_{j-1}$  is the time point of the last measurement and  $t_j$  is the time point of the following measurement,

$$\frac{d\hat{x}_{i(t|j-1)}}{dt} = f(\hat{x}_{i(t|j-1)}, d_i, \phi_i), \quad t \in [t_{j-1}, t_j], \quad (6.17)$$

$$\frac{d\hat{P}_{i(t|j-1)}}{dt} = A_{it}P_{i(t|j-1)} + P_{i(t|j-1)}A_{it}^T + \sigma_w\sigma_w^T, \quad (6.18)$$



with initial conditions

$$\hat{x}_{i(1|0)} = x_{i0}, \quad (6.19)$$

$$P_{i(1|0)} = P_{i0} = \int_{t_1}^{t_2} e^{A_{it}s} \sigma_w \sigma_w^T (e^{A_{it}s})^T ds, \quad (6.20)$$

where  $x_{i0}$  are the initial conditions for the states. The integral in equation (6.20) specifying the initial state covariance  $P_{i0}$  is taken as the integral of the Wiener process and the state dynamics over the time period of the first two measurements.

While the EKF is an exact, optimal solution to the state filtering problem in linear systems, utilizing the linearization of the system within the covariance prediction equation, it is only a first-order approximation for nonlinear systems. The matrix  $A_{it}$  is the first-order Taylor expansion of the state equations in equation (6.17) about the current state at time  $t$ , defined as

$$A_{it} = \left. \frac{\partial g}{\partial x} \right|_{x=\hat{x}_{i(t|j-1)}}. \quad (6.21)$$

Now, the EKF one-step output prediction equations to be used in the nonlinear mixed effects are

$$\hat{y}_{i(j|j-1)} = g(\phi_i, \hat{x}_{i(j|j-1)}) \quad (6.22)$$

$$R_{i(j|j-1)} = C_{ij} P_{i(j|j-1)} C_{ij}^T + \sigma^2 \quad (6.23)$$

where  $C_{ij}$  is first-order Taylor expansion of the measurement equation 6.1 about the current prediction, defined below

$$C_{ij} = \left. \frac{\partial f}{\partial x} \right|_{x=\hat{x}_{i(j|j-1)}}. \quad (6.24)$$

The one-step output covariance  $R_{i(j|j-1)}$  is therefore the sum of the state covariance associated with the observed state ( $C_{ij} P_{i(j|j-1)} C_{ij}^T$ ) and the covariance associated with the measurements ( $\sigma^2$ ). As previously state, in the case of no system noise ( $\sigma_w = 0$ ), the one-step output prediction  $\hat{y}_{i(j|j-1)}$  and covariance  $R_{i(j|j-1)}$  will reduce to the ODE prediction  $\hat{y}_{ij}$  and residual covariance  $\sigma^2$  typically utilized within the likelihood function [34].

Lastly, the second component of the EKF is the update step. Conditioning on the  $j$ th measurement, the one-step prediction and covariance are updated using the EKF state-update equations

$$\hat{x}_{i(j|j)} = \hat{x}_{i(j|j-1)} + K_{ij}(y_{ij} - \hat{y}_{i(j|j-1)}) \quad (6.25)$$

$$P_{i(j|j)} = (I - K_{ij} C_{ij}) P_{i(j|j-1)}, \quad (6.26)$$

where  $\hat{x}_{i(j|j)}$  is the updated state estimate,  $P_{i(j|j)}$  is the updated state covariance, and  $K_{ij}$  is the Kalman

gain given below

$$K_{ij} = P_{i(j|j-1)} C_{ij}^T (C_{ij} P_{i(j|j-1)} C_{ij}^T + \sigma^2)^{-1} = P_{i(jj-1)} C_{ij}^T R_{i(j|j-1)}^{-1}. \quad (6.27)$$

The optimal state estimate at time  $j$ ,  $\hat{x}_{i(j|j)}$ , is equivalent to the best state prediction  $\hat{x}_{i(j|j-1)}$  before a measurement is taken plus a correcting term consisting of an optimal weighting term multiplied by the difference between the measurement  $y_{ij}$  and the one-step prediction [34]. The Kalman gain is the weighting term which corrects the estimate based upon the covariance of the state prediction and observations. If the measurement has a large variance  $\sigma^2$ , the Kalman gain becomes small causing the correction term to go to zero and the noisy measurement to be neglected. When the system noise is large implying uncertainty in the system output, the Kalman gain will approach one due to the prediction covariance becoming large. More specifically, as the limit of the noise increases ( $\sigma_w \rightarrow \infty$ ,  $P \rightarrow \infty$ ), the Kalman gain goes to one ( $K_{ij} \rightarrow 1$ ) resulting in the updated state being equal to the measurement [19]. A comprehensive EKF implementation is presented by Tornøe et. al. [34].

### 6.3.2 Unscented Kalman Filter Implementation

Due to the localized first-order Taylor expansions, the EKF can only obtain first order accuracy for all distributions. However, another Kalman filter has been constructed which better preserves the distribution statistics as it passes through the nonlinearity. The Unscented Kalman filter (UKF) overcomes shortcomings of the EKF by utilizing the 'unscented transformation.'

The unscented transformation (UT) is a method used to calculate the statistics of a random variable which undergoes a nonlinear transformation [11]. Instead of a linearization, the UT propagates a set of sample points through the nonlinear model which will capture the posterior mean and covariance to at least 2nd order for all distributions, and at least 3rd order accuracy for Gaussian distributions [9, 11].

Assume we have a random variable,  $z$ , with dimension  $L$ , which has mean  $\hat{z}$  and covariance,  $P_z$ . This random variable gets propagated through a nonlinear function,  $\psi = g(z)$ . To calculate the statistics of  $\psi$ , we form a matrix,  $\chi$ , of  $2L + 1$  sigma vectors,  $\chi_i$ . This matrix,  $\chi$ , is constructed as follows,

$$\chi = [\hat{z}, \hat{z} \mathbf{1}_{\mathbf{x}L} + (\sqrt{(L + \lambda)P_z})_{\mathbf{L}}, \hat{z} \mathbf{1}_{\mathbf{x}L} - (\sqrt{(L + \lambda)P_z})_{\mathbf{L}}], \quad (6.28)$$

where  $\hat{z}$  is a column vector,  $\hat{z} \mathbf{1}_{\mathbf{x}L}$  is a matrix of the column vector  $\hat{z}$ , and  $(\sqrt{(L + \lambda)P_z})_{\mathbf{L}}$  is an  $L \times L$  matrix.

The corresponding weights ( $W_i$ ) for the sigma vectors are as follows

$$W_0^{(m)} = \frac{\lambda}{(L + \lambda)} \quad (6.29)$$

$$W_0^{(c)} = \frac{\lambda}{(L + \lambda)} + (1 - \alpha^2 + \beta) \quad (6.30)$$

$$W_i^{(m)} = W_i^{(c)} = \frac{1}{2(L + \lambda)} \quad i = 1, \dots, 2L, \quad (6.31)$$

where  $\lambda = \alpha^2(L + \kappa) - L$  is a scaling parameter. The tuning parameter,  $\alpha$ , is used to determine the spread of the sigma points around  $\hat{z}$ , and takes values between  $1 \geq \alpha \geq 10^{-4}$  depending on the problem. The tuning parameter,  $\kappa$ , is a secondary scaling parameter which is optimally set to  $3 - L$  [9]. Lastly,  $\beta$  is used to incorporate prior knowledge of the distribution of  $x$  (for Gaussian distributions,  $\beta = 2$  is optimal) [38]. From our matrix of sigma points (6.28),  $(\sqrt{(L + \lambda)P_z})_i$  is the  $i$ th row of the matrix square root [38]. The sigma vectors are then propagated through the nonlinear function accordingly,

$$\psi_i = g(\chi_i), \quad i = 0, \dots, 2L, \quad (6.32)$$

with the mean and covariance of  $\psi$  being approximated using a weighted sample mean and covariance of the posterior sigma points,

$$\hat{\psi} \approx \sum_{i=0}^{2L} W_i^{(m)} \psi_i \quad (6.33)$$

$$P_\psi \approx \sum_{i=0}^{2L} W_i^{(c)} (\psi_i - \hat{\psi})(\psi_i - \hat{\psi})^T. \quad (6.34)$$

Following the same procedure as the EKF, the one-step state predictions for the UKF are calculated by constructing the sigma points (6.28) around the current states  $x_{i(t|j-1)}$  and propagating them through the model from  $t_{j-1}$  to  $t_j$ , as before,

$$\chi_{k[i(t|j-1)]}^* = \frac{d\chi_{k[i(t|j-1)]}}{dt} = f(\chi_{k[i(t|j-1)]}, d_i, \phi_i), \quad t \in [t_{j-1}, t_j], \quad (6.35)$$

where  $\chi_{k[i(t|j-1)]}^*$  is the solution of the model for each sigma vector  $k$  of subject  $i$ . Using the weights (6.29, 6.30, 6.31), the mean and covariance is resolved by

$$\hat{x}_{i(t|j-1)} = \sum_{k=0}^{2L} W_k^{(m)} \chi_{k[i(t|j-1)]}^* \quad (6.36)$$

$$\hat{P}_{i(t|j-1)} = \sum_{k=0}^{2L} W_k^{(c)} (\chi_{k[i(t|j-1)]}^* - \hat{x}_{i(t|j-1)})(\chi_{k[i(t|j-1)]}^* - \hat{x}_{i(t|j-1)})^T + \sigma_w \sigma_w^T. \quad (6.37)$$

Using the state mean prediction (6.36), a new set of sigma points is constructed for the observation function (6.1)

$$\Lambda_{k[i(t|j-1)]} = [\hat{x}_{i(t|j-1)}, \hat{x}_{i(t|j-1)} \mathbf{1}_{\mathbf{xL}} + (\sqrt{(L + \lambda)\hat{P}_{i(t|j-1)}})_{\mathbf{L}}, \hat{x}_{i(t|j-1)} \mathbf{1}_{\mathbf{xL}} - (\sqrt{(L + \lambda)\hat{P}_{i(t|j-1)}})_{\mathbf{L}}], \quad (6.38)$$

and subsequently propagated through the observation function (6.1)

$$\Lambda_{k[i(t|j-1)]}^* = g(\Lambda_{k[i(t|j-1)]}, \phi_i), \quad (6.39)$$

which is used to obtain the observed state predictor and covariance

$$\hat{z}_{i(t|j-1)} = \sum_{k=0}^{2L} W_k^{m_z} \Lambda_{k[i(t|j-1)]}^* \quad (6.40)$$

$$\hat{P}_{i(t|j-1),zz}^z = \sum_{k=0}^{2L} W_k^{c_z} (\Lambda_{k[i(t|j-1)]}^* - \hat{z}_{k[i(t|j-1)]}) (\Lambda_{k[i(t|j-1)]}^* - \hat{z}_{k[i(t|j-1)]})^T + \sigma^2. \quad (6.41)$$

Now, the UKF one-step output prediction equations to be used in the nonlinear mixed effects are

$$\hat{y}_{i(j|j-1)} = g(\phi_i, \hat{x}_{i(j|j-1)}) \quad (6.42)$$

$$R_{i(j|j-1)} = \hat{P}_{k[i(j|j-1)],zz}^z \quad (6.43)$$

Lastly, the UKF equations utilize the observation sigma points (6.38) to calculate the observed cross-covariance

$$\hat{P}_{i(t|j-1),xz}^z = \sum_{k=0}^{2L} W_k^{c_z} (\Lambda_{k[i(t|j-1)]}^* - \hat{x}_{k[i(t|j-1)]}) (\Lambda_{k[i(t|j-1)]}^* - \hat{z}_{k[i(t|j-1)]})^T. \quad (6.44)$$

Using this, the state mean prediction (6.36), and state covariance prediction (6.41), the one-step state and state covariance predictions are updated by adjusting for the  $j$ th measurement, similar to the EKF, as follows

$$\hat{x}_{i(j|j)} = \hat{x}_{i(j|j-1)} + K_{ij}(\hat{y}_{i(j|j-1)} - y_{ij}) \quad (6.45)$$

$$\hat{P}_{i(j|j)} = \hat{P}_{i(j|j-1)} - K_{ij} \hat{P}_{i(j|j-1),zz}^z K_{ij}^T, \quad (6.46)$$

where  $\hat{x}_{i(j|j)}$  is the updated state based upon the measurement,  $\hat{P}_{i(j|j)}$  is the updated covariance, and  $K_{ij}$  is the Kalman gain calculated by

$$K_{ij} = \hat{P}_{i(t|j-1),xz}^z (\hat{P}_{i(t|j-1),zz}^z)^{-1}. \quad (6.47)$$

As before with the EKF, the Kalman gain is used as a weighting term to optimally combine the model

and data conditioned on their covariances.

## 6.4 Study and Data

Metformin is the most commonly prescribed treatment for type 2 diabetes in the world, however the mechanism for its glucose-lowering action remains poorly understood. A new delayed release (DR) metformin tablet was formulated to target delivery of metformin to the lower gut to enhance secretion of gut hormones while decreasing systemic exposure [33]. The metformin data was collected as part of a randomized four period, crossover study comparing the pharmacokinetics of the new delayed release formulation of metformin HCl. A single dose of 2000mg of metformin extended release (XR) was given as four 500-mg tablets immediately after a standardized meal. Pharmacokinetic samples for the measurement of plasma metformin were collected every half hour for the first 3 hours and between hours 12 to 14, and every hour thereafter up to 36 hours [2]. This was done for 16 healthy subjects, and is presented below.

## 6.5 Results

The application of SDEs to population PK/PD modeling was carried out using clinical PK metformin (XR) data from 16 healthy subjects to illustrate its utility to model development. A standard PK model is presented which illuminates known deficiencies and is used to motivate tracking unexplained time variations in the deficient component of the model. This then leads to the application of the SDE approach where multiple filters are executed and compared. Finally, a final ODE model is compared to the SDE models.

The inter-individual variability of the population, and individual parameter vector  $\phi_i$ , is assumed to be distributed around the population mean parameter vector  $\theta$  according to a log-normal distribution as in equation (6.4), more specifically,

$$\phi_i = \theta \exp(\eta_i), \quad \eta_i \in N(0, \Omega), \quad (6.48)$$

where the random-effects  $\eta_i$  influencing the individual vector  $\phi_i$  are assumed multivariate normal with mean zero and covariance matrix  $\Omega$ .

### 6.5.1 Initial Model: 2-Compartment Oral

A two-compartment micro rate-constant model with first-order absorption and elimination was selected as the initial PK model describing the single dose (QD) oral administration of metformin. A diagram representing this model is given by Figure 6.1. Previous studies have shown that metformin absorption is incomplete and variable [6], and therefore first-order absorption may not be appropriate; however,

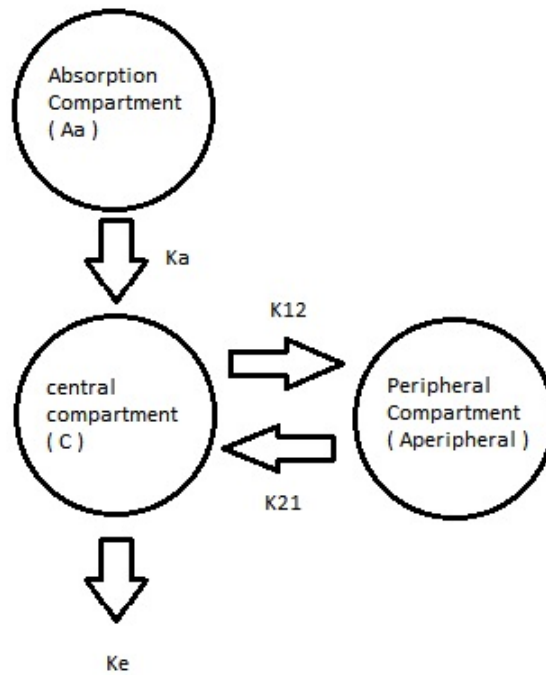


Figure 6.1: Diagram representing the two compartment model. Absorption compartment,  $A_a$ , represents the gut. Drug is taken into the absorption compartment and is transported into the central compartment at rate  $k_a$ . The drug can diffuse into the peripheral compartment  $A_{peripheral}$  at a rate  $k_{12}$  and can diffuse back at rate  $k_{21}$ . The drug will be eliminated from the body at rate  $k_e$ .

this is done in order to demonstrate the utility of SDEs to model development through the estimation of model misspecification. The system of ODEs governing the PK model can be written in matrix form, along with observation equation, as

$$\frac{d}{dt} \begin{pmatrix} A_a \\ C \\ A_{peripheral} \end{pmatrix} = \begin{pmatrix} -k_a & 0 & 0 \\ \frac{k_a}{V} & -(k_{12} + k_e) & \frac{k_{21}}{V} \\ 0 & k_{12}V & -k_{21} \end{pmatrix} \begin{pmatrix} A_a \\ C \\ A_{peripheral} \end{pmatrix} \quad (6.49)$$

$$\log(C_{obs}) = \log(C) + e, \quad e \sim N(0, \sigma^2) \quad (6.50)$$

where  $A_a$  is the state variable for the amount of drug in the absorption compartment,  $C$  is the concentration of drug in the central compartment,  $A_{peripheral}$  is the amount of drug in the peripheral compartment, and  $C_{obs}$  is the observed metformin drug concentration within the plasma.

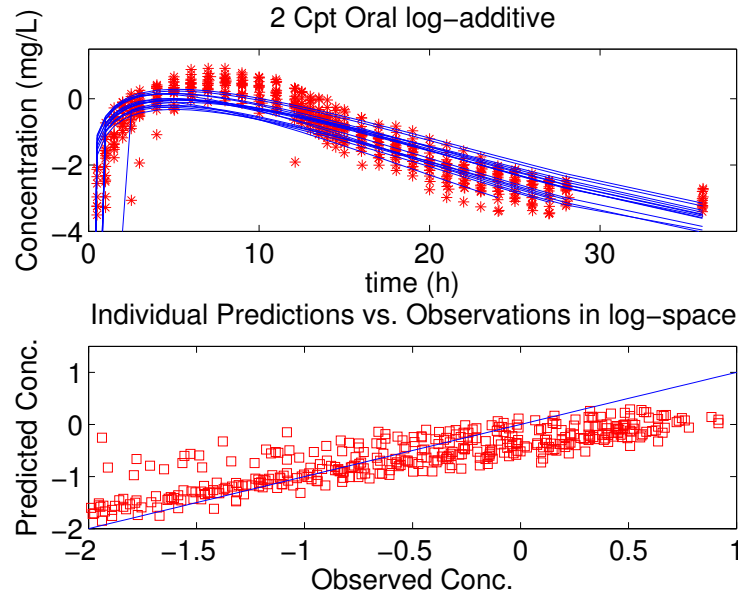


Figure 6.2: Top: Population PK model fit for 16 subjects concentration profiles in log-space for concentration. Base model fit utilizes a 2-compartment oral absorption model with log-additive error. Bottom: Individual predictions vs. individual concentrations along with unity line (blue). Unity line represents the ideal situation where the model perfectly predicts the observations.

The model (6.49) is parameterized in terms of rate parameters  $k_a$ ,  $k_{12}$ ,  $k_{21}$ , and  $k_e$  to represent the

kinetics of the drug as it travels through the system. The first-order oral absorption is governed by the rate constant  $k_a$  and the amount of drug present. The kinetics between the central and peripheral compartments are governed by the rate constants  $k_{12}$  and  $k_{21}$ , while the volume of the central compartment is represented by  $V$ . The rate at which a drug is eliminated from the system is represented by  $k_e$ .

The parameter estimates of the initial PK model are given in Table 6.1. The observed metformin concentration-time profiles for all subjects in the study are displayed in Figure 6.2. The concentration profiles miss the maximum observed concentrations and possess different qualitative features from the observations. Reviewing the predicted and observed plasma concentrations, Figure 6.2, the unity line (blue) represents the ideal situation where the model predicts the observations. Given the predictions appear qualitatively different from the unity line, there appears to be an underlying deficiency in the model. The plasma concentration profiles, the differences between the predicted and observed concentrations, along with the known uncertainty in absorption leads to the following adaptation of the model to better describe the absorption process [6, 37].

### 6.5.2 Absorption Rate Tracking Model: EKF and UKF

Utilizing the information from the initial model, the main area of model refinement should be the absorption model. The absorption rate  $k_a$  was initially assumed to be constant; however, to account for the suspicion of temporal dynamics, we concatenate the absorption rate parameter  $k_a$  into the state equations and allow it to fluctuate due to noise similar to a random walk. Instead of implementing a structural model with built in assumptions for  $k_a$  to account for these time variations, the filters will shift  $k_a$  over time to account for uncertainties in the states to best explain the concentration observations. To account for this, the model dynamics for  $k_a$  are set to zero, thereby allowing only the noise term  $\sigma_{k_a}$  to drive the process. Assigning the noise terms  $\sigma_{abs}$ ,  $\sigma_{central}$ ,  $\sigma_{peripheral}$ , and  $\sigma_{k_a}$  to be mixed effects within the modeling framework, this allows the estimation of model misspecification for each compartment. If the noise  $\sigma_{k_a}$  is nonzero, this indicates the assumption that the absorption rate parameter is constant may not hold, and that  $k_a$  may be better explained by a time-varying process. This is significant as it allows a process for model refinement.

This leads to the following model refinements for  $k_a$ , written out as an SDE as

$$d \begin{pmatrix} \log|k_a| \\ A_a \\ C \\ A_{peripheral} \end{pmatrix} = \begin{pmatrix} 0 \\ -\exp(\log|k_a|)A_a \\ \frac{\exp(\log|k_a|)}{V}A_a - (k_{12} + k_e)C + \frac{k_{21}}{V}A_{peripheral} \\ k_{12}VC - k_{21}A_{peripheral} \end{pmatrix} dt + \begin{pmatrix} \sigma_{k_a} & 0 & 0 & 0 \\ 0 & \sigma_{A_a} & 0 & 0 \\ 0 & 0 & \sigma_{central} & 0 \\ 0 & 0 & 0 & \sigma_{peripheral} \end{pmatrix} dw_t \quad (6.51)$$

$$\log(C_{obs}) = \log(C) + e, \quad e \sim N(0, \sigma^2) \quad (6.52)$$



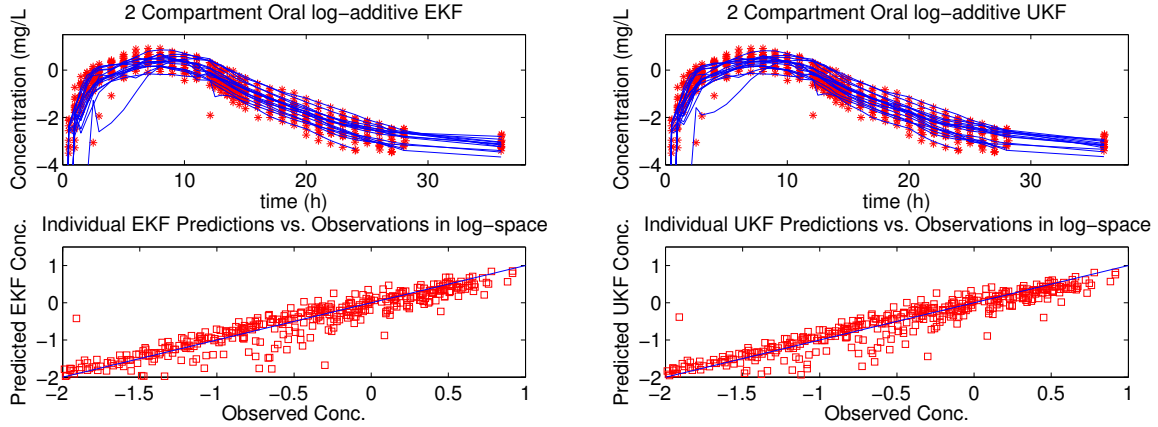


Figure 6.3: Left: Population PK model fit utilizing EKF for 16 subjects concentration profiles in log-space. Below is the individual predictions vs individual concentrations with unity line. Right: Population PK model fit utilizing UKF for 16 subjects concentration profiles in log-space. Below is the individual predictions vs individual concentrations with unity line (blue). Unity line represents the ideal situation where the model perfectly predicts the observations.

where  $k_a$  is the state variable for the absorption rate parameter and  $\sigma_{A_a}$ ,  $\sigma_{central}$ ,  $\sigma_{peripheral}$ , and  $\sigma_{k_a}$  are the noise terms associated with the model misspecification for each compartment. Given that the absorption rate  $k_a$  must be constrained to non-negative space, the state equation for  $k_a$  is log-transformed. This prevents the rate constant from becoming negative while keeping the error additive, which is required for the EKF and UKF.

The estimated model parameters for the absorption rate tracking model for both the EKF and UKF are presented in Table 6.1. Comparing the plasma concentration profiles for the absorption rate tracking models, Figure 6.3, to the initial two compartment model plasma concentration profiles, Figure 6.2, the absorption rate tracking model manages to better capture the absorption phase of the concentration profiles and no longer displays a missing underlying process in the individual predictions vs concentrations. Comparing the filtering methodologies, they appear to qualitatively match with minimal quantitative differences. Reviewing the estimates in Table 6.1, the UKF manages to converge to a better loglikelihood despite the qualitative similarities in profiles. This is due to the increased confidence in the filter estimates from the UKF, which is seen in Figure 6.4. While both filters agree in terms of the mean prediction for subject one, the prediction interval for the EKF is larger resulting in more variability associated with the estimate. Over this same profile, the UKF manages to better encapsulate the variability in the filter estimate over the time scale. This leads to the better log-likelihood.

Along with the differences in the prediction intervals, the filters exhibit other important differences. While both the EKF and UKF prescribe minimal error to the central and peripheral compartments ( $\sigma_{central}$  and  $\sigma_{peripheral}$ , respectively) the breakdown of the variability associated within the absorp-

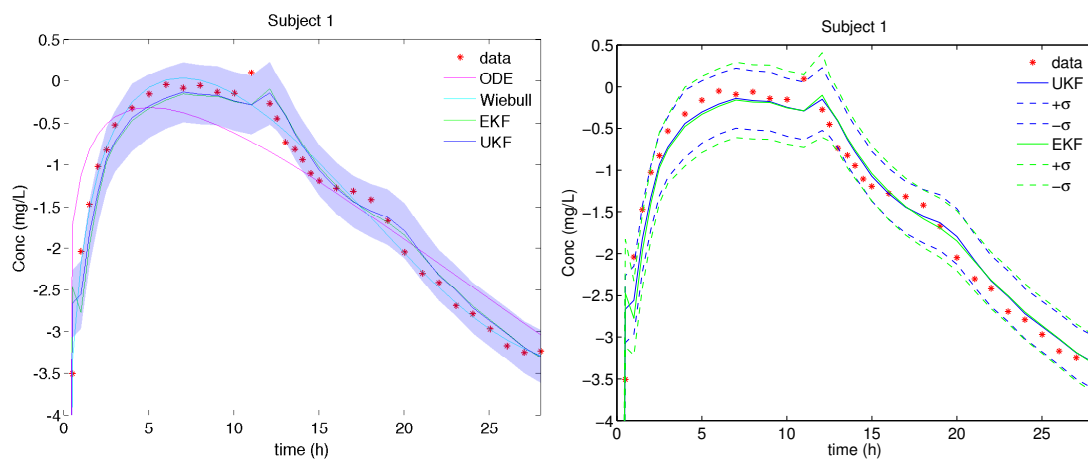


Figure 6.4: Left: Plasma concentration profile for Subject 1 including data, initial 2-compartment model (ODE), EKF absorption rate tracking model (EKF), UKF absorption rate tracking model (UKF), and Wiebull absorption 2-compartment model (Wiebull); prediction intervals are presented for the UKF calculated as  $\hat{y}_{j|j-1} \pm \sqrt{R_{(j|j-1)}}$  Right: EKF and UKF filter predictions for Subject 1 along with prediction intervals for each filter.

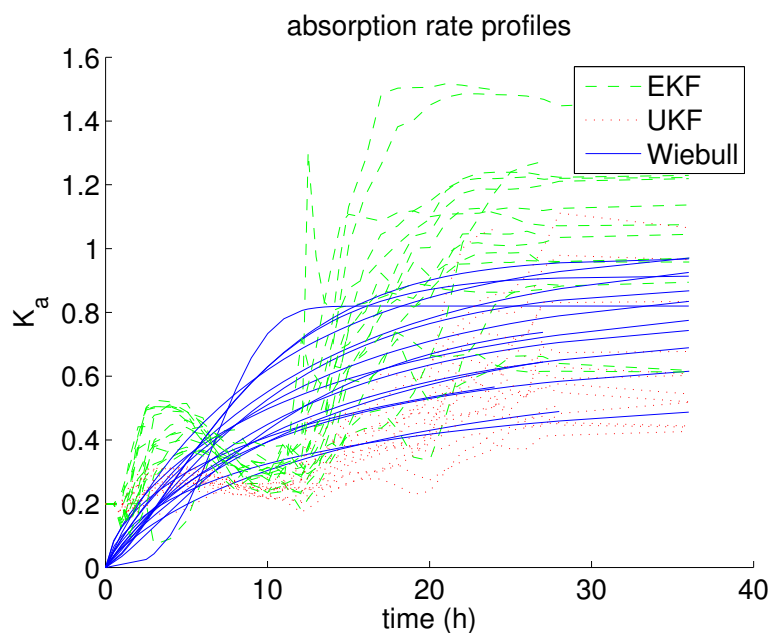


Figure 6.5: Absorption rate profiles,  $k_a$ , for Wiebull, EKF, and UKF models. This figure displays the temporal dynamics of the absorption rate of QD dose metformin for each individual.

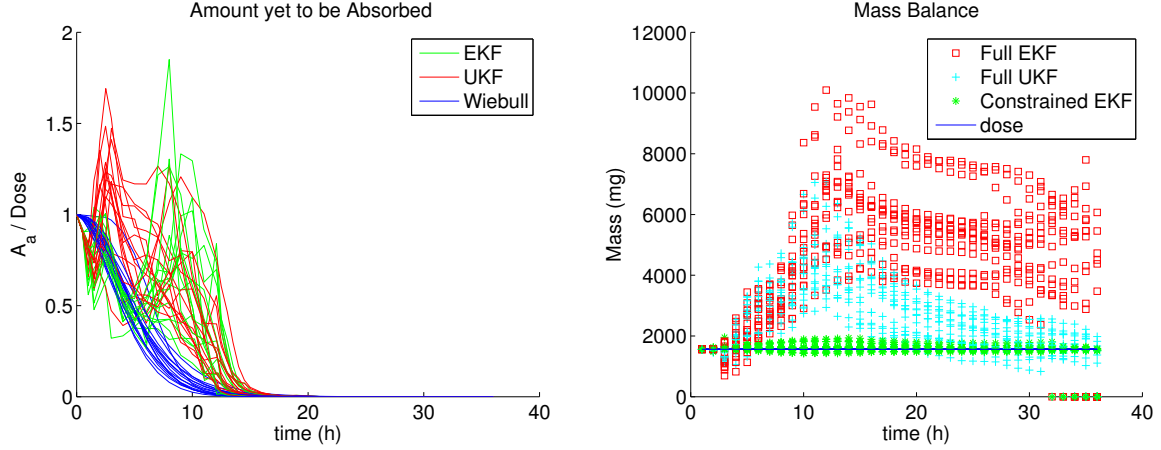


Figure 6.6: Left: Plots of the fraction yet to be absorbed of metformin utilizing the EKF, UKF, and Wiebull ODE model. Right: Mass balance of drug over time for the EKF, UKF, and constrained EKF solutions.

tion compartment along with the rate parameter,  $k_a$ , seem to deviate. The EKF maintains a smaller noise estimate for the absorption compartment ( $\sigma_{absorption} = 0.19$ ) while associating the majority of the variability to the absorption rate ( $\sigma_{k_a} = 0.39$ ). However, the UKF maintains a much smaller noise estimate for the absorption rate ( $\sigma_{k_a} = 0.064$ ) while also increasing the absorption compartment's diffusion parameter estimate ( $\sigma_{absorption} = 0.25$ ). The immediate effects of this result are better seen in Figure 6.5. Relegating more variability to the noise term for the rate parameter  $k_a$ , allows  $k_a$  to drift more readily to explain the concentration data as seen in the EKF estimates. The UKF estimates for  $k_a$  are constrained to a lesser range due to the small noise diffusion parameter,  $\sigma_{k_a}$ .

While the filter predictions do well to explain the observations, the absorption compartment is examined to check the effects of the estimated variability. Administering an oral dose, it is expected that the initial value would align with the dose and decay at a rate respective of the absorption rate parameter  $k_a$ . Dividing the absorption compartment by the dose, the amount yet to be absorbed is displayed, Figure 6.6. Comparing the filters, a troubling discovery is seen due to the large estimated variability. The fraction left to be absorbed not just increases, but can increase to values greater than one, meaning mass is being created within the absorption compartment. Looking over Figure 6.6, the mass balance is calculated as the sum of all the compartments over time, done for the filtering methods. Given this is a closed system, the sum of all the compartments at any time should equal the dose. Figure 6.6 confirms this concern of mass being created as mass grows to values much larger than the dose.

To overcome this, the noise terms for the states ( $\sigma_{abs}, \sigma_{central}, \sigma_{peripheral}$ ) in the absorption rate tracking model are fixed to be small while estimating the noise for  $k_a$ . This minimizes the chance of mass creation while still allowing information to be obtained on the absorption rate parameter,  $k_a$ . The results for mass balance of this constrained absorption rate tracking model are displayed for the EKF in

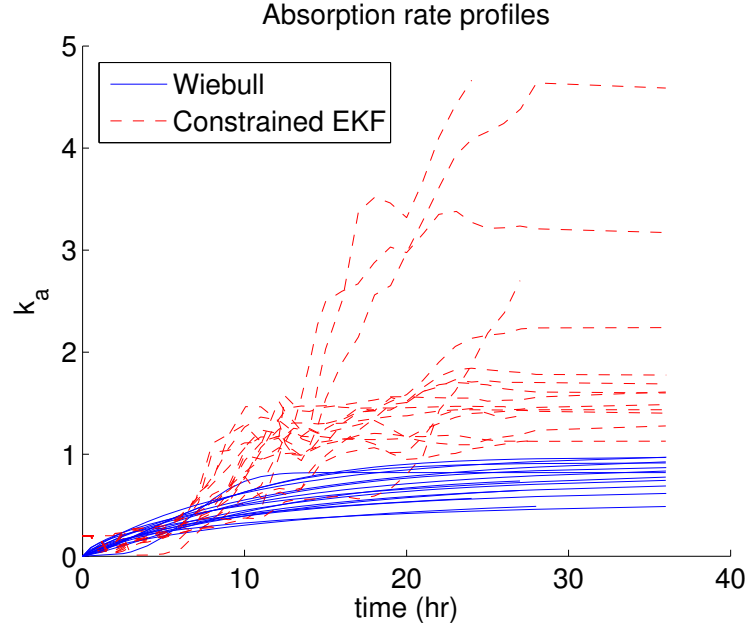


Figure 6.7: Absorption rate profiles,  $k_a$ , for Wiebull and constrained EKF models.

Figure 6.6. While some mass can still be created due to the noise terms, the effect is largely minimized by fixing their values. Understanding how this adjustment affects the absorption rate parameter,  $k_a$  is plotted for the constrained EKF in Figure 6.7. This results in a much larger rate of absorption for each subject along with a larger variance to the terminal rate. Reviewing Table 6.2, the effects of the constraints of the noise terms on the model parameter are displayed. The residual error,  $\sigma^2$ , and loglikelihood are both worse as expected given the number of degrees of freedom taken out of the fit along with the inability to quantify the modeling error for those respective states. This error now gets lumped with the residual variability which explains the increase. However, to adjust for this, the variability in the absorption rate parameter increases to try to account for the deficiencies of the absorption process. The volume of distribution estimate also changes, approaching the estimate obtained from the initial two compartment model. Utilizing the information obtained from the SDE models, a structural model for the absorption rate is constructed.

### 6.5.3 2-compartment Oral with Wiebull absorption rate

Given the temporal dynamics observed from the SDE models for the absorption rate parameter,  $k_a$ , a structural model is enacted to describe this process. A Weibull function is utilized within the initial two

Table 6.1: Results for 2-compartment Oral model with log-additive errors for original model, EKF, UKF, and Wiebull absorption.

	2-cpt Oral	EKF	UKF	2-cpt Oral Wiebull	2-cpt Oral Wiebull UKF
$\sigma^2$	0.24	0.092	0.068	0.021	0.0271
<b>R</b>	N/A	0.0892	0.0659	N/A	0.0264
$\sigma_{abs}$	N/A	0.1895	0.2478	N/A	0.0239
$\sigma_{central}$	N/A	0.0078	0.0058	N/A	0.0023
$\sigma_{peripheral}$	N/A	0.0353	0.0214	N/A	0.0232
$\sigma_{K_a}$	N/A	0.3882	0.0638	N/A	N/A
$k_a (h^{-1})$	0.21	N/A	N/A	N/A	N/A
$k_{12} (h^{-1})$	0.16	0.1963	0.0671	0.29	0.259
$k_{21} (h^{-1})$	0.0017	0.0024	0.007	0.0028	0.0021
$k_e (h^{-1})$	0.03	0.0093	0.1627	0.0008	0.0013
$V (L)$	593.12	1617.83	1670.04	334.46	363.52
Loglike	-415.51	-70.64	-24.65	177.87	201.64
-2LL	831.02	142	49.31	-355.75	-403.28
$t_{1/2} \text{ elim } (h)$	23.10	74.52	4.26	866.43	533.19
$Cl (L h^{-1})$	17.79	15.05	271.72	0.27	0.473
$Cl2 (L h^{-1})$	94.9	317.58	112.06	96.99	94.15
$V2 (L)$	55,823.5	132,324.2	16,008.53	34,539.3	44,833.3
$\alpha$	N/A	N/A	N/A	0.814	1.194
$K$	N/A	N/A	N/A	0.995	1.00
$\lambda$	N/A	N/A	N/A	12.086	15.58

compartment oral model to describe the extended release absorption rate, written out below

$$k_a = \alpha(1 - \exp(-(t/\lambda)^K)) \quad (6.53)$$

$$\frac{d}{dt} \begin{pmatrix} A_a \\ C \\ A_{peripheral} \end{pmatrix} = \begin{pmatrix} -k_a & 0 & 0 \\ \frac{k_a}{V} & -(k_{12} + k_e) & \frac{k_{21}}{V} \\ 0 & k_{12}V & -k_{21} \end{pmatrix} \begin{pmatrix} A_a \\ C \\ A_{peripheral} \end{pmatrix} \quad (6.54)$$

$$\log(C_{obs}) = \log(C) + e, \quad e \sim N(0, \sigma^2) \quad (6.55)$$

where  $\alpha$ ,  $\lambda$ , and  $K$  are now shape parameters which will be optimized within the mixed effects framework. Reviewing Figure 6.8, the plasma concentration profiles fit the data which can be better seen through the predicted versus observed concentration plot. Comparing the absorption rate profiles to the original filter estimates, Figure 6.5 shows that while the qualitative nature of the absorption does not match, the quantitative range of the rates sync up with the filter estimates. The UKF had terminal rates between 0.4-1 and the EKF had terminal ranges between 0.6-1.5, while the Weibull absorption has a terminal range 0.4-0.9. The parameter estimates for the kinetic parameters for the Weibull absorption are displayed in Table 6.1.

Lastly, to check the validity of the final model, the two compartment oral model with Weibull absorption was run with the UKF with noise terms relegated to the states. Reviewing the noise estimates for the states in Table 6.1, the absorption noise,  $\sigma_{abs}$ , has diminished due to the better quantified process and no longer is considered significant. Looking over the kinetic parameter estimates, they match the ODE model which again validates the structural model for  $k_a$ .

## 6.6 Discussion and Conclusion

While mixed effect models traditionally utilize ordinary differential equations to describe a physical process, an SDE model approach is presented. This allows the intra-individual variability to be further decomposed into measurement noise and process noise. The process noise represents model misspecification and autocorrelated residual errors while the measurement noise accounts for assay error, sampling, and other errors due to observation collection.

This study presented the derivation of the EKF and UKF for application within nonlinear mixed effect solvers, more specifically, sampling based methodologies. Using metformin clinical data, model development was carried out through the application of SDEs. The performance of the EKF and UKF was compared, displaying the advantages of the unscented Kalman filter in terms of overall performance over the extended Kalman filter. Initially fitting an oral two compartment model, deficiencies in the absorption process were highlighted. This led to the development of an SDE model to better elucidate the

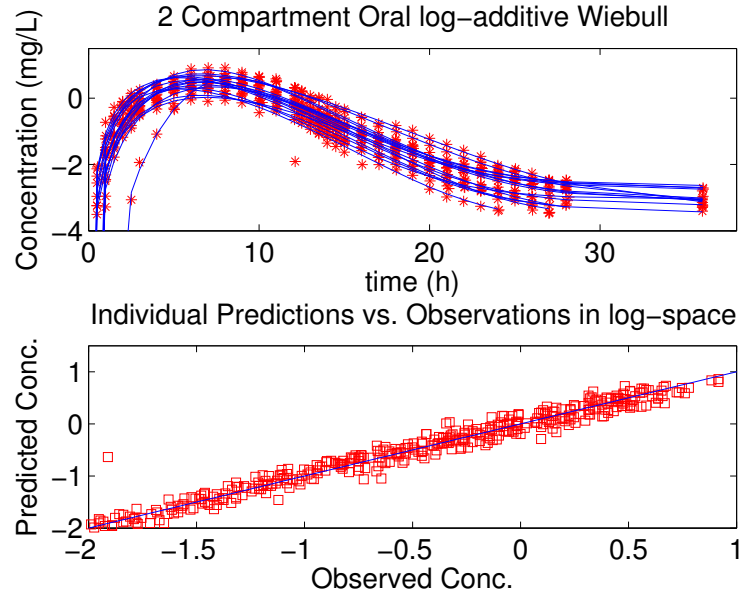


Figure 6.8: Top: Population PK model fit for 16 subjects concentration profiles in log-space for concentration. Model fit utilizes a 2-compartment oral absorption model with Wiebull absorption rate with log-additive error. Bottom: Individual predictions vs. individual concentrations with unity line(blue). Unity line represents the ideal situation where the model perfectly predicts the observations.

Table 6.2: Results for 2-compartment Oral model with log-additive errors for full EKF and constrained EKF.

	EKF	Constrained EKF
$\sigma^2$	0.092	0.15
R	0.0892	0.1441
$\sigma_{abs}$	0.1895	1e-7
$\sigma_{central}$	0.0078	1e-7
$\sigma_{peripheral}$	0.0353	1e-7
$\sigma_{K_a}$	0.3882	0.83
$k_a (h^{-1})$	N/A	N/A
$k_{12} (h^{-1})$	0.1963	0.191
$k_{21} (h^{-1})$	0.0024	0.002
$k_e (h^{-1})$	0.0093	0.025
V (L)	1617.83	516.88
Loglike	-70.64	-153.25
-2LL	142	306.5

absorption process. Comparing the estimates between the methods and models, the changes in structural model assumptions impacted the estimates for volume of distribution. Reviewing the study of metformin XR by Duong et al [6], the filter obtains a volume estimate approximately ten times larger. However, for the clearance parameter, the estimates ranged greatly depending on the filter from approximately three times greater (UKF) to five times less (EKF). This uncertainty is likely caused by the uncertainty linked to the volume and elimination parameters. The size of the study likely had an effect on the estimates as well, given Duong et al [6] conducted a study with 305 subjects, while this study has only managed 16 subjects.

Estimating the noise terms allowed the refinement of the two compartment model. This led to obtaining information on the absorption process which led to a structural model alteration for the absorption rate,  $k_a$ , as a Weibull function. While the filters helped to give model misspecification estimates for the different states, and also provided a fitting method for the temporal dynamics of the absorption rate, they did have issues by creating mass when large model misspecification was present. To prevent this, the noise terms were fixed which still provided a way to handle both the auto correlated errors and time varying parameter absorption rate. Applying the UKF to the final ODE model, the parameter estimates for the noise were small and the parameter estimates for the kinetics were nearly identical. The similar estimates for both the ODE and SDE models confirmed what was found in previous studies [12, 36].

Overall, the application of SDEs to nonlinear mixed effect modeling was highlighted. SDEs allow the estimation of model misspecification, and can also account for serial correlations. Along with these advantages, the SDE approach provided a systematic model development framework by tracking model deficiencies. Lastly, the differences between the extended and unscented Kalman filters were displayed.



## REFERENCES

- [1] Aarons, L. "Pharmacokinetic and pharmacodynamic modelling in drug development." Statistical Methods in Medical Research. Vol. 8, No. 3, 1999, Pgs. 181-182.
- [2] Buse, J., DeFronzo, R.A., Kim, T., Skare, S., Baron, A., and Fineman, M. (September 2013) *Disso-*  
*ciation between metformin plasma exposure and its glucose-lowering effect: a novel gut-mediated*  
*mechanism for action*. Presentation at the 49th Annual European Association for the Study of Dia-  
betes Meeting, Barcelona, Spain.
- [3] Chi, E.M. and Reinsel, G.C. "Models for longitudinal data with random effects and AR(1) errors." Journal of American Statistics Association. Vol. 84, 1989, Pgs. 452-459.
- [4] Davis, P.J. and Rabinowitz, P. Numerical Integration. Blaisdell, Waltham, MA. 1967.
- [5] Davidian, M. and Giltinan, D.M. "Some general estimation methods for nonlinear mixed-effects  
model." Journal of Biopharmaceutical Statistics. Vol. 3, No. 1, 1993, Pgs. 23-55.
- [6] Duong, J.K., Kumar, S.S., Kirkpatrick, C.M., Greenup, L.C., Arora, M., Lee T.C., Timmins, P.,  
Graham, G.G., Furlong, T.J., Greenfield, J.R., Williams, K.M., and Day, R.O. "Population Pharma-  
cokinetics of Metformin in Healthy Subjects and Patients with Type 2 Diabetes Mellitus: Simulation  
of Doses According to Renal Function." Clinical Pharmacokinetics. Vol. 53, 2013. Pgs. 373-384.
- [7] Gerstner, T. and Griebel, M. "Numerical integration using sparse grids." Numerical Algorithms.  
Vol. 18, 1998, Pgs. 209-232.
- [8] Grimmett, G. and Stirzaker, D. Probability and Random Processes. New York: Oxford University  
Press, 2001.
- [9] Haykin, S. Kalman Filtering and Neural Networks. New York: John Wiley and Sons, Inc., 2001.
- [10] Jazwinski, A.H. Stochastic Processes and Filtering Theory. New York: Academic Press, 1970.

- [11] Julier, S., J. and Uhlmann, J. K. "A New Extension of the Kalman filter to Nonlinear Systems." In Proc. of Aerosense: The 11th Int. Symp. on Aerospace/Defense Sensing, Simulation and Controls. 1997.
- [12] Karlsson, M.O., Beal, S.L., and Sheiner, L.B. "Three new residual error models for population PK/PD analyses." Journal of Pharmacokinetics and Biopharmaceutics. Vol 23, No. 6, 1995, Pgs. 651-672
- [13] Kalman, R.E. "A new approach to linear filtering and prediction problems." Transactions of the ASME - Journal of Basic Engineering. Vol. 82, 1960, Pgs. 35-45.
- [14] Kalman, R.E. and Bucy, R.S. "New results in linear filtering and prediction theory." Transactions of the ASME - Journal of Basic Engineering. Vol. 83, 1961, Pgs. 95-108.
- [15] Klebaner, F.C. Introduction to Stochastic Calculus with Applications. London: Imperial College Press, 2005.
- [16] Kristensen, N.R., Madsen, H., and Jorgensen, S.B. "Parameter estimation in stochastic grey-box models." Automatica. Vol. 40, 2004, Pgs. 225-237.
- [17] Lalau, J.D. and Lacroix, C. "Measurement of metformin concentration in erythrocytes: clinical implications." Diabetes, Obesity, and Metabolism. Vol. 5, 2003, Pgs. 93-98.
- [18] Lindsey, J.K., Jones, B., and Jarvis, P. "Some Statistical issues in modeling Pharmacokinetic data." Statistics in Medicine. Vol. 20, 2001, Pgs 2775-2783.
- [19] Majda and Harlim, J. Filtering turbulent complex systems. Cambridge University Press, UK, 2012.
- [20] Morokoff, W. and Caflisch, R. "Quasi-Monte Carlo integration." Journal of Computational Physics. Vol. 122, No. 2, 1995, Pgs. 218-230.
- [21] Myung, I.J. "Tutorial on maximum likelihood estimation." Journal of Mathematical Psychology. Vol. 47, 2003, Pgs. 90-100.

- [22] Overgaard, R.V., Jonsson, N., Tornøe, C.W., and Madsen, H. "Nonlinear Mixed-Effects Models with Stochastic Differential Equations: Implementation of an Estimation Algorithm." Journal of Pharmacokinetics and Pharmacodynamics. Vol. 32, No. 1, 2005, Pgs. 85-107.
- [23] Pinhiero, J.C. and Bates, D.M. "Approximations to the Log-Likelihood Function in the Nonlinear Mixed Effects Model." Journal of Computational and Graphical Statistics. Vol. 4, No. 1, 1995, Pgs. 12-35.
- [24] Racine-Poon, A. and Wakfield, J. "Statistical Methods for population pharmacokinetic modeling." Statistical Methods in Medical Research. Vol. 7, No. 1, 1998, Pgs. 63-84.
- [25] Sheiner, L., and Wakefield, J. "Population modeling in drug development." Statistical Methods in Medical Research. Vol. 8, No. 3, 1999, Pgs. 183-193.
- [26] Sheiner, L.B. and Steimer, J.L. "Pharmacokinetic/Pharmacodynamic Modeling in Drug Development." Annual Review of Pharmacology and Toxicology. Vol. 40, 2000, Pgs. 67-95.
- [27] Sloan, I.H. and Wozniakowski, H. "When are Quasi-Monte Carlo Algorithms Efficient for High Dimensional Integrals?" Journal of Complexity. Vol. 14, No. 1, 1998, Pgs. 1-33.
- [28] Smith, R. Uncertainty Quantification: Theory, Implementation, and Applications. SIAM, Philadelphia, PA. 2014.
- [29] Smith, R.C. Smart Material Systems: Model Development. SIAM, Philadelphia, PA, 2005.
- [30] Smolyak, S. "Quadrature and interpolation formulas for tensor products of certain classes of functions." Doklady Akademii Nauk SSSR. Vol. 4, 1963, Pgs. 240-243.
- [31] Stroud, A. and Secrest, D. Gaussian Quadrature Formula. Prentice-Hall, NY. 1966.
- [32] Stoer, J and Bulirsch, R. Introduction to Numerical Analysis. Second edition, Springer-Verlag, NY. 1993.

- [33] Taylor, A., Chigutsa, E., Monteleone, J., and Fineman, M. (May 2013) *Population Pharmacokinetic Modeling of a Novel Delayed-Release Formulation of Metformin (MetDR)*. Poster presented at the American Conference on Pharmacometrics, Fort Lauderdale, FL, USA.
- [34] Tornøe, C.W., Agerso, H., Jonsson, E.N., Madsen, H., and Nielsen, H.A. "Nonlinear mixed-effects pharmacokinetic/pharmacodynamic modelling in NLME using differential equations." Computer Methods and Programs in Biomedicine. Vol. 76, 2004, Pgs. 31-40.
- [35] Tornøe, C.W., Jacobsen, J.L., Pedersen, O., Hansen, T., and Madsen, H. "Grey-box modelling of pharmacokinetic/pharmacodynamic systems." Journal of Pharmacokinetics and Pharmacodynamics. Vol. 31, 2004, Pgs. 401-417.
- [36] Tornøe, C.W., Overgaard, R.V., Agerso, H., Nielsen, H.A., Madsen, H., and Jonsson, E.N. "Stochastic Differential Equations in NONMEM: Implementation, Application and Comparison with Ordinary Differential Equations." Pharmaceutical Research. Vol. 22, No. 8, 2005, Pgs. 1247-1258.
- [37] Tucker, G.T., Casey, C., Phillips, P.J., Connor, H., Ward, J.D., and Woods, H.F. "Metformin Kinetics in Healthy Subjects and in Patients with Diabetes Mellitus." British Journal of Clinical Pharmacology. Vol. 12, 1981. Pgs. 235-246.
- [38] Wann, E. and Van Der Merwe, R. "The Unscented Kalman Filter for Nonlinear Estimation." Adaptive Systems for Signal Processing, Communications, and Control Symposium, IEEE. 2001. Pgs. 153-158.

## Chapter 7

# Conclusion

Overall, the application of nonlinear filtering to biological systems modeling has been highlighted through its utility in a number of problems, both simulated and real world. The motivation for its use was given due to the required simplification of complex processes in biology for modeling purposes. Filtering provides a useful way to incorporate the effects of these simplifications within the modeling framework. The definition and premise of the inverse problem was presented. The application of filtering to inverse problems was highlighted in chapter two. Multiple techniques can be used to utilize filtering for parameter estimation. The precision and accuracy of each technique was displayed on a number of problems of varying difficulty, and the strengths and weaknesses were discussed. The ability of the filters to overcome a multitude of challenges including stiffness, strong nonlinearities, proportional error models, and sparse sampling were necessary adversities to overcome for real application.

Next, to facilitate the proper modeling of autonomic regulation of the cardiovascular system via the baroreceptor, the biology of the cardiovascular system was discussed. This provided the necessary background to understand the important processes for modeling the effects of the body during orthostatic stress. Using the biology of the CVS, along with a circuit analogy, a model was constructed using heart rate data to predict blood pressure during a head-up tilt experiment. Accounting for the pooling of blood in the lower extremities due gravitational effects through hydrostatics, a five compartment model was constructed. The simplified model was used to describe the autonomic regulation via the baroreceptor during head-up tilt through the estimation of the resistance of the arteries and contractility of the heart. These parameters were selected to be estimated by conducting a sensitivity analysis followed by subset selection, along with understanding the information to be examined about the biological system. Using a nonlinear spline methodology, these time varying quantities were estimated and compared to the estimates obtained from the ensemble transform Kalman filter. This helped to again highlight the utility of the Kalman filter to complex biological systems, and also gain knowledge on the regulation of the CVS during head-up tilt.

Next, general background on pharmacokinetics and pharmacodynamics was presented to provide

the necessary information for the modeling to take place. Understanding the disposition of a drug as it enters the body, distributes, causes an effect, and is eliminated is crucial to properly model the system. Detailing those processes helped show the complexity of the systems we wish to understand and test hypotheses against.

Lastly, using the background on pharmacokinetics and pharmacodynamics, nonlinear mixed effects modeling was introduced and applied to a PK study for metformin. Using both an extended and unscented Kalman filter within the nonlinear mixed effect framework allowed the quantification of model misspecification which could be used to understand modeling deficiencies. This also could account for time correlated residuals and provided a method for estimation of time varying parameters, already witnessed in a previous chapter. This methodology provided a model development framework for biological systems. Not only that, the estimation of model misspecification for populations would allow the use of filters in the future for medical purposes since the process noise matrix is necessary *a priori* information for actually, real world application of Kalman filtering. Applying an importance sampling based expectation maximization algorithm with SDEs to a small, metformin study allowed a better, and more thorough, understanding of the absorption process of the drug. While the study was small, it showed the value of SDEs in modeling.

Overall, this thesis presented a thorough, detailed narrative on nonlinear filtering methodologies and their application to parameter estimation, state estimation, and uncertainty quantification. Future work would hope to further develop some of the methods displayed including, but not limited to, when to use a joint estimation method over a dual estimation method, particle filtering, the advantages of particle filtering over Kalman filtering and vice versa, how to overcome mass balance issues in a closed system utilizing filters, how sensitivities and correlation affect filter performance, and any refinements upon the filtering algorithms themselves.